Doctoral Dissertation

FPGA-based system development for high-throughput single-cell detection and sorting from micro to nanoscale

（FPGAシステム開発に基づいたハイスループット

・マルチスケールな細胞計測と分取）

TANG TAO

September 2022

Division of Material Science

Graduate School of Science and Technology

Nara Institute of Science and Technology

Contents

1. General Introduction

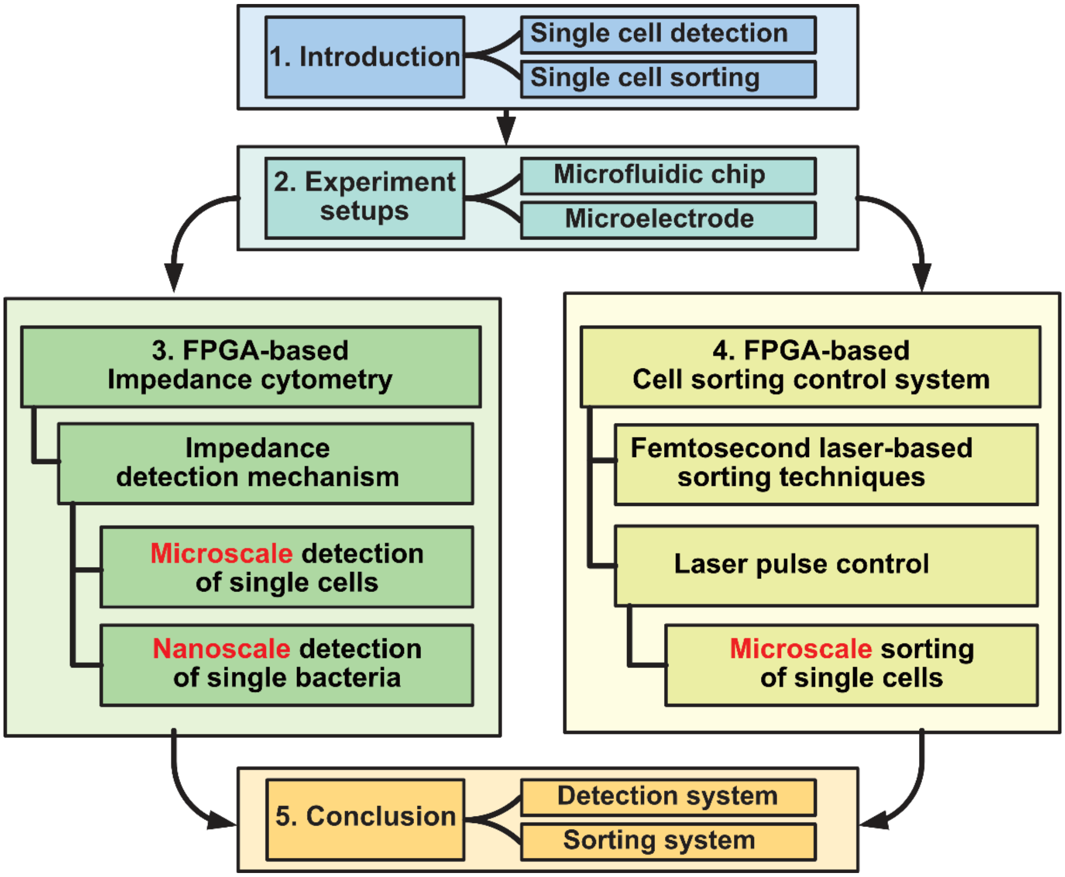

Fig. 1.1: Outline diagram of the dissertation

1.1. Inhomogeneous cells

Cells are considered the basic units of life, performing a multitude of complex functions and readily changing their program in response to environmental changes. For instance, cells in mammals are heterogenous in their functions and states, and they work together to maintain normal bodily functions [1]. Each cell type is specifically tuned to the specific tissue, in which it resides, and owns a different morphology and internal structure (see Fig. 1.2A).

As an example of cellular morphology, in all vessels, the endothelial cells were highly elongated polygons, usually hexagonal, which were oriented along the vessel axis. The clefts were highly oriented with a preferred orientation which was parallel to the vessel axis [2]. By contrast, skeletal muscle cells or fibers are highly elongated cells with a very elastic and resistant plasma membrane [3]. It has known that the cellular morphology is dependent on cellular phenotype and physiological and signaling states. Many functional changes in cells cause stereotypical changes in cellular morphology, and some changes in shape can also cause characteristic changes in cellular phenotype [4].

As for the cell interior, all cells consist of cytoplasm filled with a jelly-like substance called cytosol. Organelles inside the cell are suspended in the cytosol, and interact with one another and the cytoskeleton to synergistically execute various physiological functions [5], [6]. Typically, intracellular organelles and molecules varies with the cell type and states, e.g., red blood cells only contain hemoglobin and do not have a nucleus like white blood cells. Much is known about the intracellular elements, from large organelles to minute molecules, but how they interact and how these interactions are regulated to sustain an organized and functional cell is largely unknown [7].

Additionally, within any single tissue, no matter how apparently homogeneous, there is a diverse population of normal cells, all of which represent different manifestations of that tissue type. For instance, normal mammary epithelial cell growth, differentiation and morphogenesis are optimally supported by interaction with surrounding cell matrix. However, if some of them turn to be cancer cells, it would be another story. Some properties of cells would be different, including duplication, morphology, and even intracellular structures and components. For instance, breast tissue becomes progressively stiffer and tumor cells become significantly more contractile and hyper-responsive to matrix compliance cues [8]. As shown in Fig. 1.2B, cancer cells may look very different from normal cells. In contrast to normal cells, cancer cells grow and divide at an abnormally rapid rate, are poorly differentiated, and have abnormal membranes, cytoskeletal proteins, and morphology.

Overall, cell-to-cell variation is a universal property of multi-cellular organisms, which contain diverse cell types characterized by different functions, morphologies, and gene expression profiles. For normal cells, these properties are relatively stable, but they can vary when they are cancerous, old, or under certain stimuli.

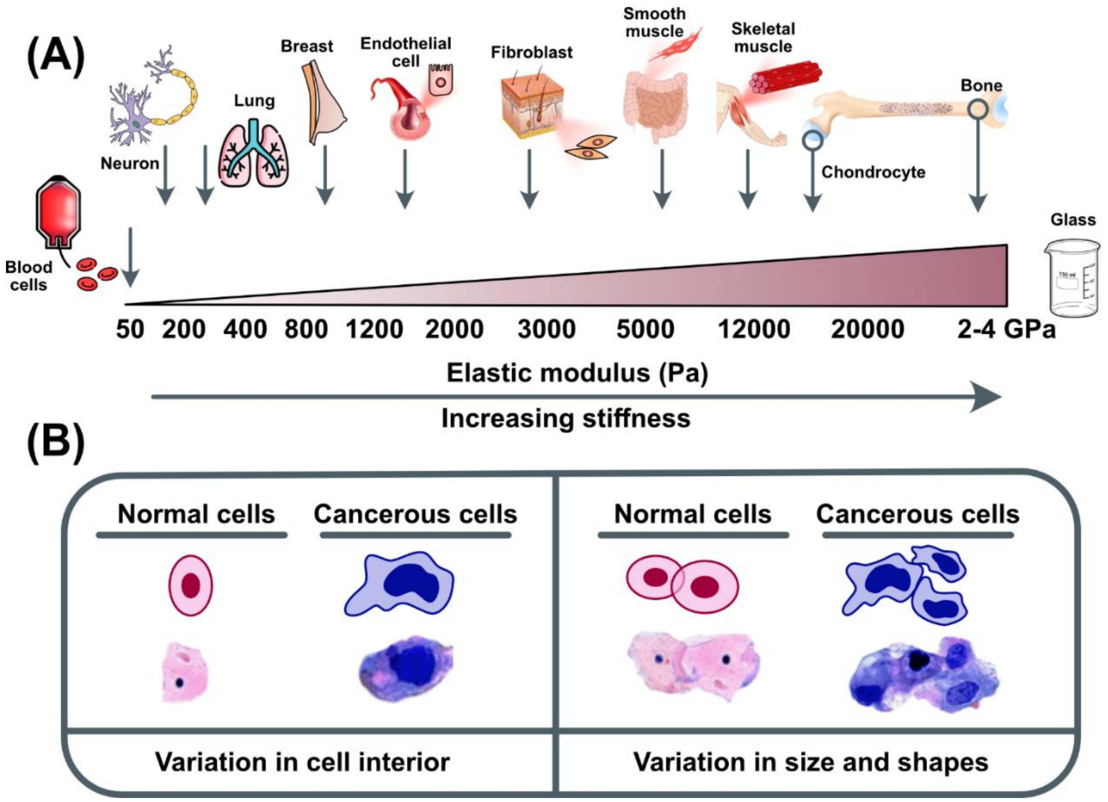

Fig. 1.2: Cells are tuned to (A) their functions and (B) states.

1.2. High-throughput single-cell detection

Investigation of tissues or cell populations is inherently limited by the fact that the readout of assays that uses bulk tissue to represent an average of a cell population. Intrinsic cellular heterogeneity in single cells is obscured in the typical bulk tissue studies [9]. Cytometry technologies have advanced recently to detect hundreds and thousands of cells in a second; this allows a more precise understanding of the properties of individual cells and of the difference between single cells [10].

1.2.1. Optical cytometry

Cytometry technique is a method to perform rapid multi-parametric analysis of single cells or particles suspended in solution. Traditional flow cytometers, namely the optical cytometry, consist of three systems: fluidics, optics, and electronics. The fluidics system consists of sheath fluid to focus suspended sample in the microchannel before optical detection. Single sample is analyzed when it passes the detection laser focal point. The optical system consists of excitation optics (lasers) and collection optics (photomultiplier tubes or PMTs and photodiodes) that generate the visible and fluorescent light signals used to analyze the sample, as shown in Fig. 1.3A. Single particle analysis relies on the interrogation of individual cells by laser light and the collection of the resulting fluorescence and scatter. As an example of the volume detection, the durations ("widths") of the scatter and fluorescence pulses generated by the passage of individual particles (see Fig. 1.3A) represents the time of the particle passing through the beam. The scatter duration is increasing with the diameter of cells. Besides, the integral ("area") of a pulse provides an indication of the total amount of scattering or fluorescing material in a cell; the maximum intensity value ("peak" or "height") of a pulse provides an approximate measure of the highest concentration of scattering or fluorescing material [11]. Research has shown that the optical cytometry is capable of detecting, identifying, and counting specific cells. This method can also identify particular components within cells [12], but the fluorescence dying is essential for this method which would pose chemical or physical impact on cells [13].

1.2.2. Imaging cytometry

Imaging cytometry combines traditional optical flow cytometry with fluorescence microscopy, as shown in Fig. 1.3B. This allows for rapid analysis of a sample for morphology and multi-parameter fluorescence at both a single cell and population level [14], [15]. In contrast to pure quantitative measurements provided by optical flow cytometry, imaging cytometry allows capturing cell images that contain a wealth of information about a cell. While optical flow cytometry measures forward scattered light to estimate the relative cell size, microscopy yields the exact cell size through its bright field image. To date, this technique has realized both 3-

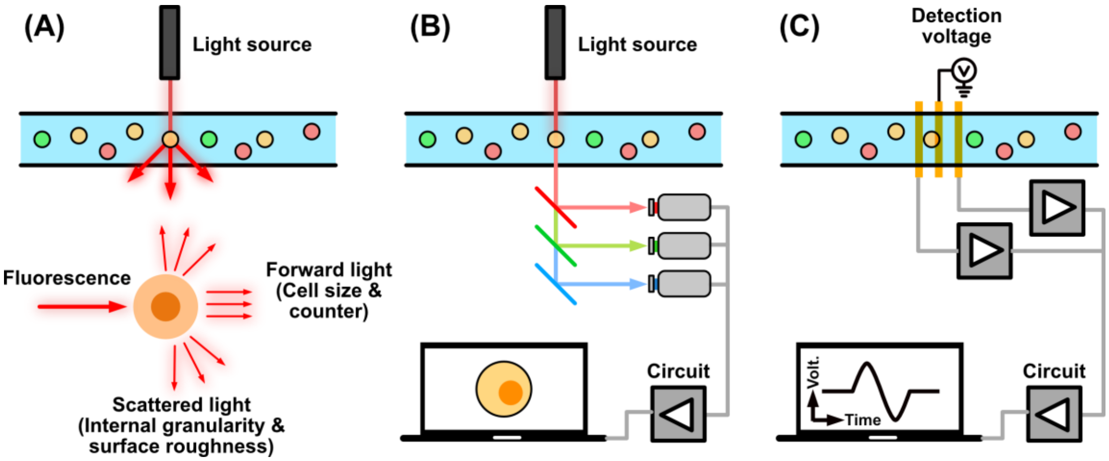

Fig. 1.3: Schematics of flow cytometry, including (A) optical cytometry, (B) Imaging cytometry, and (C) Impedance cytometry

dimensional and super resolutions that allow imaging of the biological structure and function beyond the diffraction limit, producing extraordinarily detailed fluorescent cell images [16], [17]. Additionally, a parallel microfluidic cytometer has shown its capability of performing detection with higher throughput and higher content [15], [18], but has very limited 1-dimensional spatial resolution. Imaging cytometry, however, imposes a huge burden on the back-end data handling units that handle digital image transportation and processing. This technique can generate thousands of multi-spectral images of cells per second. Thus, the files generated by imaging cytometry can be extremely stressful on the back-end data handling units [19], [20]. Additionally, in imaging cytometry systems, the optical setups and techniques used are extremely expensive and demand a lot of the experimental environment as well as their handlers [21], [22].

1.2.3. Impedance cytometry

A label-free alternative to impedance cytometry is impedance spectroscopy, as shown in Fig. 1.3C. Typically, high-throughput internal and external cell detection can be achieved by impedance cytometry with relatively inexpensive devices. Microfluidic impedance cytometry involves the measurement of the electric field screening of individual cells passing over patterned electrodes in a microchannel, as accomplished by electric current variation under an applied AC voltage. The measured current exhibits a characteristic temporal signal shape whose features depend on the applied potential, the system impedance, and cell properties, *i.e.*, volume and dielectric properties [23]. The measured impedance is frequency dependent and exhibits characteristic dispersions for each subcellular region [24]. While the electrical double-layer around the electrodes screens the field at frequencies <100 kHz, the signal is chiefly determined by the cellular electrical size in the 0.1–1 MHz range due to complete membrane-induced screening. Polarization of the plasma membrane in the 2–10 MHz range offers information on membrane morphology based on measured capacitance. In the 10–30 MHz range, the membrane is minimally polarized, so that the cytoplasmic conductivity and permittivity provide information on the organelles, while at higher frequencies, the response is dependent on nucleus properties. It is noteworthy that the exact frequency range values are dependent on cell size, media conductivity and the complex conductivity of the respective subcellular layer. Using superimposed voltage sinusoids, the impedance magnitude and phase can be obtained simultaneously over multiple frequencies for each cell, paving the way for multiparametric analysis by fitting impedance spectra to the appropriate shell model for characterization of subcellular electrophysiology. However, while cell recognition by fluorescence cytometry can simply be determined based on pre-set thresholds, recognition based on impedance metrics requires the analysis of temporal signal trains of single cells at each frequency and population-level analysis of the scatter plots to identify characteristic frequency dispersions.

1.3. Single cell sorting

Sorting particles and cells from heterogeneous suspensions is an essential step in the processing and purification of complex mixtures for subsequent analysis and diagnosis [25]–[27]. Especially in many therapeutic and diagnostic practices, sorting process is widely used as the first step for drug screening [28], stem cell investigations [29], tissue and organ regeneration[30], and cancer diagnostics and therapy[31]–[33]. By far, there are numerous sorting techniques and applications, the majority of which consist of two steps: detection and cell manipulation. One well-established approach is fluorescence-activated cell sorting (FACS) [34]–[36]. Important cells are pre-stained with fluorescent dyes for easy detection and to activate the sorting system (i.e., cell manipulation). Typically, these dyes are very lipophilic, they can be used to tag any type of cell fast and effectively [37]–[39], but the fluorescence intensities of stained cells differ for various reasons, such as the cellular physical properties [40], viability [41], and cell cycle profiling [42], [43]. Aside from fluorescence intensities, the same cell lines can also differ in other aspects, including dielectric properties[44], [45], deformability[46]–[48], and morphology[22], [49], [50]. In other words, cell lines can be divided into several subpopulations based on a single detection method such as fluorescence intensity or dielectric characteristics.

As for the cell manipulation, to date, most research focus on the binary separation since some active sorting systems only accept one key line, like the presence or absence of a fluorescent signal in FACS [34], [51], [52]. The type of cell manipulation techniques determines whether a sorting system can be extended to accommodate multiple selection. The viscoelastic flows [50] and the deterministic lateral displacement (DLD) [53], [54], for example, can sort multiple cells while these passive techniques are only useful for size-based separation. Active cell manipulation is required when it is necessary to work with a variety of cell phenotyping and detection approaches. For example, the traveling surface acoustic waves (TSAW) [55] has been applied for volume-based multi-separation. However, standard acoustic microfluidic devices suffered from high voltage requirement (e.g., > 200 Vpp) and excess heat [52], [56]. Due to poor energy conversion, a large portion of the electrical energy used in acoustofluidic sorters is lost as heat, which weakens the biocompatibility of acoustofluidic sorters. Alternative is to use multi-steps on-chip sorters (i.e., integrated and combined microchips), which incorporate several separation processes into a single chip. [57], [58]. Multi-step sorters, on the other hand, have a number of issues, such as difficult microchip design and fabrication [59], [60], greater sample loss due to the larger on-chip space required for the multi-step process [61]–[63], and low throughput (e.g., <1 kHz)[57], [64].

The femtosecond (fs) laser-assisted method [51] (see Fig. 1.4A) offers several advantages over other cell manipulation techniques, like the highest throughput, up to 100 kilohertz (kHz), which is far exceeding others, such as dielectrophoresis (DEP) (90 Hz [65]) (see Fig. 1.4B), traveling surface acoustic waves (TSAW) (4 kHz [66]) (see Fig. 1.4C), piezoelectric transducer (PZT) (23 kHz [67]) (see Fig. 1.4D). Although magnetophoresis (MAP) has also been shown to reach a high throughput (83 kHz [68]), labeling cells with magnetic beads or removing labels are laborious and difficult (see Fig. 1.4E). In Contrast, fs-laser-assisted binary sorting has reached a 100% success rate at a high throughput (100 kHz) for polystyrene beads, and a 63% success rate at an 83.3 kHz throughput for cells in previous work [51]. In this technique, a jet flow is generated by the fs pulse irradiation and acts as an impulsive force on objects, i.e., the fs pulse irradiation generates shock and stress pressure waves, resulting in the jet flow. Thus, there is no cell damage caused by the heat generation during the sorting process [69]. No physical heating

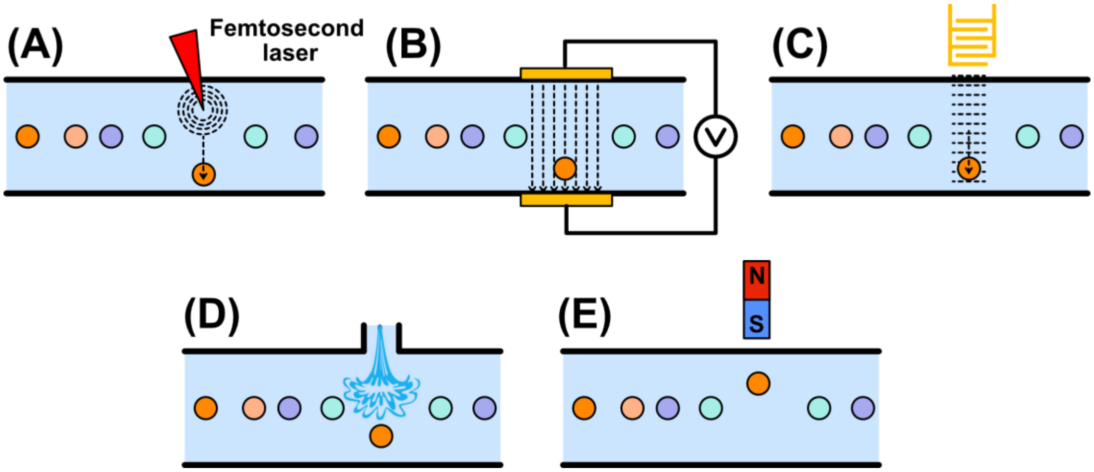

Fig. 1.4: Schematics of active cell sorting techniques based on (A) femtosecond laser (B) dielectrophoresis (C) acoustic waves (D) piezoelectric transducer [330], and (E) magnetophoresis

makes it more biocompatible than other methods that use acoustofluidic [52], [56] or thermal-based [70] microdevice sorting techniques. Additionally, the strength of the impulsive force is determined by the pulse number, pulse energy, and pulse intervals of the fs-laser system [69], allowing for customized streamlining manipulation in a high-throughput system.

1.4. Aims and outline

Single-cell analysis and manipulation enable the identification and isolation of key samples from heterogeneous cell clusters. Although, by far, numerous techniques have been available, there are still many rooms for further improvement in device performance, such as understanding the detection mechanism of the impedance cytometry, and also the development of high-through cell sorting techniques.

In this dissertation, my purpose is to develop a FPGA-based system for single cell detection and manipulation. For the single cell detection, analysis, we reported a method for FPGA-based impedance cytometry system, and developed novel analysis method to extend the application of impedance cytometry. For example, my work demonstrated the capability of impedance cytometry to analyzing the morphology and intracellular components of single cells. Additionally, in my research, the FPGA-based Impedance cytometry was also shown to characterize the single bacteria. In order to accelerate the data analysis, a machine learning-based impedance detection system was developed, which enabled the fast antibiotic susceptibility testing for single bacteria.

As for the single cell manipulation, we employed a FPGA board to develop a control system. It has the capability of controlling the number of triggers for the femtosecond laser pulses. When the femtosecond laser pulses are focused in fluids, which results in the cavitation bubble and also shock waves. The previous work[51] has shown that femtosecond laser pulses can produce highly localized transient cavitation bubbles in a microchannel to kick target microparticles. In this dissertation, we further improved the sorting system through controlling the femtosecond laser pulses; The femtosecond laser induced force can be adjusted through laser pulses.

A detailed description of the system development and experiment verification can be found in each chapter of the dissertation, including six chapters:

Chapter 1: General introduction

This chapter introduced the development of techniques for single cell detection and sorting in recent years. It starts from the importance of single cell analysis; Aimed at key cells within inhomogeneous cell clutters or tissues, microfluidic flow cytometry provides a high-through and label-free means for single cell identification. Additionally, target cells can be separated from inhomogeneous cells using microfluidic cell sorting techniques. All relevant single cell detection and sorting techniques have been gone through in this chapter, and we also compared the advantages and disadvantages of each technique. In this dissertation, the impedance cytometry was employed for single cell detection, and femtosecond laser-based cell sorting system was used for single cell sorting.

Chapter 2: General experimental setups

The whole research was conducted based on Polydimethylsiloxane (PDMS) microfluidic devices. The impedance cytometry requires additional fabrication of microelectrodes on the glass slides. In this chapter, we detailly describe how to fabricate microfluidic devices and microelectrodes. Additionally, some common devices used during experiments are also introduced in this chapter.

Chapter 3: FPGA-based impedance cytometry

This chapter first introduced the basic mechanism of the impedance cytometry, and the development of FPGA-based impedance cytometry.

Secondly, microscale detection of single cells (size > 5 um) was performed. When suspended cells flow through the microelectrodes one by one, the impedance pulses are detected. Through analyzing these impedance pulses, we analyzed the relationship between impedance pulses and intra- or extra-cellular properties, including cell morphology, intracellular component density, and intracellular component distribution.

Lastly, this chapter discussed how to detect nanoscale targets, like single bacteria (size < 5 um), with impedance cytometry. Firstly, we presented a new design of impedance cytometry, namely parallel impedance cytometry, which has the capability of simplifying the post-processing of the nanoscale impedance detection. Additionally, a machine learning-based impedance system was proposed based on the parallel impedance cytometry. This system has the capability of processing impedance data and recognizing susceptible bacterial cells in real time.

Chapter 5: FPGA-based cell sorting control system

This chapter went through the mechanism of the femtosecond laser-induced cavitation bubble and acoustic forces. A FPGA-based control system was proposed to determine the number of femtosecond laser pulses based on the strength of detected fluorescence signal. Through controlling the pulse number, the femtosecond laser-induced force can be controlled, so that to realize the multi-sorting process of single cells.

Chapter 6: General conclusion

This chapter summarized all the research results in this dissertation, and presents the future plan of this research.

2. General experimental setups

2.1. Microfluidic chip

2.1.1. Microfluidic chip fabrication

The microfluidic device was fabricated by soft lithography of polydimethylsiloxane (PDMS) on a mold/master made using a negative photoresist (Su-8, 3010; Tokyo Ohka Kogyo, Tokyo, Japan) on a silicon wafer (4-inch. diameter). The PDMS (SYLGARD 184; Dow Corning, Midland, MI) was made by mixing a ratio of 10:1 w/w base-to-curing agent. Then, the mixed PDMS was poured over the master, degassed, and backed at 80 ℃ in an oven for 3 h to cure/crosslink the polymer. Following that, the PDMS microchannel part was cut and peeled off from the master, followed by cleaning with tape. Finally, the PDMS layer and a glass slide (76 × 26 × 0.8 mm, borosilicate glass) were treated with oxide plasma (Plasma Cleaner CY-P2L-B) for 1 min at 90 W prior to bonding together. All experimental parameters and conditions can be determined based on past experience[44], [71] and some references [72], [73].

2.1.2. Microelectrode fabrication

The channel is placed over two pairs of coplanar electrodes, each pair consisting of one source and one detection electrode. Each electrode is coated with a 70 nm thick layer of gold (Au) over a 70 nm thick layer of chromium (Cr). In accordance with some references[45], [74], [75], the electrode parameters were designed and arranged to perform as expected during experiments [44], [76].

2.2. General equipment

2.2.1. Autofluorescence during the impedance detection

Ultraviolet rays (U-ULH, OLYMPUS OPTICAL CO. LTD.) were employed to stimulate autofluorescence of *E. gracilis* cells, in order to illustrate the impedance detection and intracellular components distribution. The light source has a wavelength ranging from 450 nm to 490 nm, and the illumination power is 0.139 mW after a 20× object lens (NA: 0.5). Through a red-light filter, autofluorescence signals in the 648-709 nm wavelength region were exclusively recorded at a rate of 60 fps using a CCD camera (LU075C-IO, Lumenera Corp.). The suspension of *E. gracilis* cells was pumped into the device at a flow rate of around 0.1 μL/min during the video recording.

2.2.2. Optical system for the cell sorting

A motorized microscope stage (OptoSigma, BIOS-L101S) was used to mount the microfluidic chip upside down on an upright microscope (Olympus BX53). For sample loading (10 μL/min) and sheath flow loading (130 μL/min), two syringe pumps were used (Harvard Apparatus). Additionally, a high-speed camera (Ametek, Phantom V1211) was employed to capture the object motion over the entire period of single cell/bead sorting at a frame rate of 100,000 fps.

For fluorescence detection, an object lens (Olympus UPlanFL 20×, 0.5 NA air objective) was used to focus the laser beam onto single cells/beads as they flowed through the sorting area. The laser is a diode-pumped solid-state laser (488 nm, 40 mW). The fluorescence intensity was converted into voltage signals using a PMT (Edmund optics, 84-609). We used a bandpass filter with 530 nm central wavelength and a passband of 40 nm in conjunction with a pinhole to reject undesired wavelength bands. Notably, 530 nm was chosen as the bandpass wavelength to allow the detector to detect fluorescence emitted by either beads or cells.

For cell sorting, a regeneratively amplified Ytterbium laser femtosecond pulse laser (Spirit One, Spectra-Physics) was used. A 500 kHz repetition rate is set for the fs-laser system, which is set to generate fs pulses train with a center wavelength of 1040 nm. Due to the fact that cell sorting relies on the multi-photon absorption in fluids, which is not limited to the fs laser at this wavelength. Pulse pickers were equipped with acousto-optic modulators, which were controlled by the lab-made intensity discriminator to pick up a single-shot pulse from the pulse train. The fs pulse is then focused within the pocket structure using the same objective lens used for fluorescence detection [71].

3. FPGA-based impedance cytometry

3.1. Impedance system development and detection mechanism

3.1.1. Cell modeling

In impedance detection, as shown in Fig. 3.1A, individual particles perform as an insulator in the microchannel, and it would cause an increase in the resistance between electrodes. The fluctuation in the conductivity between electrodes can be monitored and transformed to impedance pulses. Electrical impedance is the ratio of the excitation voltage to the response current when a cell passes through the sensing zone.

$$\tilde{Z} = \tilde{V}/\tilde{I} \qquad \text{(Eq. 3.1)}$$

Where $\tilde{Z}$ is the electrical impedance, $\tilde{V}$ is the applied voltage, and $\tilde{I}$ is the response current.

The response current reflects the dielectric properties of target cells and host medium [72], [73]. As a particle or cell passes through the sensing zone, it causes an electric field change owing to the differences in permittivity or conductivity between the cells and the medium. Cells cannot be regarded as homogenous, and different components of cells, such as membrane and cytoplasm, should be modeled for estimating the complex permittivity of cells [74], [75]. The single-shelled spherical model (Fig. 3.1B), which is composed of a conducting sphere (cytoplasm) and an insulating thin shell (cell membrane), has been widely used to analyze the obtained results of impedance measurements [56,57]. Therefore, the complex permittivity of the cell $\tilde{\varepsilon}_p$ can be calculated as follows:

$$\tilde{\varepsilon}_p = \tilde{\varepsilon}_{mem} \frac{\gamma^3 + 2\left(\frac{\tilde{\varepsilon}_i - \tilde{\varepsilon}_{mem}}{\tilde{\varepsilon}_i + 2\tilde{\varepsilon}_{mem}}\right)}{\gamma^3 - \left(\frac{\tilde{\varepsilon}_i - \tilde{\varepsilon}_{mem}}{\tilde{\varepsilon}_i + 2\tilde{\varepsilon}_{mem}}\right)} \qquad \text{(Eq. 3.2)}$$

where $\tilde{\varepsilon}_{mem}$ and $\tilde{\varepsilon}_i$ refer to the complex permittivities of the cell membrane and cytoplasm, respectively; $\gamma = (R + d)\ /R$, where R and d represent the inner radius and membrane thickness of the cell, respectively.

For the suspension of cell/particle, the complex permittivity is generally simulated using Maxwell's mixture theory. The complex permittivity for the medium-cell mixture $\tilde{\varepsilon}_{mix}$ is

$$\tilde{\varepsilon}_{mix} = \tilde{\varepsilon}_m \frac{1+2\Phi\tilde{f}_{CM}}{1-\Phi\tilde{f}_{CM}} \qquad \text{(Eq. 3.3)}$$

where $\tilde{\varepsilon}_m$ represents the complex permittivity of the suspending medium, Φ is the volume fraction of the cell/particle to the sensing zone, and $\tilde{f}_{CM} = \left(\tilde{\varepsilon}_p - \tilde{\varepsilon}_m\right)/\left(\tilde{\varepsilon}_p + 2\tilde{\varepsilon}_m\right)$ is the Clausius-Mossotti factor.

For the cell-medium mixture, the complex impedance Z_{mix} is linked to its complex permittivity $\tilde{\varepsilon}_{mix}$ and can be calculated as

$$\tilde{Z}_{mix} = \frac{1}{j\omega\tilde{\varepsilon}_{mix}G_f} \qquad \text{(Eq. 3.4)}$$

where $j = \sqrt{-1}$, ω is the electric field frequency, and G_f is a geometric constant that depends on the geometry of the detection zone. For single-cell impedance analysis, the value of G_f is the ratio of the electrode area to the gap for an ideal parallel-plate electrode system. However, the electric field generated by microelectrodes is usually not uniform, and the issue of the divergent field should be corrected [76].

According to above equations, the dielectric properties of the particle/cell can be derived by measuring the complex impedance of the particle/cell suspension.

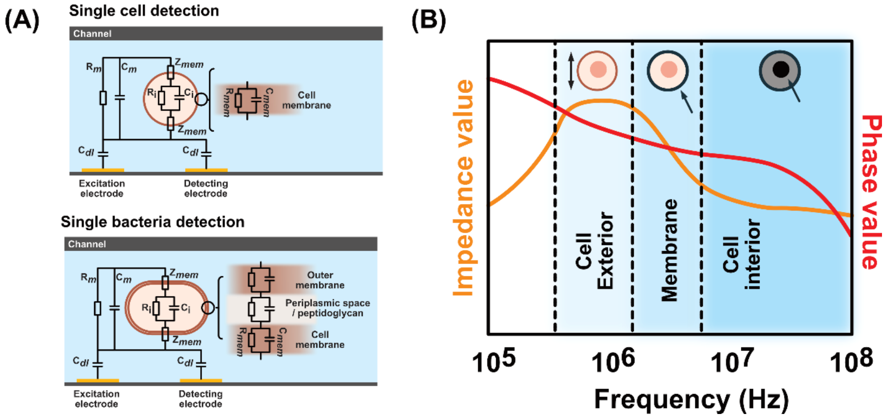

Fig. 3.1: Impedance cytometry mechanism. (A) Side view of the microfluidic channel showing a sample cell passing between the measurement and reference electrodes. (B) Spectra of impedance magnitude and phase, with indication of the cellular features probed in each frequency range.

3.1.2. Equivalent circuit modeling

Impedance signals reflecting the information of cells can be acquired when a single cell passes through the electrode sensing zone. When a direct current (DC) voltage is applied to the electrodes, the cell/particle can be considered a homogenous insulating spherical particle, and the signal strength is relative to the ratio of the cell volume to the channel dimension [77]. When the applied signal is an alternating current (AC) voltage, the single-shelled spherical cell model is used to model the cell and acquire detailed information regarding the cell itself [78], [79]. In 1989, Foster and Schwan proposed a simplified equivalent circuit model for simplifying the analysis of the system [80]. Generally, the resistance of the cell membrane is much larger than its capacitance and can be ignored; the capacitance of the cytoplasm can also be ignored because the capacitance is much smaller than its resistance. Therefore, as shown in Fig. 3.1A, the cell is approximated to a resistor that represents the cytoplasm (R_i) in series with two capacitors that describe the membrane (C_{mem}). In addition, the impedance is dependent on the medium resistance (R_m), medium capacitance (C_m), and electrical double-layer capacitance (C_{dl}). Electrical double-layer capacitance appears at the interface between the surface of the electrode and an adjacent liquid electrolyte [81]. Typically, C_{dl} increases with the surface area of the electrode. According to the equivalent circuit model, large C_{dl} and R_m can result in the attenuation of the measured particle and cell signals. Therefore, electrode with small electrical double-layer capacitance and liquid media with high conductivity are beneficial to high sensitivity cell sensing. Specifically, the values of other electrical components are described as follows:

$$R_m = \frac{1}{\sigma_m(1-3\Phi/2)G_f} \qquad \text{(Eq. 3.5)}$$

$$C_m = \varepsilon_\infty G_f \qquad \text{(Eq. 3.6)}$$

$$C_{mem} = \frac{9\Phi R C_{mem,0}}{4} G_f \qquad \text{(Eq. 3.7)}$$

$$R_i = \frac{4(1/2\sigma_m + 1/\sigma_i)}{9\Phi G_f} \qquad \text{(Eq. 3.8)}$$

Where $C_{mem,0} = \varepsilon_{mem}/d$ represents the specific membrane capacitance (per unit area), $\varepsilon_\infty \cong \varepsilon_m[1 - 3\Phi(\varepsilon_m - \varepsilon_i)/(2\varepsilon_m + \varepsilon_i)]$ represents the high-frequency permittivity at limit, and σ_m and σ_i represent the conductivity of the medium and cytoplasm, respectively.

The resistance of individual cells mainly comes from the cell membrane, which is frequency-dependent properties, as shown in Fig. 3.1B. In the equivalent circuit modeling, as the cell membrane and electrical double-layer are treated as capacitors, thus the C_{mem} and C_{dl} will change with the applied AC frequency (ω). In the low-frequency range ($\omega < 1\,MHz$), the electrical double layer dominates the system impedance; thus, the sensitivity for detecting a single cell is very low. As the frequency increases ($1\,MHz < \omega < 100\,MHz$), the electrical double-layer capacitance gradually decreases, and the system impedance is dominated by the cell size. At a higher frequency range ($\omega > 100\,MHz$), the system impedance mainly depends on the cytoplasm resistance, because the membrane capacitance is short-circuited in this frequency range. Foster and Schwan's equivalent circuit model provided good agreement with experiments for calculating single-cell impedance. However, cell membrane conductance and cytoplasm capacitance should also be considered in certain cases, such as electroporation and cell lysis. Under these circumstances, a complete equivalent circuit model that contains membrane resistance and cytoplasm capacitance is required. Sun et al. discussed the full details for calculating the values of R_i, C_i, R_{mem}, and C_{mem} [24], [82].

Before cell sensing, researchers usually sweep the impedance cytometry device in a certain frequency range to ensure no significant changes over the device impedance. Additionally, many researchers also calibrate the impedance signals of individual cells using standard polystyrene beads during each measurement.

3.1.3. Impedance signal processing

In electrical impedance measurement, Lock-in amplifier generates synchronized reference voltage signals [83], [84], which were an in-phase signal ($S_{rx} = A_r sin(\omega t)$), and an in-quadrature (90°-shift) reference signal ($S_{ry} = A_r cos(\omega t)$). At first, in-phase signal ($S_{rx} = A_r sin(\omega t)$) is connected to the electrodes as excitation and the resultant current signal (I_i) is measured. The current signal is then transformed to the voltage signal (S_i) on the transimpedance amplifier, and sent back to the lock-in amplifier.

On the assumption that input signal to the Lock-in amplifier is a sine wave given by:

$$S_i = A_i sin(\omega t + \theta) + B(t) \qquad \text{(Eq. 3.9)}$$

Where A_i, ω, and θ are the amplitude, frequency, and phase, respectively, and $B(t)$ is the noise signal. In order to obtain the impedance signal of the cytometry system, the input signal is modulated signals synchronized reference voltage signals, which were given by:

$$S_i \times S_{rx} = \frac{1}{2}A_iA_r cos(\theta) - \frac{1}{2}A_iA_r cos(2\omega t + \theta) + B(t) \times A_r sin(\omega t) \qquad \text{(Eq. 3.10)}$$

$$S_i \times S_{ry} = \frac{1}{2}A_iA_r sin(\theta) - \frac{1}{2}A_iA_r sin(2\omega t + \theta) + B(t) \times A_r cos(\omega t) \qquad \text{(Eq. 3.11)}$$

For impedance analysis, the amplitude and the phase information of the input signal were important metrics; both metrics belongs to DC components in the demodulated signals. To this end, the demodulated signals needed to be filtered to remove the AC signals and obtain DC signals. A very narrow band low-pass filter was applied to extract the DC signals. In this section, a finite impulse response (FIR) low-pass filter (LFP) was implemented. The outputs Z_X and Z_Y of the LPF are given by:

$$Z_X = \frac{1}{2}A_iA_r cos(\theta) \qquad \text{(Eq. 3.12)}$$

$$Z_Y = \frac{1}{2}A_iA_r sin(\theta) \qquad \text{(Eq. 3.13)}$$

where the Z_X is the real parts of impedance signal, and the Z_Y is the image parts. The impedance magnitude ($|Z|$) and phases (θ) can be defined as

$$|Z| = 2\sqrt{Z_X^2 + Z_Y^2}/\sqrt{2}A_r \qquad \text{(Eq. 3.14)}$$

$$\theta = \arctan(Z_X/Z_Y) \qquad \text{(Eq. 3.15)}$$

3.1.4. FPGA-based lock-in amplifier

The signal processing method coded on FPGA board was introduced in detail in my previous work [85]. In this section, we applied (Xilinx ZYNQ7020) to prepare the lock-in amplifier (LIA). Fig. 3.2 depicts the detection algorithms. The codes were compiled using VIVADO 2020.2. Inside the FPGA platform, a digital signal generator generates the reference signals (i.e., the in-phase and quadrature signals), one of which is given as the excitation voltage for the impedance cytometry. In the experiment, the frequency generated in Lock-in amplifier is equal to the frequency of the signals to be measured from the output sides. Then, the measured voltage signals were modulated with the in-phase and quadrature signals via digital multipliers in real time, resulting in two components (i.e., DC components and high-frequency components). Notably, when calculating modulation, each frequency component in a multi-frequency signal can be isolated from the others. For example, in the case of two detection frequencies, the output of this step includes four signal components. For each isolated frequency, this step produces two signal components. After that, the outputs were sent to the next stage – the cascaded integrator–comb (CIC) filter cascade, in which the sampling frequency was reduced to 10 KSPS to eliminate most high-frequency components. To further reduce noise, I used a finite impulse response (FIR) filter with an order of 101 (Peled and Bede Liu, 1974). The filter design was achieved using MATLAB 2020a (Mathworks Inc., Natick, USA). The outputs from the FIR filter were converted to analog signals again (DIGILENT Pmod DA2, National Instruments), recorded by the data collection system (USB-6363 BNC, National Instruments, USA) and presented in computer. Detection throughput is limited by the time it takes for the system to process signals. Since the processing time of the developed system is set to 100 μs, the highest throughput of the detection system is about 125 k samples/s. It is worth mentioned that the developed FGPA-based lock-in amplifier can realize the simultaneous detection of signals with up to 4 frequencies. Moreover, by simplifying the signal processing codes, the detection throughput (125 k samples/s) can be further improved.

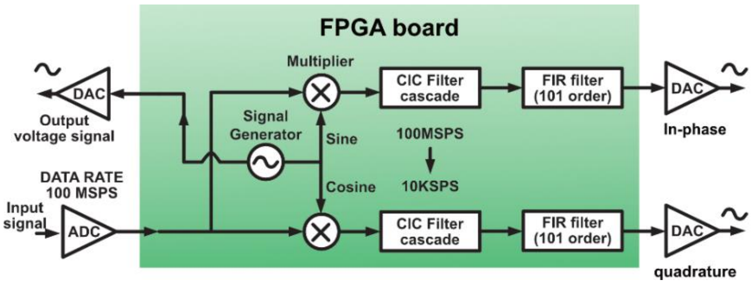

Fig. 3.2: FPGA-based Lock-in amplifier and involved digital signal processing methods.

Table 3.1 summarizes the advantages of FPGA-based lock-in amplifier over other approaches. As a first advantage, the FPGA enables the fast development of the lock-in amplifier, as it is programmable. Circuits can be designed and verified at any time, and several plans can be tried in a short time to find the best one. However, traditional PCB-based lock-in amplifiers take a long time to design and manufacture [86], making it difficult to find the best design through trial and error. FPGA-based lock-in amplifiers are more resistant to environmental noise than circuit-based ones. In noisy detection environments, circuit-based lock-in amplifiers are more likely to be susceptible to static or electromagnetic interference, compared to FPGA-based systems. As the PCB board is nonadjustable once fabricated, it is impossible to adjust the circuit layout to deal with background noise[87]. In contrast, an FPGA-based lock-in amplifier can change its "circuit" by modifying its programs and adding real-time denoising algorithms, so that to improve the signal-to-noisy ration of the output signals. Additionally, an FPGA-based lock-in amplifier processes digital signal instead of analog signal in detection, but most conventional circuit-based systems can only work with analog signal. It is known that a digital signal (in comparison to an analog signal) is inherently more immune to noise. Additionally, similar to the FPGA board, the Arduino board is also programmable and works with digital signals. The limitation of Arduino-based lock-in amplifiers [88] is their processing speed, as their response time is a few hundred microseconds, whereas FPGA boards can process on a nanosecond scale. A high-process speed is essential for lock-in amplifier especially in the case of high-detection frequencies. When digitalizing the measured signal, the AD converter on Arduino boards has a processing speed between 50 kHz and 200 kHz for maximum resolution, while the FPGA board can sample at over 100 MHz. Furthermore, the AD converter of Arduino board can only achieve 10-bit resolution, while the FPGA used in this study can achieve 14-bit resolution. In other words, despite Arduino-based lock-in amplifiers being able to accomplish the same tasks as FPGA-based ones, they are still not as efficient or effective as their FPGA-based counterparts.

Table 3.1: Comparison of different types of lock-in amplifiers

	FPGA (Eclypse Z7) [44], [89]	**PCB circuit** [86], [87]	**Arduino (Uno Rev 3)** [88]
Programmability	Yes	No	Yes
Noise resistance	Strong	Poor	Normal
Sampling rate	> 100 MHz	~	50 ~ 200 kHz
Digitalization resolution	14 bits	~	10 bits
Applicable detection frequency	< 50 MHz	Up to gigahertz scale	< 1 MHz

3.1.5. Impedance cytometry

As shown in Fig. 3.3, the impedance cytometry was built on a FPGA board (Diligent Eclypse Z7, USA), which has two roles: (1) Signal generator, capable of generating AC signals with specific detection frequencies on the central electrode; (2) Lock-in amplifier, capable of analyzing impedance pulses by deconvoluting differential voltages of both detection electrodes. Specifically, for the detection voltage, an AC signal is generated on the FPGA board by a digital-to- analog converter (Zmod DAC, Digilent Inc., USA) with a maximum current output of 4 mA. With such low current, the voltage signal is safe for target cells, meanwhile a similar and even higher voltage have been employed on mammalian cells safely [73], [90], [91]. The function and working mechanism of the FPGA-based lock-in amplifier [44] have been introduced before. The current fluctuation induced by single cells would be converted to digital impedance signals in the developed FPGA-based lock-in amplifier. After that, all digital signals are converted to analog signal through an DA converter (i.e., Pmod DA2), in order to collect all impedance data via a DAQ device (USB-6363). As a result, all measured impedance signal can be shown and stored in the computer. In this work, our system is applicable for the signal analysis with up to four frequencies, which is controlled by our programs via the FPGA board. The maximum number of frequencies that can be applied is limited by the connector ports on the FPGA board. Furthermore, the latest commercial device is also limited to four-frequency detection, which is the same as ours.

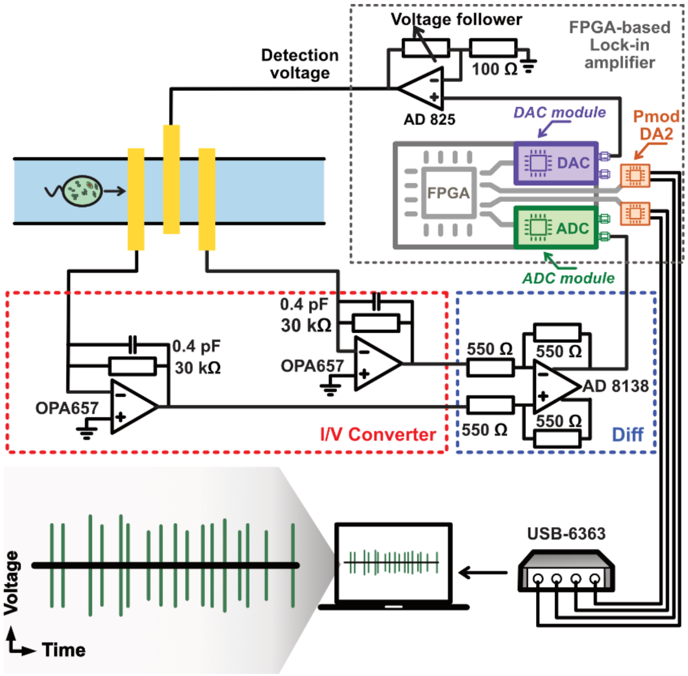

Fig. 3.3: Impedance cytometry system. When single cells flow through the detection channel, the induced fluctuation on the electrodes would be monitored and converted to the impedance signals via the FPGA-based lock-in amplifier. All impedance signals were converted to analog signal via the DA converters (Pmod DA2) and collected via the data

acquisition device (USB-6363). Eventually, the collected impedance signals are shown as waveforms in the computer in real time.

For the impedance detection, current propagates from the central electrodes to both detection electrodes, and are transferred to voltage signals by transimpedance amplifiers (I/V converter). The transimpedance amplifier is made with operational amplifier (OPA 657U), and the feedback resistor is selected as 33 kΩ. The bandwidth of the transimpedance circuit is 16.55 MHz, therefore it can stably convert current to voltage signals with a magnitude gain of 90.36 dB for 500 kHz signals and 89.95 dB for 6 MHz signals. Afterward, voltage signals get differential on differential amplifier (Diff, see Fig. 3.3A), and the resultant voltage signals were captured by an analog-to-digital converter (Zmod ADC, Digilent Inc., USA) on the FPGA board at a sampling rate of 100 MHz.

As for the collection of impedance signals, all processed impedance pulses are converted back to analog voltage by a digital-to-analog converter (Pmod DA2, Digilent Inc., USA) in real time. The analog voltage is then recorded using the data acquisition system (USB-6363 BNC, National Instruments, USA) at a sampling rate of 125 kHz and shown in computer in real time using NI DAQExpress (National Instruments, USA).

3.2. Microscale detection of single cells

3.2.1. Single cell shape detection

3.2.1.1. Experiment purposes and preparation

In this section, I investigated the ability of impedance flow cytometry to measure the shape of single cells/particles. I found that the impedance pulses triggered by micro-objects that are asymmetric in morphology show a tilting trend, and there is no such a tilting trend for symmetric ones. Therefore, I proposed a new metric, tilt index, to quantify the tilt level of the impedance pulses. The value of tilt index tends to be zero for perfectly symmetrical objects, while the value is greater than zero for asymmetrical ones. Also, this metric was found to be independent on the trajectories (i.e., lateral, and z-direction shift) of the target micro-object. In experiments, I adopted a home-made lock-in amplifier and performed experiments on 10 μm polystyrene beads and *Euglena gracilis* (*E. gracilis*) cells with varying shapes. The experimental results coincided with the simulation results and demonstrated that the new metric (tilt index) enables the impedance cytometry to characterize the shape single cells/particles without microscopy or other optical setups.

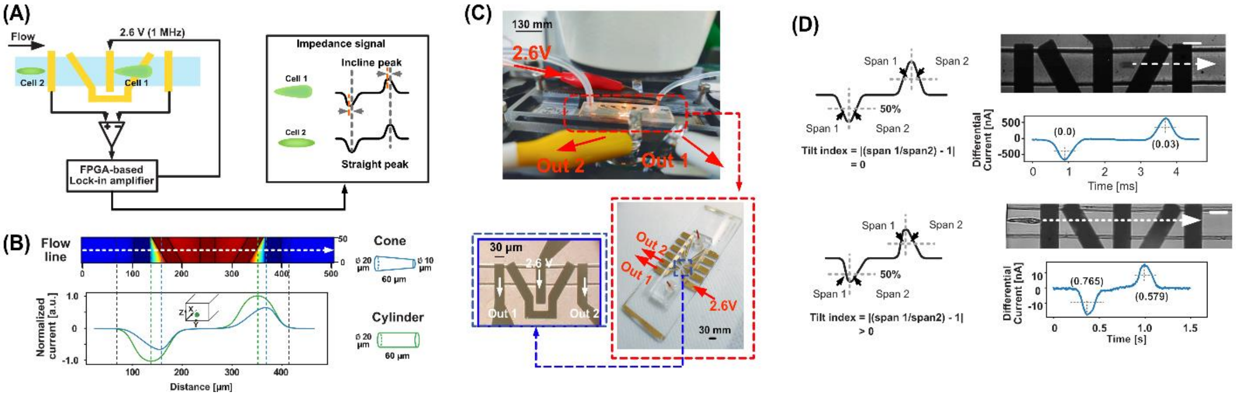

Fig. 3.4: The developed microscopic impedance cytometry for quantifying single-cell shape. (A) Schematic of the impedance-based single-cell shape detection system. This case uses a detection frequency of 1 MHz, which is not sufficient to cross the cell membrane but can only be used for exterior detection. (B) Simulation analysis for symmetric (Cylinder, Radius: 10 μm, Length: 60 μm) and asymmetric micro-objects (Cone, Radius: 5 μm and 10 μm, Length: 60 μm), both starting from the same location (Y=25 μm, Z = 15 μm). (C) Experimental setup and the layout of the electrodes. (D) Experimental results of impedance pulse for a 10 μm spherical polystyrene bead and an asymmetric *E. gracilis* cell. The scale bar represents 30 *μ*m.

Considering the length of *E. gracilis* ranges from 10–100 μm in this section, the impedance cytometry involved a non-parallel floating electrode to separate each sensible region, so that to leave enough blank space for *E. gracilis* and to avoid the existence of *E. gracilis* at both sides of differential impedance cytometry at the same time. The floating electrode can create a triangle-shaped electric field, which enables the tracking of single particles [92], and as shown in Fig. 3.4B, two detection areas are separated by an equipotential region (i.e., undetectable region). As for the parameters of the impedance cytometry, the microchannel in detection area is 50 μm wide, 35 μm high and 290 μm long. Electrodes are 30 μm wide, and the distance between the input electrode and the output electrode is 100 μm, and the distance between the output electrode and the floating electrode is 5μm on the shortest side and 35μm on the other side

As shown in Fig. 3.4D, the impedance pulse for 10 μm beads is not tilted, but the impedance pulse triggered by *E. gracilis* is tilted due to the asymmetric shape of *E. gracilis*. To better characterize this phenomenon, I provided a new metric – tilt index, defined as:

$$tilt\ index = \left|\frac{span\ 1}{span\ 2} - 1\right| \qquad \text{(Eq. 3.16)}$$

The critical line is 50% peak value, and the tilt index is calculated as the ratio of the time spans on either side of the pulse peak and then subtracted by one, so that the metric is independent on the time-related parameters (i.e., flow rate) and is always greater than or equal to zero. Theoretically, spherical beads have a tilt index of almost zero, and the tilt index of most *E. gracilis cells* is greater than zero. More specifically, the tilt index tends to be zero for symmetric objects, while the tilt index tends to be greater than zero for non-symmetric objects. The degree of asymmetry of an object can also be quantified as a specific value by the tilt index.

3.2.1.2. Experimental results and discussion

Fig. 3.5 depicts the experimental results on thousands of beads and cells, which compares the distribution of the tilt index of both samples. In Fig. 3.5A, the tilt index is distributed in a range from 0.113 to 0.440 for 50% *E. gracilis* cells, and for 10 μm beads, half of them is distributed in a range from 0.027 to 0.100. In Fig. 3.5(A-i), the median of 10 μm beads (0.050) is much closer to zero than the that of *E. gracilis* cells (0.319), coinciding with the simulation results that the tilt index of symmetric objects tends to be zero. For 10 μm beads, a small interquartile range (0.073) implies a stable size distribution, while for *E. gracilis* cells, the interquartile range (0.327) strongly indicates that the size distribution of *E. gracilis* cells is unstable and fluctuates in a wide range (see Fig. 3.5 (A-ii)).

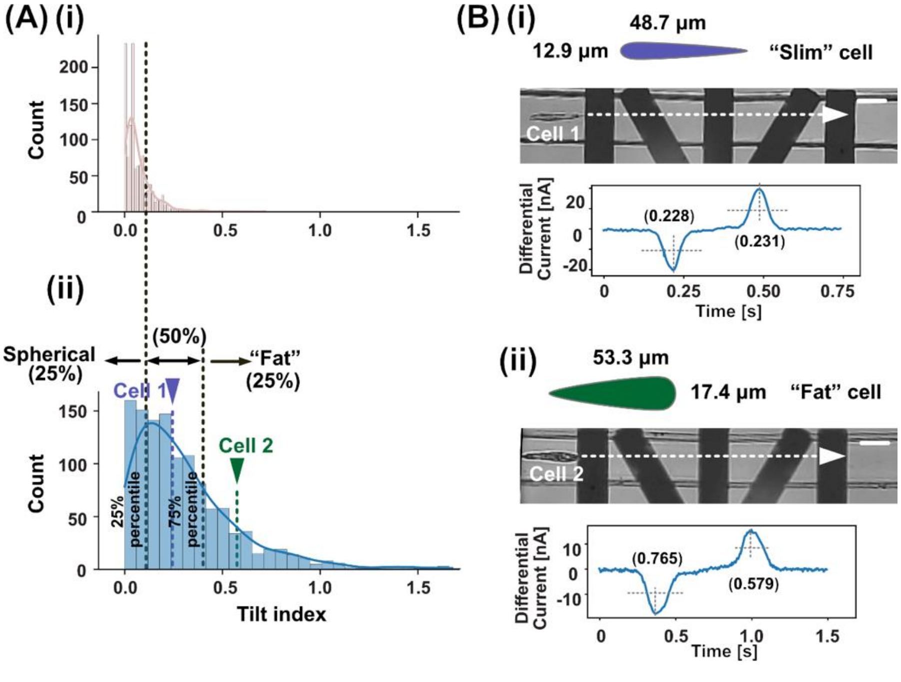

Fig. 3.5: Comparison of tilt index of impedance signals for 10 μm polystyrene beads and E. gracilis cells. (A) Data distribution of the tilt index for (i) 10 μm polystyrene beads (CV: 1.093) and (2) E. gracilis cells (CV: 0.911). (B) Impedance signals triggered by E. gracilis cells of different shapes. The scale bar represents 30 μm.

Specifically, the impedance pulses triggered by 10 µm beads are almost symmetrical (tilt index ≈ 0), but the pulse is inclined (tilt index > 0) for *E. gracilis* cells. As shown in Fig. 3.5B. When a *E. gracilis* cells (Cell 1: 48.7 µm long and 12 µm wide) flowed through the electrodes, both impedance pulses were tilted, and corresponding tilt index was 0.231. In another case, when Cell 2 (53.3 µm long and 17.4 µm wide) passed through the detection area, it induced an impedance signal that has a tilt index of 0.579. Same as the simulation analysis, a "fat" *E. gracilis* cell (Cell 2) has a greater tilt index than a "slim" one (Cell 1).

Through comparison, the results shown that 75% of 10 µm spherical beads have a tilt index of smaller than 0.10, but the tilt index of most *E. gracilis* cells fall within a range from 0.113 to 0.440. Moreover, I found that the value of tilt index is closely related to the shape of *E. gracilis* cells. Half of the *E. gracilis* cells in this study (0.113 < tilt index < 0.440) should have a "slim" shape and look like an elongated cylinder as Cell 1; *E. gracilis* in the other group (tilt index > 0.440), have a "fat" body and should have more paramylon inside, like Cell 2; and the rest group (tilt index < 0.113) of *E. gracilis* have a similar tilt index to the 10 µm beads and should be approximately spherical or cylindrical in shape.

Notably, the repeatability of the analysis method can be verified through comparing the distribution of the tilt index of beads and E. gracilis cells, as shown in Fig. 3.5. All polystyrene beads share a similar morphology and are perfect spheroid shapes, their tilt indexes were distributed in small range, in Fig. 3.5A(i). In contrast, E. gracilis cells are diverse in their shape, resulting in tilt indexes ranging widely between 0 and 1, in Fig. 3.5A(ii). The relation between the object shape and the tilt index can be solidly supported by the difference in distribution range. As for the measurement precision, currently, we only can detect asymmetric level of single objects in their morphology. By comparing cell imaging and their impedance pulses, different tilt indexes can be related to cells with visible differences. At present, the measurement precision is approximately micrometer scale, and it can be further improved in the future.

3.2.1.3. Summary

Overall, I developed a new method for measuring the shape of single cells by impedance cytometry. This is achieved based on the phenomenon that impedance pulses of asymmetric micro-objects show a tilting trend. Using a new metric, namely the tilt index, the shape of asymmetric single cells/particles can be quantified as a non-zero number. Also, the tilt index increases with the increase of the asymmetric level of micro-objects. In contrast, the tilt index is around zero for the symmetric micro-objects (e.g., sphere or cylinder).

3.2.2. Cell volume and intracellular components

3.2.2.1. Experiment purposes and preparation

Intracellular components (including organelles and biomolecules) at the submicron level are typically analyzed in situ by special preparation or expensive setups. Here, a label-free and cost-effective approach of screening microalgal single-cells at a subcellular resolution is available based on impedance cytometry. To the best of my knowledge, it is the first time to show the relationships between impedance signals and submicron intracellular organelles and biomolecules. Experiments were performed on E. gracilis cells incubated under aerobic conditions and 15 μm polystyrene beads (reference) at two distinct stimulation frequencies (i.e., 500 kHz and 6 MHz). Detection frequencies were determined based on the properties to be detected. The low detection frequency (500 kHz) can be employed to characterize the shape and volume of single cells, as 500 kHz current cannot cross the cell membrane and mainly propagates around the cell in the microchannel. The cell membrane shows high resistance to the low-frequency current. In contrast, high frequency (6 MHz) current is able to cross the cell membrane and detection cell interior. Thus, the high frequency (6 MHz) is employed to characterize the intracellular components.

Based on the impedance detection of tens of thousands of samples at a throughput of about 900 cells/s, three metrics were used to track the changes in biophysical properties of samples. As a result, the electrical diameters of cells showed a clear shrinkage in cell volume and intracellular components, as observed under microscope. The morphology metric of impedance pulses (i.e., tilt index) successfully characterized the changes in cell shape and intracellular composition distribution. Besides, the electrical opacity showed the stable ratio of the intracellular components to cell volume under the cellular self-regulation. Additionally, simulations were used to support these findings and to elucidate how submicron intracellular components and cell morphology affect impedance signals, providing a basis for future improvements. This work opens up a label-free and high-throughput way to analyze single-cell intracellular components by impedance cytometry.

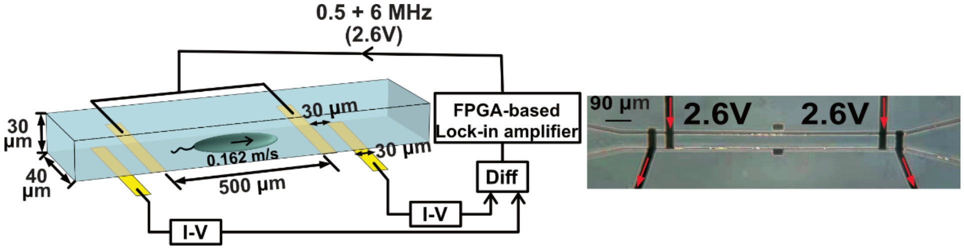

Fig. 3.6: Principles of probing the changes in the volume and intracellular component of E. gracilis cells by impedance cytometry. Differential-electrode microfluidic impedance chip. Individual cells are measured simultaneously at two frequencies (i.e., 500 kHz and 6 MHz) using a FPGA-based LIA.

Fig. 3.6 depicts the concept of the detection system. A straight microfluidic channel (Dimensions: 40 μm width, 30 μm high) was placed over two pairs of coplanar electrodes (Materials: gold (Au) and chromium (Cr)), and each pair has one source and one detection electrode (Dimensions: 30 μm wide, 30 μm edge-to-edge span, and 500 μm span between two pairs of electrodes). As for the impedance detection system, a FPGA-based lock-in amplifier (LIA) was used to stimulate the source electrode with a 2.6 V AC signal at two frequencies (i.e., 500kHz and 6MHz) simultaneously. The current signals from two detection electrodes were transferred to voltage signal and subtracted using custom-designed transimpedance amplifier (I-V) and a differential amplifier (Diff), respectively. Lastly, the resulted voltage signal was captured by FPGA-based LIA for the impedance analysis.

As one type of algae, *E. gracilis* has one layer of plasma membrane like animal cells, but it contains chloroplasts, which is easy to observe under microscope, facilitating the determination of the organelles/biomolecules in cells. In order to stimulate and record the changes in cell morphology and intracellular components, *E. gracilis* cells were cultured in aerobic environments and measured every 24 h for 3 days without any external nutrients.

3.2.2.2. Simulation analysis

Here, two stimulation frequencies (500 kHz and 6 MHz) were used to maximize the performance of the developed impedance cytometry, and a complete single-cell characterization in terms of cell volume, and the intracellular components was conducted. As shown in Fig.

3.7(A), two detection frequencies corresponded to different cell membrane conductivity. The membrane conductivity curve has been verified in several works [45], [98].

The high frequency ($|Z_{HF}|$, 6 MHz) was determined based on single shell model of cells [93]–[95], through which the plasma membrane is conductive and high-frequency current can pass through the cytoplasm of single cells, inducing the impedance dependency on intracellular properties. In contrast, the low frequency ($|Z_{LF}|$, 500 kHz) field was shielded from the outside by the cellular membrane, and thus the impedance signals showed a dependency on the cell volume. Compared with polystyrene beads (frequency-independent insulators), high-frequency conductive cells exhibited lower opacities (ratio of $|Z_{HF}|/|Z_{LF}|$).

In detail, at a low frequency (500 kHz), the impedance signal directly correlates with cell volume. Thus, changes in cell size can be presented as the changes in the amplitudes of impedance pulses, respectively. Besides, the low frequency impedance is less influenced by the volume and distribution of intracellular components, since the membrane show high resistance to the low frequency field. Therefore, for cell morphology, the volume change can be traced through low-frequency electrical diameter ($|Z_{LF}|^{1/3}$). In contrast, at a high frequency (6 MHz), the plasma membrane is no longer a perfect insulator, and the conductivity of intracellular components affects high-frequency impedance signals. Thus, changes in high-frequency electrical diameter ($|Z_{HF}|^{1/3}$) can be attributed to changes in the volume of intracellular components. Lastly, the occupancy of intracellular organelles/biomolecules in single cells are denoted by electrical opacity ($|Z_{HF}|/|Z_{LF}|$) in this work. Of note, the detection system was calibrated based on the impedance signals of 15 μm polystyrene beads, which have well-defined size (CV < 1%) and almost perfect insulation (< 355 MHz in 1× phosphate-buffered saline (PBS)) [73].

Experiments were performed at five different time points (i.e., 0 h, 12 h, 24 h, 48 h and 72 h) for the control and anaerobic groups. During the three-day experiment, all *E. gracilis* cells were grown in diluted medium to maintain the viability and proliferation of the anaerobic group. In the absence of adequate nutrients, *E. gracilis* cells are forced to consume stored carbohydrates (i.e., paramylon) and reduce organelles to sustain life, as evidenced by the reduction in cell volume and intracellular chloroplasts.

Additionally, 15.6 μm polystyrene beads (Polysciences, USA) were diluted using 1× phosphate-buffered saline (PBS) to a concentration of 1120 beads/μL. The physical property of beads is frequency-independent, which is treated as perfect insulator in this case and used as reference for the impedance detection. Notably, all samples were transferred to 1× PBS solution, loaded into a syringe and injected by a syringe pump to the detection area in the microchannel at a flow rate of about 0.162 m/s.

Table 3.2: Simulation parameters

Parameters	Value
Channel length	300 μm
Channel depth	30 μm
Relative permittivity of membrane	5
Relative permittivity of cytoplasm	50
Conductivity of cytoplasm	0.5 S/m
Electrodes wide	30 μm
Electrode span	30 μm
Relative permittivity of 1× PBS	80
Conductivity of 1× PBS	1.34 S/m

Before experiments, the numerical simulations were employed to show the varying conductivity of the cell membrane at different detection frequencies. Electrical model of single cells [96], [97] has been introduced in detail in Section 3.1.2, which includes the resistance (R_{PBS} and C_{PBS}) of the diluted PBS solution in which *E. gracilis* cells are suspended, resistance and capacitance of the cytoplasm (R_C and C_c), and impedance of the plasma membrane (Z_M). The electrical double layer of electrodes was not taken into consideration in this work, since it has little effect on the detection at the two applied frequencies [93].

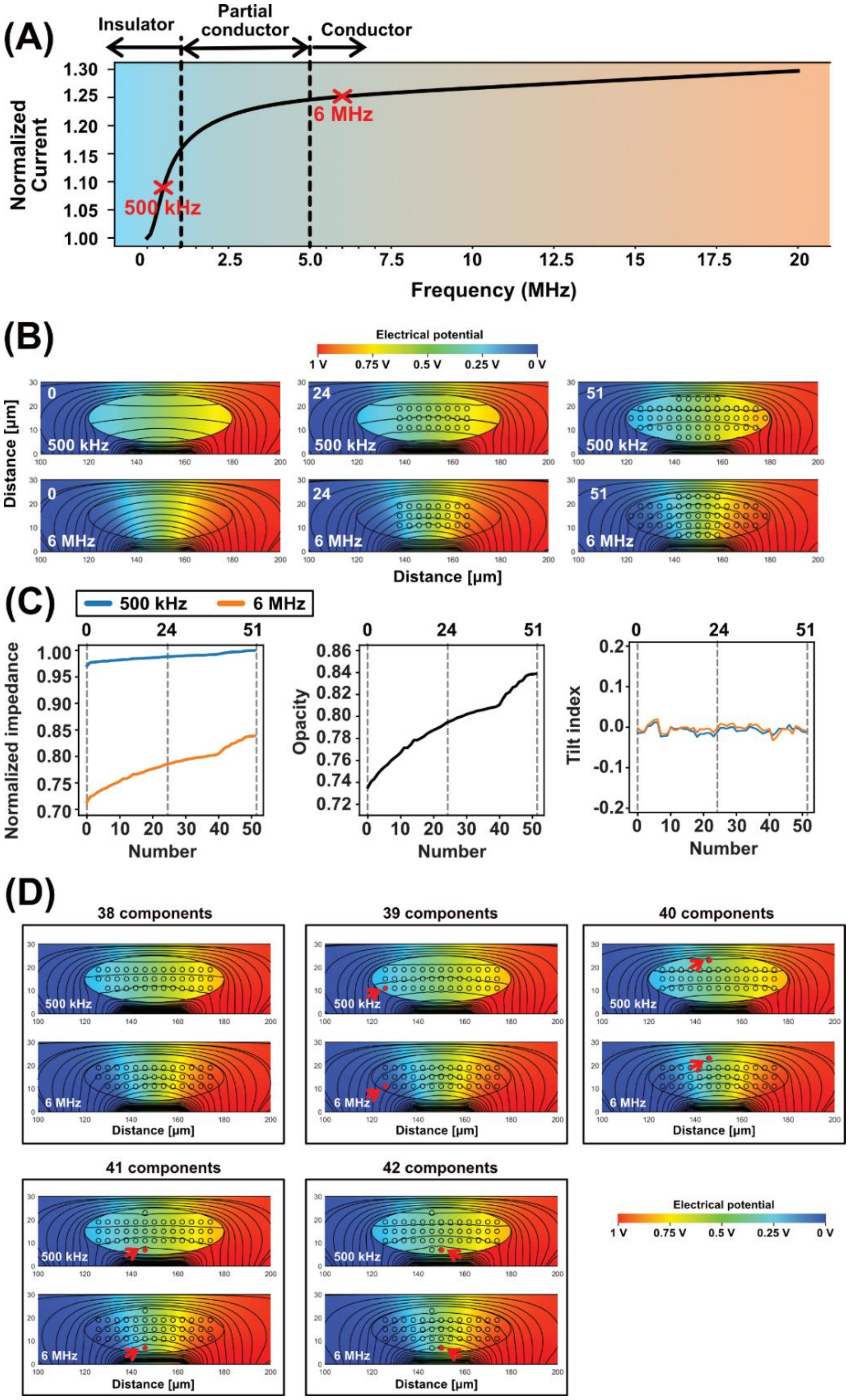

Fig. 3.7: Numerical simulation results for *E. gracilis* cell model at two frequencies. (A) Current signals at different frequencies, and electronic potential distribution at low (500 kHz) and high (6 MHz) frequencies. Streamlines indicate the current density. (B) Illustrations of the changes in the distribution of the electronic potential as the number of intracellular components increase from 0 to 51. The blank lines denote the current signals. (C) The relationship of impedance signals with the volume of intracellular components,

which is presented through normalized impedance, opacity, and the tilt index. (D) Distribution of intracellular components changes when the number of intracellular components increases from 38 to 42.

All simulations were performed via COMSOL Multiphysics 5.6 (COMSOL Inc., Burlington, MA, USA), which are focus on investigating the response of single electrode pair for simplicity. *E. gracilis* cells (see Fig. 3.7A) were considered as a 2D ellipse (Radius: 30 μm long-axis, 10 μm short-axis) in the model, as most of them are cigar shaped. Besides, the cell membrane (10 nm) was modelled using the contact impedance approximation rather than the full-fidelity thin-layer geometry, which greatly simplified numerical calculations while ensuring reliable analysis [98], [99]. Additionally, organelles and biomolecules are all simplified as 2D circles (Dimensions: 1 μm radius, 2 μm span) with twice the thickness of the cell membrane (20 nm), because chloroplasts have a double membrane envelope. The impedance signal can be obtained through calculating the current signal when particles move along the centerline under the stimulation of two frequencies (i.e., 500 kHz and 6 MHz) simultaneously. Other parameters of cells used for the simulation [96], [100] are shown in Table 3.2.

As shown in Fig. 3.7A, intracellular components (e.g., organelles) were uniformly placed in the cell and packed by the cell membrane for the *E. gracilis* cell model. The current signal in the detection area gradually increases when frequency increases from 0 to 20 MHz. At low alternative current (AC) frequency (< 1 MHz), the cell behaves as an insulator, and the dependence of low-frequency impedance on the AC frequencies are associated with the properties of the suspension solution (i.e., ×1 PBS). At intermediate frequencies (1-5 MHz) [73], the dielectric properties of the cell membrane dominate the measured impedance spectrum, and the resistance of the cell membrane to the current signal decreases with the increase of AC frequency. At higher frequencies (>20 MHz), the electric field can cross all cell membrane, and the impedance signals are totally dominated by the conductivity of cell cytoplasm. In this work, I chose 6 MHz as the high detection frequency because it can cross cell membrane with a single molecular layer but should not be possible for organelles having double membranes (i.e., chloroplasts).

Fig. 3.7B shows the effect of intracellular components (e.g., organelles) on the impedance at both frequencies. First, as the number of intracellular components increases from 0 to 51, the amplitudes of the low-frequency and high-frequency impedance signals increase, but the high-frequency increases much faster than the low-frequency (see Fig. 3.7C). This is because of the high resistance of the cell membrane to the low-frequency current signals, and in turn, the low-frequency impedance shows low sensitivity to the changes in the total volume of intracellular components. Of note, all impedance signals in Fig. 3.7C are normalized to the impedance value of the cellular model containing 51 intracellular components. In addition, the opacity shows a similar trend to the high frequency impedance signals as the number of intracellular components increases. Since the low- ($|Z_{LF}|$) and high-frequency ($|Z_{LF}|$) impedance signals show a linear relationship with the volume of the target cell and the intracellular components, respectively, and the opacity ($|Z_{HF}|/|Z_{LF}|$) is dependent on the intracellular density to some extent. In contrast, there is almost no relationship between the tilt index and the volume of intracellular components, as the tilt index fluctuates around 0 for both high-frequency and low-frequency signals.

A sudden change in the slope of the tilt index curve can be observed in Fig. 3.7C, which can be attributed to the change in intracellular component layout. Fig. 3.7D illustrates the layout of intracellular components with the component number ranging from 38 to 40. When the number of intracellular components exceeded 40, the components were added up and down the cell interior.

Thus, I estimated that intracellular layout is responsible for the sudden change in tilt index curve at the 40 intracellular components.

3.2.2.3. Experimental results and discussion

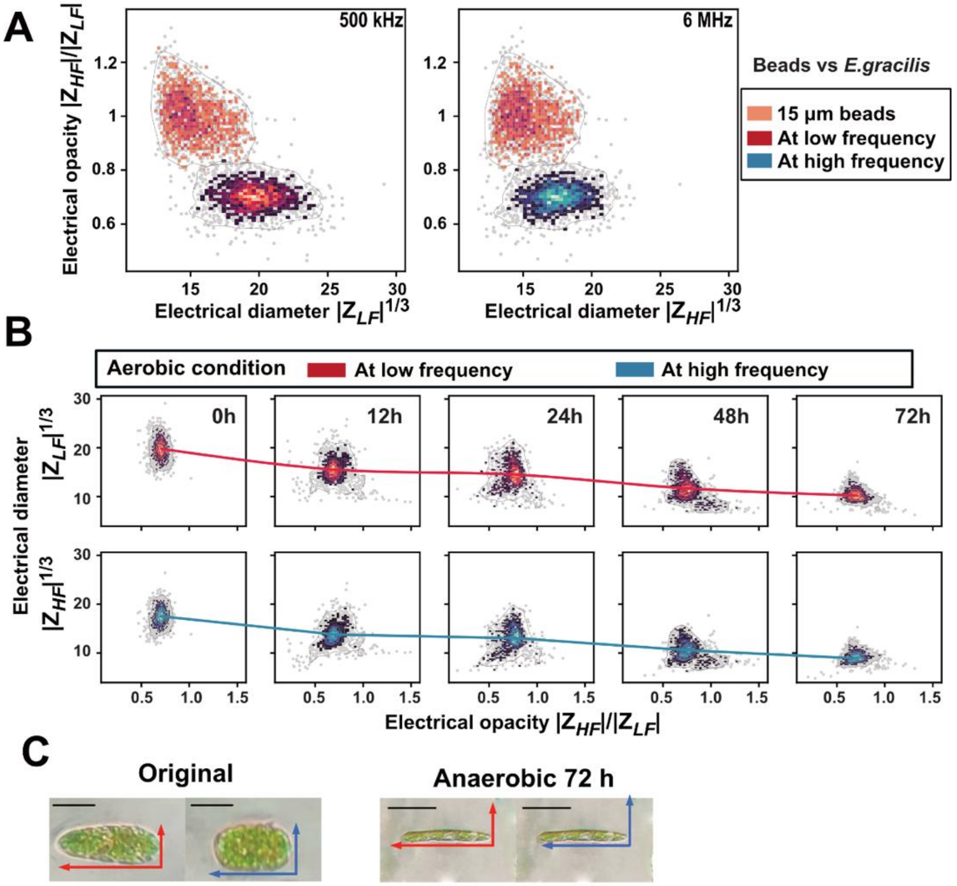

Fig. 3.8: Impedance analysis based on the electrical opacity and electrical diameter. (A) Impedance scatter plots of *E. gracilis* cells (2000 events) and 15 µm polystyrene beads (2000 events) that are used as a reference. The x-axis is the cube of the impedance (proportional to the diameter). (B) Time course of changes in the impedance scatter plots (i.e., electrical diameter vs. electrical opacity) of E. gracilis cells cultured with (aerobic) or without air (anaerobic) within three days.

Insufficient nutrition specifically affects the intracellular components, forcing *E. gracilis* cells to consume stored energy (e.g., paramylon) and adjust the volume of organelles (e.g., chloroplasts) to sustain life. Living conditions (i.e., aerobic or anaerobic) determine how *E. gracilis* cells convert stored carbohydrates into energy and the efficiency of the conversion. With self-consumption, a number of phenotypic changes in the cell shape, volume, as well as in the distribution of intracellular components occur, leading to the changes in dielectric properties.

15 µm polystyrene beads having well-defined dielectric properties and diameter are used to calibrate the device and eliminate the effects of device variations and non-linearities in the electronical measurement [73]. All cell impedance data were normalized by a single linear multiplier to ensure 15 µm beads have a median opacity of 1 and a median electrical diameter of 15 (see Fig. 3.8A). For the original *E. gracilis* samples, they had a low-frequency electrical diameter ($|Z_{LF}|^{1/3}$) of about 16-23 µm and a high-frequency electrical diameter ($|Z_{HF}|^{1/3}$) of 15-20 µm for intracellular components, with an electrical opacity of about 0.75. The low-frequency electrical diameter was similar to the optical diameter in Fig. 4C. In this work, I hypothesized that high-frequency impedance signals can determine the volume and distribution of intracellular components, which has been verified through the simulation analysis. Besides, the low-frequency electrical diameter ($|Z_{LF}|^{1/3}$) should scale with the cell volume, which is also supported by the optical diameter in Fig. 3.8C, and the high-frequency electrical diameter ($|Z_{HF}|^{1/3}$) should scale with the equivalent volume of intracellular components.

During 3-day experiments, clear electrical diameter shifts were observed (see Fig. 3.8B). This is because the nutrients in the medium were not sufficient for *E. gracilis* cells to maintain a fat body, and they began to shrink in size. After 3 days of starvation, the low-frequency electrical diameter of *E. gracilis* cells (~ 19.64 µm) shrank by about 48% (~ 10.17 µm) under aerobic conditions. The high-frequency electrical diameter (~ 17.5 μm) was reduced by 47.6% (~ 9.14 μm) under aerobic. Furthermore, although electrical diameters decreased, their electrical opacity remained almost unchanged, which can be attributed to the self-regulation mechanism of cells [101]. Here, electrical opacity is defined as the ratio of cell volume to intracellular component volume, namely occupancy. The volume reduction of *E. gracilis* can also be seen under the microscope (×40) as shown in Fig. 3.8C, where the length of *E. gracilis* is almost the same and the contraction occurs mainly in the width of cell samples.

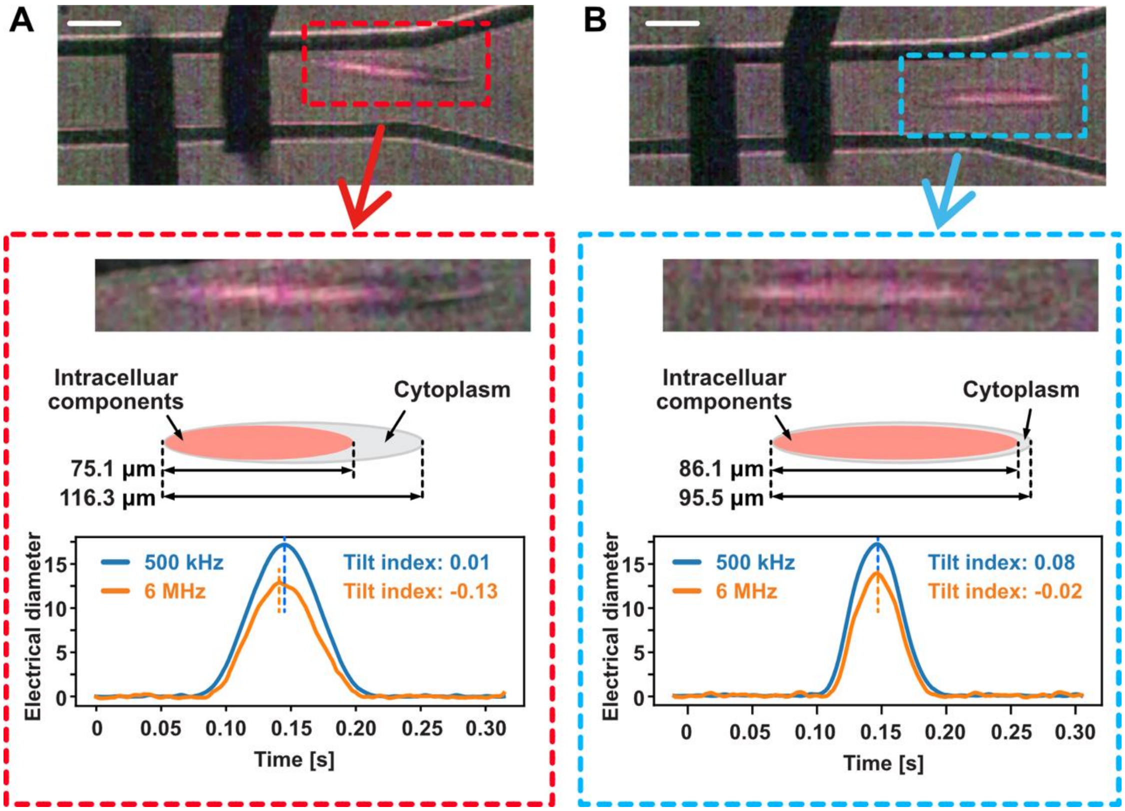

Fig. 3.9: Comparison of tilt index for two E. gracilis cells with different distributions of intracellular components. (A) E. gracilis cell with intracellular components constituting about 64.6% of cell interior on the left. (B) E. gracilis cell with almost evenly distributed intracellular components. Scale bar indicates 30 μm.

Fig. 3.9 illustrates the impedance waveforms of two cells. All waveforms were collected by the DAQ device (USB-6363) at a sampling rate of 125 kHz, which is sufficient to collect most details. In this case, impedance pulses have been transferred to the electrical diameter. The Electrical diameter of single cells at different detection frequencies is the magnitude of the impedance pulses. Obviously, different detection frequencies and target cells resulted in different electrical diameter. With the same the low detection frequencies (e.g., 500 kHz), the electrical diameter is related to the cell volume and changes according to the cell size. The high detection frequency (e.g., 6 MHz) can detect the cell interior, and its magnitude is related to the amount of intracellular composition. For example, the cell in Fig. 3.9A has less intracellular components than the cell in Fig. 3.9B. Accordingly, the first cell has a smaller high-frequency electrical diameter than the second one.

3.2.2.4. Summary

Overall, the dual-frequency impedance assays enabled rapid and quantitative tracking of the changes in biophysical properties of *E. gracilis* single cells under aerobic incubation conditions at a high throughput (~ 900 samples/s). Based on two metrics, namely the electrical diameter, opacity, cell volume and intracellular components are successfully detected.

The simplicity of the measurement suggests that my method is suitable for a new generation of rapid tests for intracellular components at a sub-cellular level. The ability of high frequency to cross the cell membrane and characterize intracellular composition provides considerable benefits to resolve largely unseen compositions and to investigate responses in cell populations in near real-time. The only limitation is that the dielectric properties of some organelles (e.g., chloroplasts) and biomolecules (e.g., paramylon) are so far unknown, which requires further analysis to distinguish their influence on impedance detection.

3.2.3. Intracellular density detection

3.2.3.1. Experiment purposes and preparation

Cell staining is a typical procedure for assessing the distribution and density of intracellular components. In this work, a label-free alternative is developed and verified using impedance cytometry to characterize the loss of intracellular components of *E. gracilis* cells. By inhibiting chloroplast synthesis, the number of chloroplasts in single cells are reduced gradually, as is the density of intracellular components. As a result, low-frequency impedance signals (0.5 MHz) are shown to assess the cell morphology. With increasing voltage frequency (i.e., > 1 MHz), the resistance of the cell membrane lowers. The magnitude and morphology of impedance signals (6 MHz) has a relationship with the density and distribution of intracellular components, respectively. Additionally, impedance-based cell phenotyping reveals that the shrinking of intracellular components and cell volume can cause two distinct declines in the high- and low-frequency electrical diameter of single cells, respectively. This conclusion is confirmed by simulation results and the time course of the changes in electrical diameters and electrical opacity. To sum up, my findings indicate that impedance cytometry and my analysis method can be further refined to serve as a powerful and non-invasive tool for assessing intracellular components at the single cell level.

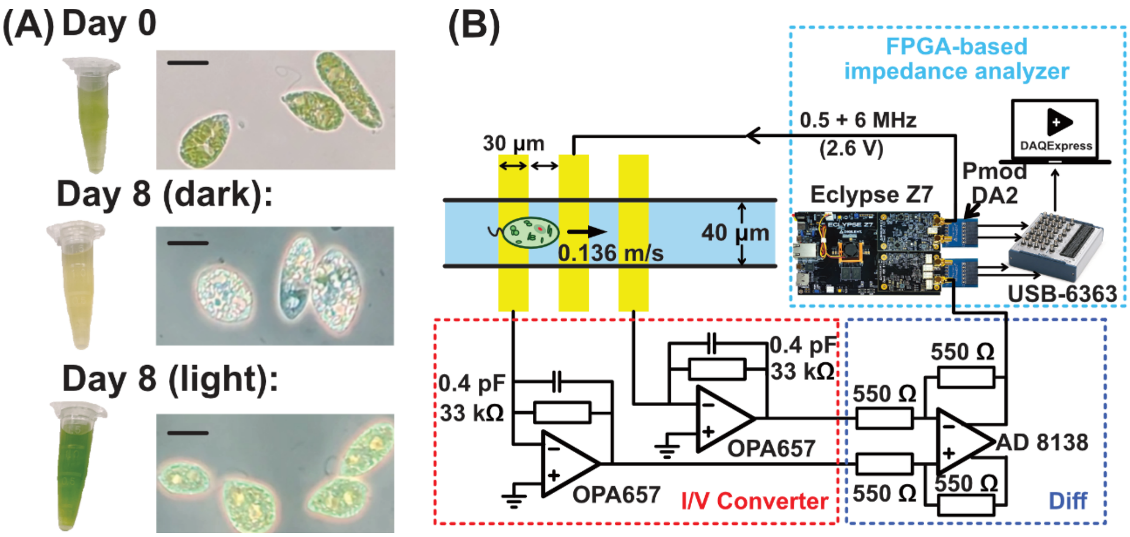

Fig. 3.10: Principles of detecting impedance signal changes of *E. gracilis* single cells with chloroplast discoloration. (A) Experimental images *E. gracilis* samples used for measurements in different states, including initial state, 8 days of dark and light culture. Scale bar represents 30 µm. (B) A photograph (top) ad a schematic (bottom) of the detection system, and individual particles are measured at two simultaneous frequencies (i.e., 500 kHz and 6 MHz) using a FPGA-based impedance analyzer.

During pre-cultivation, *E. gracilis* cells were cultivated in a culture tube using Koren-Hutner (KH) medium (pH 3.5) [102] for more than one week. Cell cultures were kept at 23.5 °C under continuous light illumination of 130−150 µmol/m^2/s photons. In experiments, *E. gracilis* cells in the precultures were transferred into new culture medium (KH) at a concentration of 440 cells/µL, and then divided into 6 tubes with 20 mL per tube. Half of test tubes were used as the control and were still incubated in the same light conditions as pre-cultivation, while the other three were incubated in the dark as dark group. As shown in Fig. 3.10A, there is a clear color difference between the dark and light group, which is due to the decrease in the number of chloroplasts in the dark.

Experiments were conducted at 5 different time points (i.e., 0 days, 2 days, 4 days, 6 days, and 8 days) for the light and dark groups, and each group contained three independent cell cultures of *E. gracilis* for robust characterization. Besides, 10 μm polystyrene beads (Polysciences, USA) were used as the references for the calibration of the electrical diameter and electrical opacity of single cells, because the physical property of beads is frequency-independent, which can be treated as perfect insulators. For impedance detection (see Fig. 3.10B), all samples were transferred to 1× phosphate-buffered saline (PBS) and injected by a syringe pump (Harvard Apparatus 11 Elite) to the detection area in which single cells/beads flowed at a rate of about 0.136 m/s. The throughput (sample rate) of the impedance detection is about 1500 cells/s, in this case.

10 μm polystyrene beads were used as the reference particles, owing to their fixed permittivity and conductivity. Also, they can be considered as perfect insulators independent of AC frequencies [79]. The influence of target object shape on impedance signals has been investigated in my previous studies [44]. The tilting impedance pulses can be quantified through the metric – tilting index ($T^{Left}/T^{right} - 1$), which is defined as the ratio of the left-half duration of the impedance pulse to the right-half duration. Additionally, the electrical opacity ($|Z_{HF}|/|Z_{LF}|$) is used to represent the changes in the density of intracellular components.

3.2.3.2. Simulation analysis

The simulation aims at analyzing propagation profiles of currents on the cell membrane at two detection frequencies, and a cell model with the same distribution of intracellular components and different morphology (see Fig. 3.11A) was employed in this work. Based on single-shell model [96], [97], *E. gracilis* (see Fig. 3.11A) is simplified as a 2D ellipse in simulation (Radius: 30 μm long-axis, 10 μm short-axis) for the case 1. The cell membrane (10 nm) was modeled using the contact impedance approximation [98], [99], [103]. All intracellular components, including paramylon and chloroplasts, were considered as non-conducting 2D circles (Dimensions: 1 μm radius, 0-2 μm span). This is because paramylon belongs to the water-insoluble crystals [104]–[107] and chloroplasts possess a double cell membrane envelope [103], therefore, both components should show high resistance at a detection frequency of 6 MHz.

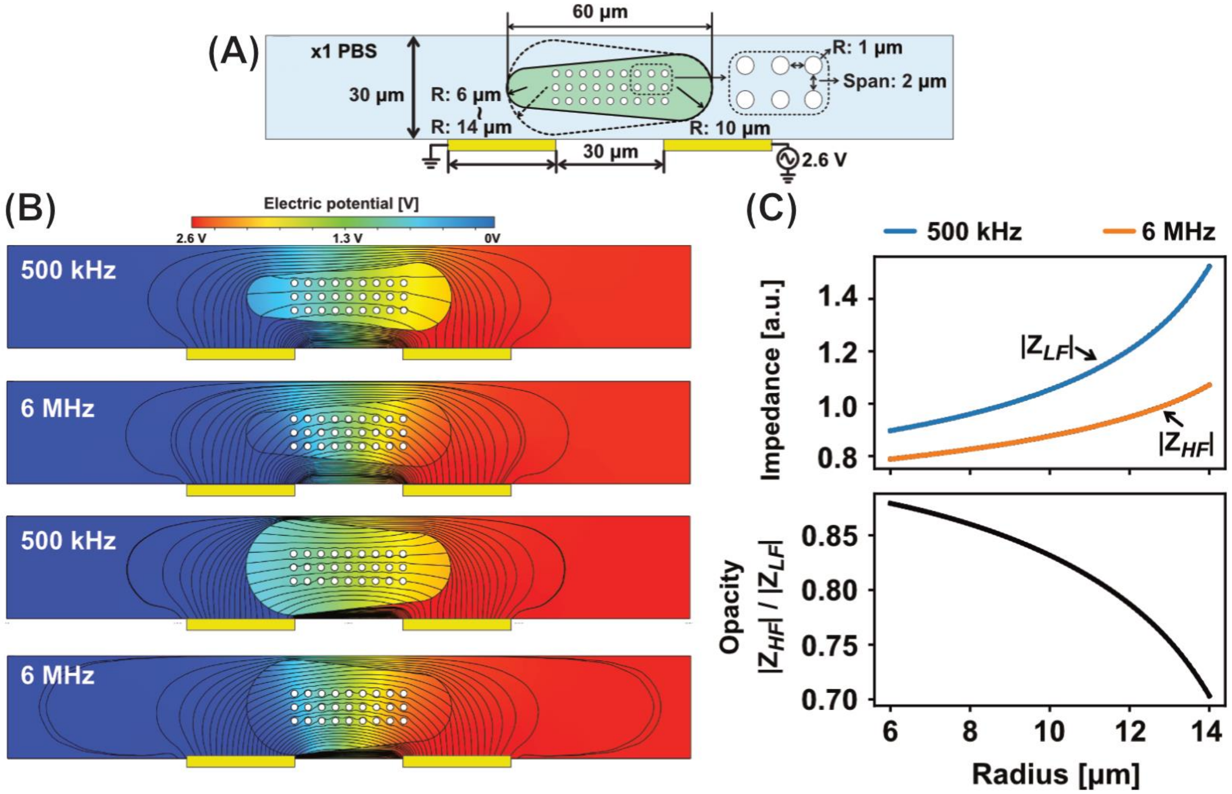

Fig. 3.11: Numerical simulation results for *E. gracilis* cell models with varying cell morphology distribution at low (500 kHz) and high (6 MHz) detection frequencies: (A) parameters used in simulation, (B) Electronic potential distribution for two types of cell models with high (top two) and low (bottom two) intracellular density. Black solid lines represent current lines. The density of the black streamlines indicates the current density (A/m^2). (C) Effects of the distribution of intracellular components on the dielectric properties of single cells, including the low-frequency ($|Z_{LF}|$) and high-frequency impedance ($|Z_{HF}|$), and opacity ($|Z_{HF}|/|Z_{LF}|$).

The propagation of current in a microchannel is illustrated in Fig. 3.11B, where the solid and smooth black lines denote the current signals. At a low frequency (500 kHz), current signals abruptly change direction as they cross the cell membrane. This phenomenon is known as the high resistance of the cell membrane, which can distort the propagation profile of low-frequency current. At a detection frequency between 1 and 5 MHz [73], the lipid bilayer of the cell membrane presents increasing resistance to the current as the detection frequency decreases. The impedance signals are primarily determined by the dielectric properties of the cell membrane rather than intracellular components. At a high-frequency electric field (e.g., 6 MHz), current can propagate within the cell, and all current profiles remain smooth regardless of the presence of cell membrane. Intracellular components can directly act on the high-frequency impedance signals by impeding the conduction of high-frequency current. If the voltage frequency is greater than 20 MHz, all organelles (e.g., chloroplasts) are conductive, resulting in a cytoplasm-dependent state of the impedance signal. In this work, the high detection frequency was set to 6 MHz because it can pass through single-shell cell membranes, but not through organelles with double membranes (i.e., chloroplasts) or biomolecules (i.e., paramylon).

In simulation, when a cell has the same morphology and different distribution of intracellular components, the impacts of cell morphology on the impedance signals are shown in Fig. 3.11C. A cell with increasing volume leads to an increase in impedance at low and high detection frequencies, but the impedance increases faster at low frequencies (500 kHz) than at high frequencies (6 MHz). Besides, the electrical opacity of the cell decreases with increasing volume, when the intracellular components remain the same. This phenomenon suggests that the volume changes have a more apparent effect on the low-frequency impedance signals than on the high-frequency ones, and that the electrical opacity decreases when the intracellular density decreases.

3.2.3.3. Experimental results and discussion

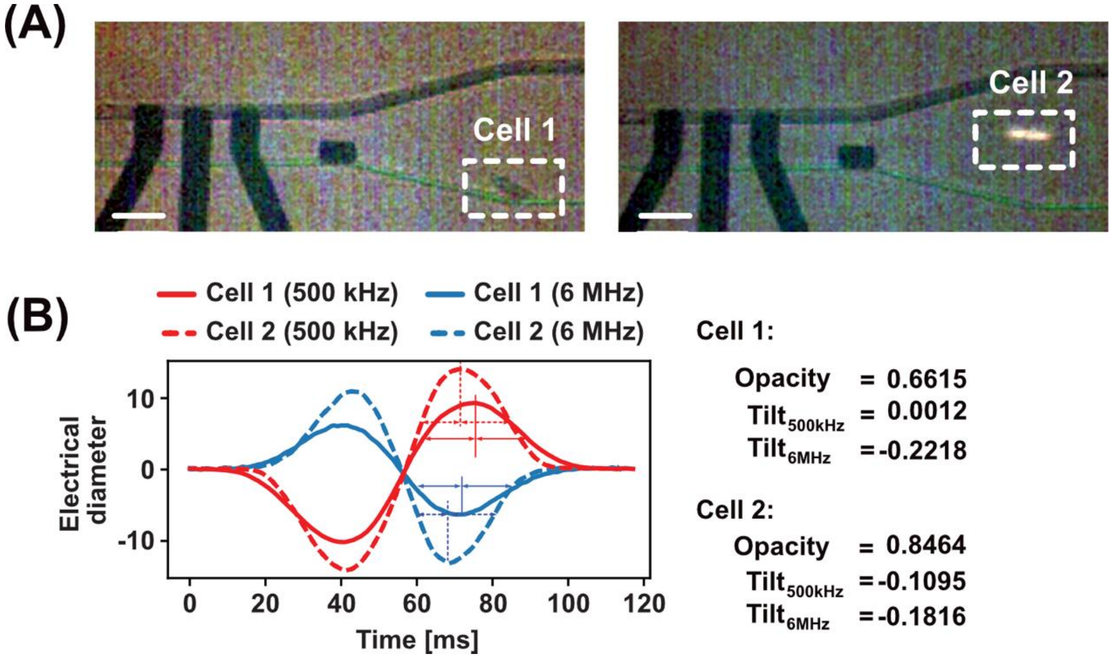

Fig. 3.12: Comparison of two *E. gracilis* cells with different intracellular densities. (A) Fluorescence images of both *E. gracilis* cells. Scale bar represents 60 µm. (B) Impedance signals of both *E. gracilis* cells.

In experiments, when *E. gracilis* cells flow through the detection area, the induced low-frequency impedance signals provide information about the cell volume and cell morphology. High-frequency impedance signals provide information about the intracellular density and distribution, and low-frequency impedance signals are related to cell volume and morphology. In Fig. 3.12A, the autofluorescence of chloroplasts in *E. gracilis* cells was used to visualize intracellular components (i.e., chloroplasts) and intracellular distribution. The intensity of the fluorescence increases as the number of chloroplasts increases. In comparison to the cell 1 (see Fig. 3.12B), the cell 2 had a higher fluorescence intensity and also exhibited a bigger electrical opacity (i.e., 0.8464). This result is attributed to the fact that the cell 2 contained more chloroplasts, contributing to a more compact distribution of intracellular components and also to an increase in cellular density. By contrast, cell 1 had no chloroplasts insides and also no fluorescence.

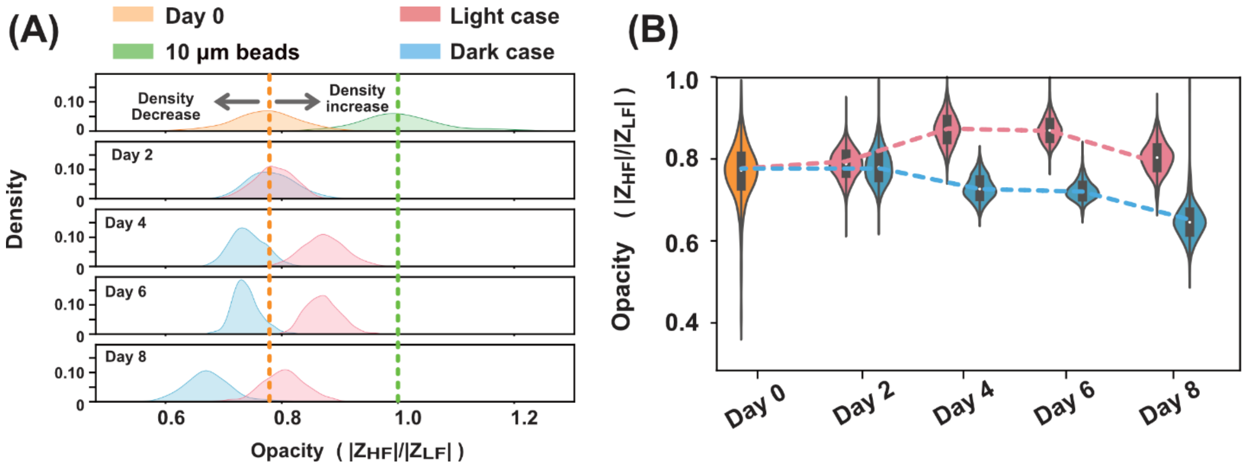

Fig. 3.13: (A) Time course of the changes in the opacity ($|Z_{HF}|/|Z_{LF}|$) of 10 µm polystyrene beads as well as *E. gracilis* cells (n=1000) cultivated under light and dark conditions within eight days. (B) Violin plots of the changes in opacity over 8 days for *E. gracilis* cells in two cases.

The electrical opacity represents the ratio of the impedance at low and high detection frequencies. When current propagates in fluid between electrodes, free ions in solution migrate toward the electrode. As these ions build up, an electrical double-layer (EDL) forms at the surface of the electrodes. The EDL results in a varying capacitance between fluid and electrode at different detection frequencies [108]. Typically, the influence EDL in the impedance cytometry is neglected when the detection frequency is greater than 100 kHz [93]. Therefore, at a low detection frequency (500 kHz), the low-frequency impedance can be related to the cell volume, shape. In contrast, at a high detection frequency (6 MHz), the high-frequency impedance is related to the volume and distribution of intracellular components. In this section, I employed electrical opacity to characterize intracellular densities so that to eliminate the influence of varying cell volume.

Fig. 3.13A shows the time course of opacity changes for 10 μm beads and *E. gracilis* cells cultivated in the dark and light conditions for eight days. In comparison to polystyrene beads with an opacity of 1, day-0 *E. gracilis* cells had an opacity of 0.78 (mean point). The opacity of the *E. gracilis* cells is less than one, which agrees with the conclusion in simulation. High-frequency current can propagate both within and outside the cell, resulting in a low impedance magnitude. By contrast, the cell membrane is extremely resistive to low-frequency current, and current can propagate only in flowing fluid, not within the cell. As a result, the magnitude of the low-frequency impedance is usually larger than that of the high-frequency impedance.

Additionally, the magnitude of the low-frequency impedance is proportional to the cell volume, because a large cell in a sealed channel results in a tiny conducting area, which leads to a high current resistance. The magnitude of high-frequency impedance is dependent on the distribution and density of intracellular components. As simulations demonstrate, the high-frequency impedance increases proportionally to the number and also the compactness of intracellular components. It is conceivable that the ratio of high- to low-frequency impedance reflects the density of intracellular components.

During the 8-day cultivation, the difference in opacity between both cases began on the second day and peaked on the fourth day. Compared with the day-0 samples, the opacity of cells in the light case is greater, whereas the opacity in the dark case is decreased, because the loss of chloroplast spares some intracellular space and decreases the intracellular density. Clearly in Fig. 3.13B, the opacity of *E. gracilis* cells continued to decline as chloroplasts were lost, despite that fact that they were still capable of synthesizing paramylon via external nutrients. However, in the absence of photosynthesis, *E. gracilis* cells in the dark can only utilize nutrients in culture medium to synthesize and store paramylon, a process that is less efficient than cells in the light. Especially, when the external nutrients are insufficient, *E. gracilis* cells have to consume stored carbon source (paramylon) inside single cell. As a result, the intracellular biomass gradually decreased after day 2.

3.2.3.4. Summary

Overall, all simulation and experimental results revealed that the impedance-based detection method is capable of performing intracellular analysis, including the density and dielectric properties of cells. Given the ease of the measurement, this technique in combination with my suggested analysis method can be utilized to develop a new generation of quick assays for intracellular components. The only limitation is that the dielectric properties of various organelles and biomolecules are unknown, necessitating additional study to differentiate them at different frequencies.

3.2.4. Single cell biomass tracking

3.2.4.1. Experiment purposes and preparation

The biomass assessment of single cells plays a vital role in many areas, including the analysis of cell state [109] and of cell growth mechanism [110], as well as environmental and energy issues [111], [112]. To date, several techniques, including live-cell imaging [22], Raman flow cytometry [113], and chemical probes [114], have been successfully applied for high-throughput assessment of intracellular biomass in single cells. However, most of these optical-based approaches are time-consuming and labor-intensive, and the tight requirement for maintaining and calibrating beam-focusing points limits their robustness and portability. In this work, I proposed a more effective and convenient method to characterize biomass as the magnitudes of high-frequency impedance signals.

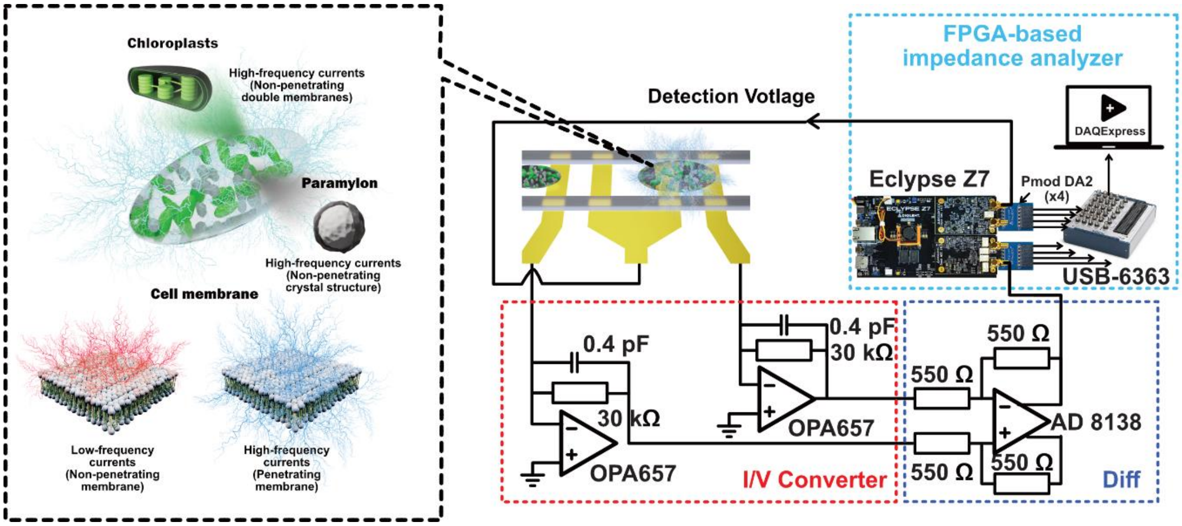

Fig. 3.14: Schematics of the four-frequency impedance cytometry. (A) Microfluidic impedance cytometry for the detection of *E. gracilis* cells, and some important structures of single *E. gracilis* cells. (B) Impedance signals at four distinct frequencies (i.e., 500 kHz, 4 MHz, 7 MHz, and 10 MHz), and the effect of intracellular component distribution on the morphology of high-frequency impedance signals. (c) FPGA-based impedance analyzer, and (d) the frequency response of the homemade transimpedance amplifier.

A four-frequency impedance cytometry (i.e., 500 kHz, 4 MHz, 7 MHz, and 10 MHz) was employed for analyzing the biomass of single *E. gracilis cells*, as shown in Fig. 3.14. In order to monitor the biomass of single cells, *E. gracilis* cells were cultured under various conditions over four days. The high-frequency impedance (7 MHz, and 10 MHz) was employed to detect intracellular biomass, and low-frequency impedance was used to track the changes in the cell volume. Electrical scanning *E. gracilis* cells internally and externally clearly showed the cellular response to different cultivation medium with organic source or inorganic ions, in which cells exhibited significant differences in multiplication, volume, and opacity. The volume of single cells was monitored via low-frequency impedance magnitudes, and the biomass change was tracked by high-frequency impedance magnitudes. The impedance detection system was built on a field-programmable gate array (FPGA) board with a home-made transimpedance amplifier (see Fig. 3.14) [85]. I envision that the tilt index can be an alternative to determine the frequency of electrical penetration for cell membrane. Besides, the proposed impedance-based platform can be adopted to evaluate cellular states and biomass, which is critical in practical applications involving continuous cell cultures [115], [116].

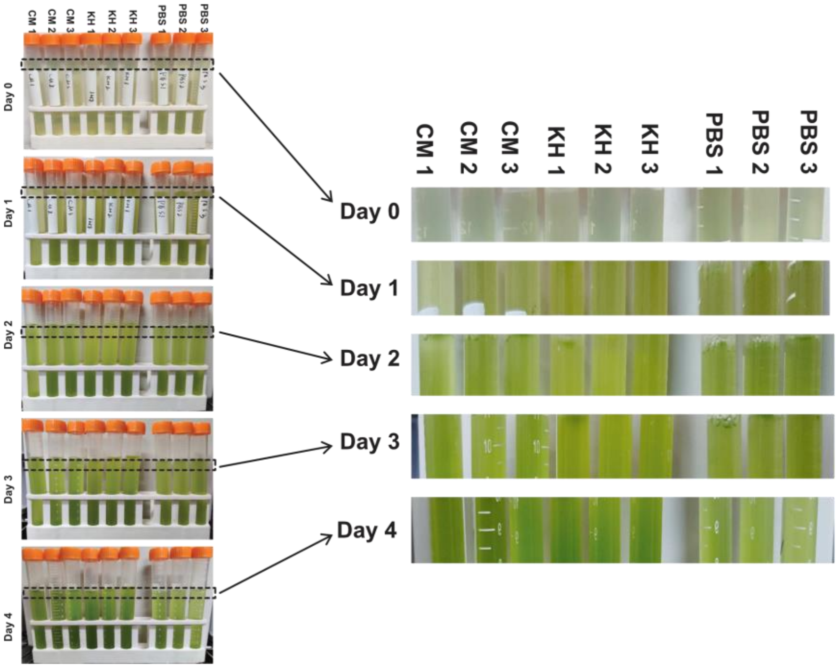

Fig. 3.15: Color change in culture tubes for *E. gracilis* cells. The green color becomes more intense as more cells multiply each day.

Before experiments, the cultures were grown in culture tubes each with a working volume of 13 mL under continuous illumination (warm white, 130−150 μmol/m^2/s) at 28 °C. To study the effect of organic nutrients on biomass and metabolization of individual cells, *E. gracilis* cells were grown photo-mixotrophically using KH medium (PH: 3.5) [117]. As for the effect of inorganic ions on cell growth, *E. gracilis* cells were cultivated photo-autotrophically using CM medium (PH: 3.9) [118]. *E. gracilis* cells were cultivated using 1× Phosphate-Buffered Saline solution (PBS, PH: 6.9) as the control group. The detailed components of CM and KH medium were described by Wang et al. [119]. Briefly, the CM medium does not include any organic carbon sources, whereas the KH medium contains glucose and various organic acids and amino acids as carbon sources [120]. Both KH and CM medium contain high concentrations of inorganic ions, such as Zn^{2+}, Mn^{2+}, Fe^{3+}, Cu^{2+}, Co^{2+}, and Ni^{2+}, some of which can promote the biomass accumulation and multiplication of *E. gracilis* cells [121], [122].

Experiments were conducted over a 4-day period (i.e., 0-4 days) for the CM-medium, KH-medium, and 1×PBS solution, with each group containing three independent cultures of *E. gracilis* for robust characterization. The growth of *E. gracilis* cells were analyzed through cell number, dry weight, cell volume, and opacity. Herein, the dry weight of *E. gracilis* cells is determined using 0.4 mL of cultures that had been dried at 100 °C for more than 4 hours [123]. The volume of the cells was determined using low-frequency electrical diameters ($|Z_{LF}|^{1/3}$) and the volume of intracellular components was determined using high-frequency electrical diameters ($|Z_{HF}|^{1/3}$) [124]. The color change in culture tubes over four days is shown in Fig. 3.15, and the green color in the culture tubes gets darker as the number of cells grows.

3.2.4.2. Experimental results and discussion

In this work, I employed low-frequency impedance metrics (i.e., 500 kHz, and 4 MHz) to track the volume change in *E. gracilis* cells during photo-mixotrophic cultivation, as well as high-frequency impedance metrics (i.e., 7 MHz, and 10 MHz) to monitor the biomass accumulation. I cultured *E. gracilis* cells in Koren-Hutner (KH) medium for four days and impedance signals were used to determine the biomass accumulation of *E. gracilis* cells grown photo-mixotrophically. The impedance detection of *E. gracilis* cells are shown in Fig. 3.16. In this section, a maximum detection frequency of 10 MHz was used, which worked well with my system and is also commonly used for cell interior analysis [45]. The lowest detection frequency (500 kHz) has been tested in my previous work to characterize the volume and shape of single cells [124], [125]. The two middle frequencies, 4MHz and 7MHz, were selected based on a 3MHz spacing.

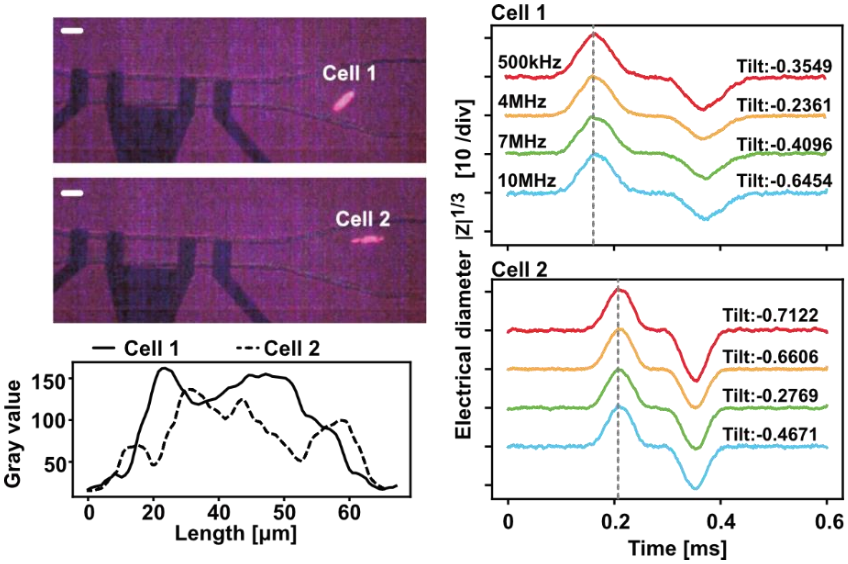

Fig. 3.16: Impedance detection of *E. gracilis* cells. Electrical diameter and tilt index of two *E. gracilis* cells with different brightness at four detection frequencies (i.e., 500 kHz, 4 MHz, 7 MHz and 10 MHz). The scale bar indicates 30 μm.

E. gracilis cells can proliferate rapidly and accumulate paramylon in photo-mixotrophic cultivation by either photosynthesis or digesting organic carbon sources in the cultivation medium (KH medium). *E. gracilis* cells cultivated in KH medium over four days are illustrated in Fig. 3.17A. In Fig. 3.17B, the number of *E. gracilis* cells continued to increase over four-day cultivation, from around 241 cells/μL to 1936 cells/μL. Also, the biomass of *E. gracilis* cells increased rapidly from 2.4 mg/mL to 8.5 mg/mL. The sudden drop at Day 3 may be due to the measurement error.

As for the impedance characterization of single cells, in Fig. 3.17C, all dielectric properties of *E. gracilis* cells were calibrated using the dielectric properties of 10 μm beads. Over a four-day cultivation period, the electrical diameter of cells at 500 kHz increased from around 10.89 to 11.46. This is because low-frequency impedance value depends on the cell volume: a rise in low-frequency electrical diameters indicates an increase in cell volume [24], [45], [124]–[126]. At the highest detection frequency (10 MHz), current can freely penetrate the cell membrane and propagate in the cytoplasm between intracellular components (i.e., paramylon and chloroplasts), allowing the high-frequency electrical diameter to be related to the intracellular nonconductive biomass of individual cells. Therefore, the increase in both low- and high-frequency diameter can denote that there was a slight increase in the volume and biomass during the first 2 days.

In Fig. 3.17D, the electrical opacity of the cells (day 1-4) is nearly identical to that of the precultures (day 0), since the new cultivation conditions are the same as the preculture condition. Whereas the rise in high-frequency electrical diameter (i.e., 7 MHz to 10 MHz) happened on the first day, earlier than the increase in low-frequency (i.e., 500 kHz) electrical diameter that occurred on the second day (see Fig. 3.17C). This may be because when *E. gracilis* cells were transferred to a fresh medium, adequate organic nutrients and inorganic ions induce the generation of intracellular components prior to cell multiplication. In detail, the proliferation rate of *E. gracilis* cell can be accelerated by the following ions: Mg^{2+}, Ca^{2+}, Mn^{2+}, Cu^{2+}, Co^{2+}, and

Ni^{2+} in the medium [127], and cell multiplication occurs slightly later than the chloroplast multiplication. For *E. gracilis* cells, the number of chloroplasts in each cell is relatively stable, varying from 10 to 20 [128]. When there are 60 or more chloroplasts per cell, it usually means that cell multiplication is taking place [129], [130]. Thus, *E. gracilis* cells may have increasing intracellular biomass prior to their multiplication, which results in a slightly earlier increase in high-frequency electrical diameters than low-frequency electrical diameters.

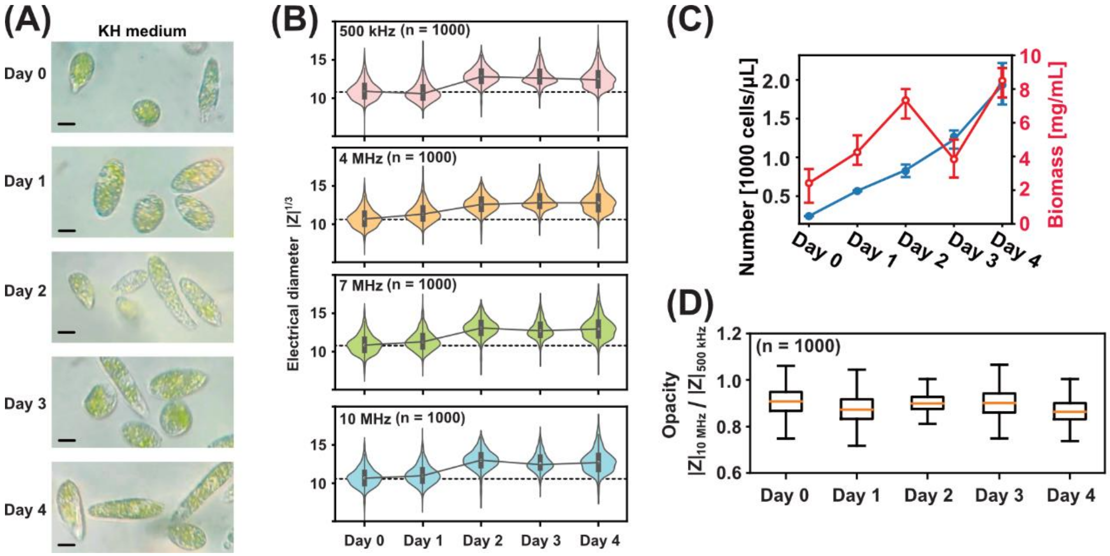

Fig. 3.17: Cell cultivation in KH medium over four days. (A) Comparison of volume of *E. gracilis* cells within four-day experiments. The scale bar indicates 10 µm. (B) Statistical analysis of the cell proliferation and biomass accumulation of *E. gracilis* cells. (C) Time course of changes in electrical diameters of *E. gracilis* cells at four detection frequencies (500 kHz, 4 MHz, 7 MHz and 10 MHz). (D) Time course of changes in electrical opacity of *E. gracilis* cells.

Although some inorganic metal ions are required for *E. gracilis* cell growth and are stabilized during biomass synthesis [127], [131], organic supplies may be insufficient in natural environment. Thus, *E. gracilis* cells have to grow photo-autotrophically, and most of the biomass have to be produced by photosynthesis using carbon dioxide from the air as the carbon source [132], [133]. To analyze the effect of inorganic ions on cell growth and biomass accumulation, *E.*

gracilis cells were cultured in a 1× PBS solution as a control. The dielectric properties, cell multiplication, and biomass accumulation of *E. gracilis* cells cultured in PBS and Cramer-Myers (CM) medium are compared and shown in Fig. 3.18.

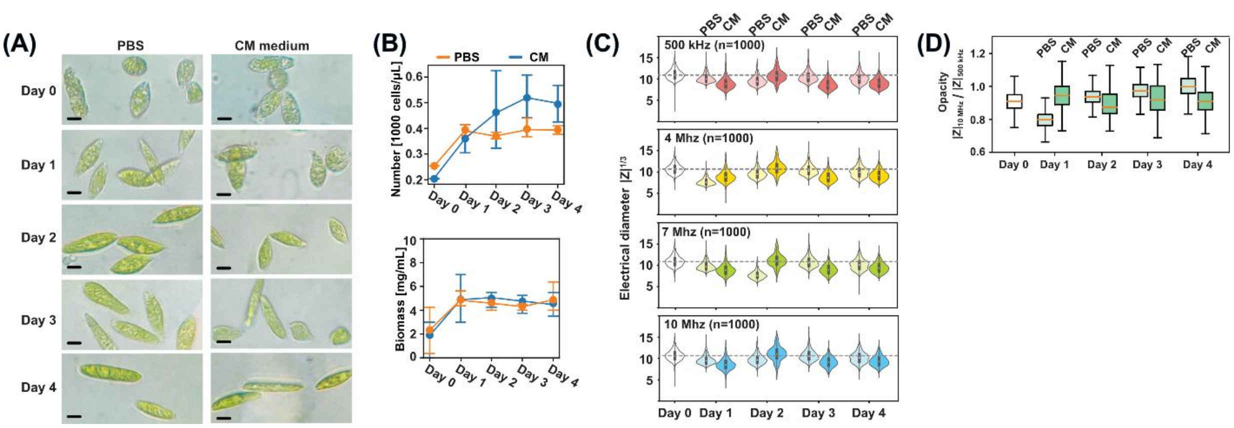

Fig. 3.18: Cell cultivation in PBS solution and CM medium over four days. (A) Comparison of volume of *E. gracilis* cells within four-day experiments. The scale bar indicates 10 µm. (B) Statistical analysis of the cell proliferation and biomass accumulation of *E. gracilis* cells. (C) Time course of changes in electrical diameters of *E. gracilis* cells at four detection frequencies (500 kHz, 4 MHz, 7 MHz and 10 MHz). (D) Time course of changes in electrical opacity of *E. gracilis* cells.

Without organic carbon sources in the growth medium, *E. gracilis* cells cultivated in PBS and CM medium over four days are shown in Fig. 3.18A. Because of the limited carbon sources in the air, the paramylon synthesis was restricted. Thus, when *E. gracilis* cells were transferred into CM medium and PBS solution, cells started to consume stored energy (paramylon), leading to the reduction in biomass. Additionally, the effect of inorganic ions on the cell growth is shown in Fig. 3.18B. Despite insufficient carbon sources, *E. gracilis* cells in CM medium divided more frequently than those in PBS solution. This result also satisfied several research on the conclusion of the promotion inorganic ions on the *E. gracilis* cell multiplication [107], [119], [134].

Although there were more cells in CM medium than in PBS medium, the biomass of the cells was almost the same in both cases. In other words, individual cells cultured in CM medium might own less biomass than cells cultured in PBS solution. This conclusion was further approved by impedance detection, as illustrated in Fig. 3.18C. After four days of cultivation, the electrical diameters of *E. gracilis* cells in PBS solution are larger than those of cells in CM medium at four detection frequencies. This indicated that *E. gracilis* cells in PBS solution had a larger volume, due to larger low-frequency electrical diameter, and have denser intracellular components, due to higher electrical opacity (see Fig. 3.18D), than cells cultured in CM medium.

Additionally, the electrical diameters and electrical opacity of cells are also good indicators of the change in cultivation medium. When *E. gracilis* cells were transferred to fresh cultivation medium, the electrical diameter and opacity of cells, especially in PBS solution, declined rapidly on the first day of cultivation, which can be related to changes in osmosis and pH value of the cultivation medium. After two days of adaptation to the new environments, *E. gracilis* cells returned to normal electrical opacity and diameter.

Considering the growth condition of *E. gracilis* cells in CM medium, KH medium and PBS solution, I concluded that some inorganic ions may contribute to cell multiplication. Especially when *E. gracilis* cells grow in an environment with sufficient organic and inorganic sources, the proliferation rate and cell biomass productivity reach the maximum. Inorganic ions can be accumulated in cells [121], [135], and the resultant biomass is valuable as a source of biodiesel.

3.2.4.3. Summary

Overall, all experimental results indicate that I successfully employed low-frequency impedance to performance analysis of the morphology and volume of single cells, and high-frequency impedance to characterize intracellular biomass. The detection mechanism is supported by numerous previous works. Our previous work has shown that low-frequency detection is capable of analyzing cell morphology, as the low-frequency current mainly propagates around the cell [44], [124], [125]. The dependence of low-frequency impedance on cell volume has also been verified [45]. Additionally, it has been demonstrated that high frequency impedance can be used to analyze the amount [125], distribution [124], and density [125], [136] of intracellular components. Here, impedance-based biomass analysis is based on the ability of high-frequency impedance to monitor the amount and density of intracellular components, which has also been proved by experimental results.

Besides, the proposed impedance-based platform has shown its capability to evaluate the effects of the culture conditions on *E. gracilis* cell growth (volume, opacity, and number) and biomass accumulation. High-frequency impedance magnitudes (≥ 7 MHz) can characterize biomass accumulation, and low-frequency impedance magnitudes (≤ 4 MHz) enable the quantification of volume of single cells. The changes in biomass accumulation and cultivated in different medium were successfully monitored over four days. In the future, I suggest extending the application of tilt index to mammalian cells to track changes of membrane properties in cell aging, carcinogenesis, or lysis.

3.3. Nanoscale detection of single bacteria

3.3.1. Parallel nano detection without post-calibration

3.3.1.1. Experiment purposes and preparation

Unlike visual measurements, impedance detection requires post calibration to quantify the morphology of single objects. This study presents a novel impedance cytometry system, called parallel impedance cytometry, for real-time calibration of the impedance signals. Parallel dual microchannels allow simultaneous detection of reference and target particles in two separate microchannels, without the pre-mixing of reference and target suspension. The performance of the system is evaluated by simulation and experiments, indicating that impedance pulses of the particles from parallel dual channels appear on the opposite sides of the same time series. The raw impedance waveforms can be directly used to assess the electrical properties of single objects without the need for long-term statistical analysis afterwards. Polystyrene beads with different sizes ranging from nano to microscale (e.g., 500, 750 nm, 1, 2, 3 and 4.5 μm) confirm the nano-sensitivity of the system. In addition, the detection of antibiotic-treated *Escherichia coli* (E. coli) demonstrates that my system can be used for quantitative assessment of the morphology change of individual cells, as well as for the proportion of sensitive cells in real time. The findings indicate that the novel impedance cytometry provides a new pathway for accurate, real-time analysis of single objects ranging from submicron to micron-scale.

To test the performance of the proposed system, six types of polystyrene beads (Polysciences, USA) size were employed, including 500 nm, 750 nm, 1 μm, 2 μm, 3 μm, and 4.5 μm. The physical properties of the beads are frequency-independent, and they are treated as perfect insulators and used as the reference for the impedance detection [73], [95].

In order to test the sensitivity of the developed system for detecting nanoscale objects, the E. coli cells were employed here. The nanoscale morphology change of E. coli cells can be a result of antibiotic treatment. In experiments, *E. coli* cells were maintained at 37 ºC and passaged every 12 to 16 hours. *E. coli* cells were treated with Mecillinam [137], [138] at a concentration of 1 μg/mL for 8 hours to induce spherical shape [139]. Then, the cell fixing was performed with 70% alcohol at 23 ºC. We manually stirred the cell-alcohol mixtures before putting them in the triple shaker at 100 rpm for about 2 hours to prevent the formation of aggregates. After the fixation, cells were then centrifuged at 3000 rpm for 30 minutes and washed in 1× PBS. The sample preparation followed the method used in previous experiments, which has been validated as applicable [145]. All fixed cells were suspended in the 1× PBS solution and stored at 4 ºC in a refrigerator. Sample suspension was loaded into the microchannel using a syringe pump to the detection area in the microchannel at a flow rate of 1 μL/min.

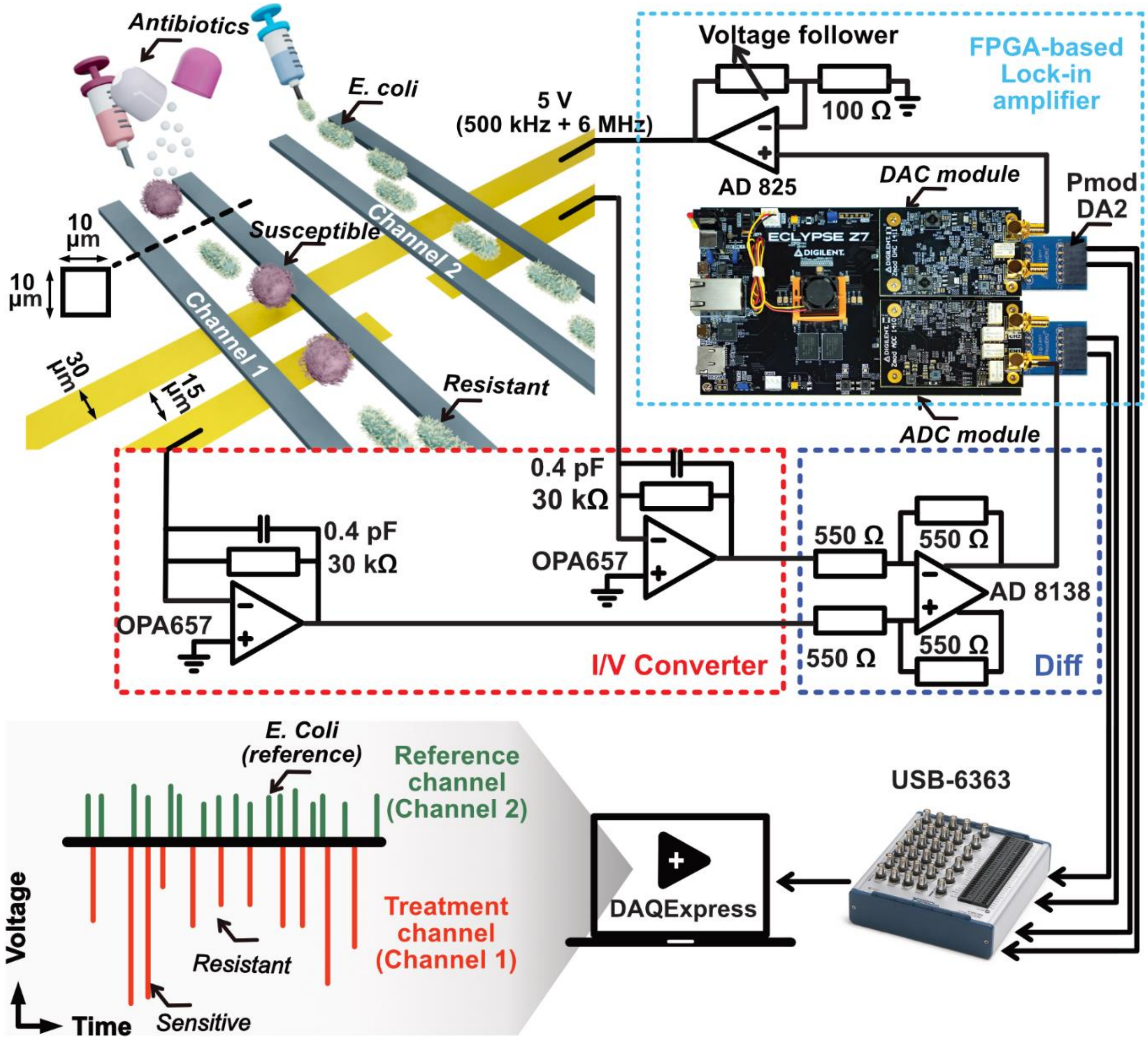

Fig. 3.19: Schematic of the FPGA-based detection system and the design of parallel impedance cytometry.

Fig. 3.19 illustrates the electrode layout and the FPGA-based impedance detection system. The microchannels are 10 μm wide and 10 μm deep, which are placed over 30 μm wide electrodes with spacing of 20 μm. The electrode has a 70 nm thick gold layer (Au) over a 70 nm thick chromium layer (Cr).

3.3.1.2. Simulation analysis

To study the working mechanism and sensitivity of the proposed parallel impedance cytometry system, I performed 3D numerical simulation via COMSOL Multiphysics 5.6 (COMSOL Inc., Burlington, MA, USA). The simulated microchannel has a dimension of 10 µm × 10 µm × 100 µm (Depth × Width × Length), and the electrodes are of 30 µm width and 20 µm span. The fluids in microchannel are set as 1× PBS. The relative permittivity and conductivity of 1× PBS in the microchannel are 80 and 1.34 S/m, respectively. Parallel channels have the same electrodes for applying detection voltages, but each has an independent detection electrode. The current output from each channel is labeled with distinct colors (channel 1 in blue, and channel 2 in orange, in Fig. 3.20). Same to my detection system, the final result is a differential calculation between channel 1 and channel 2, namely system output = channel 1 - channel 2 (labeled in red).

Spherical particles with different diameters of 500 nm, 750 nm, 1 µm, 2 µm, 3 µm, and 4.5 µm are set as nonconductive objects and flow through the channel 1 and channel 2, separately. In the detection region, the impedance rises as the particles squeeze out the conductive liquid above the gap between electrodes. This results in the decrease in current on the detection electrode as particles pass through the gap between the electrodes. The magnitudes of the impedance ($|Z|$) is positively related to the size of single particles. Particles have diameters ranging from 500 nm to 4.5 µm and the impedances range from 0.018 nA to 0.63 nA. Therefore, it is possible to realize the nanoscale sensitivity in simulation, and also assess the size of single objects with the impedance magnitude. In experiments, all current signals are converted to voltage signals for real-time processing on the FPGA board and data collection.

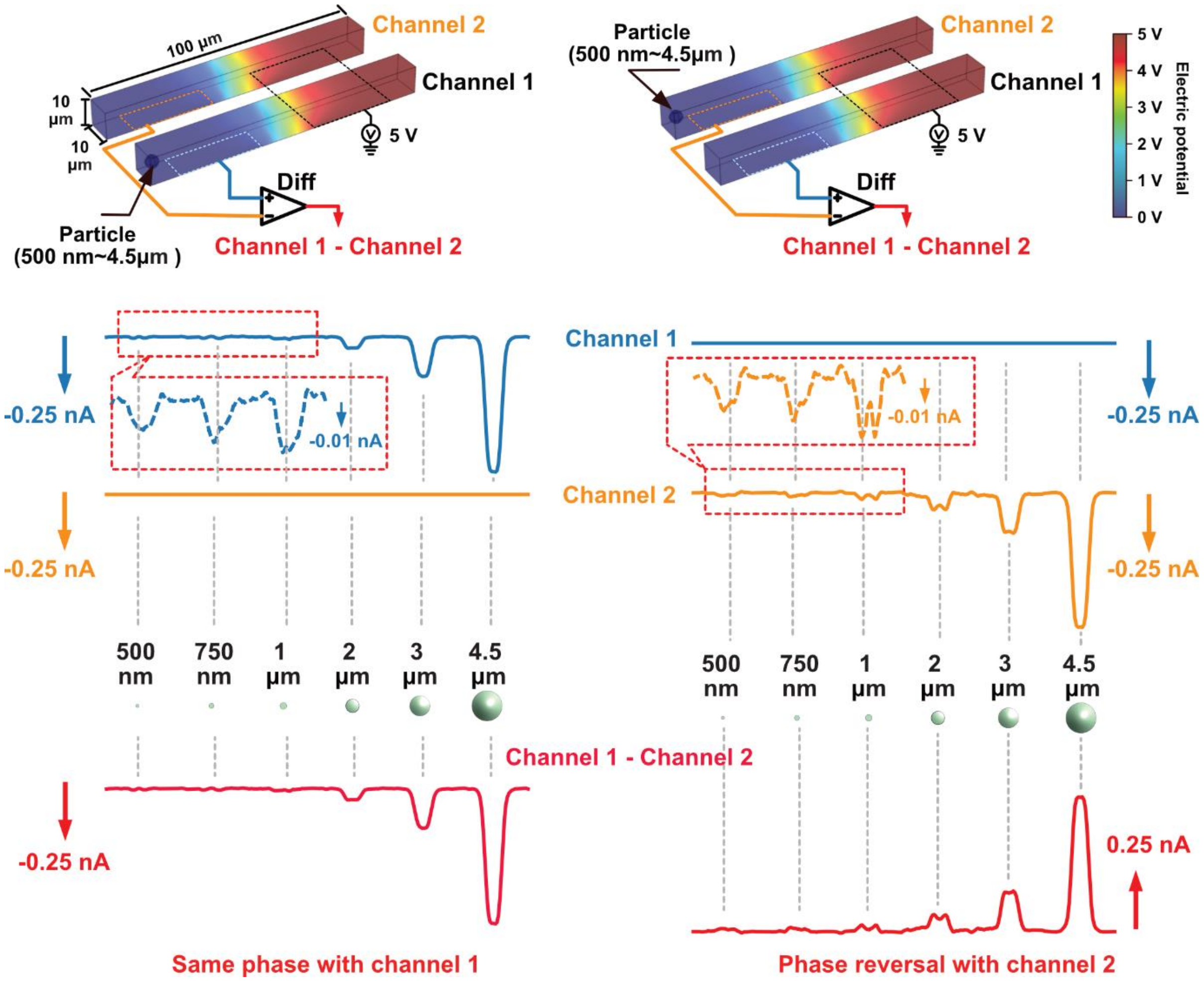

Fig. 3.20: Numerical simulation results of parallel impedance cytometry when particles of different sizes (500 nm – 4.5 μm) flow through channels. The current outputs from two channels are labeled with distinct colors (channel 1 in blue, and channel 2 in orange), and total system output is labelled in red.

A particle flowing in channel 1 produces an impedance pulse only at the output in channel 1, and a pulse generated at the output in channel 2 should be induced by a particle in channel 2. Besides, the raw impedance pulses generated in channel 1 and channel 2 are in the same phase. I took advantage of the differential amplifier to reverse the phase of impedance pulses in channel 2, and to merge the output of two channels. As a result, the system output is in the same phase with the impedance pulses in channel 1, which is in the opposite phase to the impedance pulse of channel 2. In both simulation and experiments, the parallel dual channels are powered by the same electric source (the FPGA board), so it is possible to merge the impedance signals from different channels and to process all the signals together. The same process, however, cannot be performed with two channels powered by different electric sources.

3.3.1.3. Beads experimental results and discussion (nanoscales)

Fig. 3.21 shows the raw impedance signals from the detection system, when the 4.5 μm polystyrene beads are used as reference particles in channel 1, and 6 types of beads with diameters of 4.5 μm (Fig. 3.21A and Fig. 3.21B), 3 μm (Fig. 3.21C), 2 μm (Fig. 3.21D), 1 μm (Fig. 3.21E), 750 nm (Fig. 3.21F), and 500 nm (Fig. 3.21G) are used in channel 2. As shown in Figure 4A, when 4.5 μm beads flowing in both two parallel channels, impedance pulses in channel 1 is in the revise direction to impedance pulses in channel 2. The impedance pulses in channel 1 appear on the downside of the time series, while the impedance pulses in channel 2 appear on the upside. This is consistent with the numerical simulation results. Additionally, as the beads in both channels have the same diameter (4.5 μm beads), the impedance pulses on either upside or downside of the same time series have the same magnitudes. When the diameter of the particles in channel 2 is unknown, it is possible to estimate the bead diameter to be around 4.5 μm through comparing the raw impedance waveforms of both channels during real-time detection (see Fig. 3.21A).

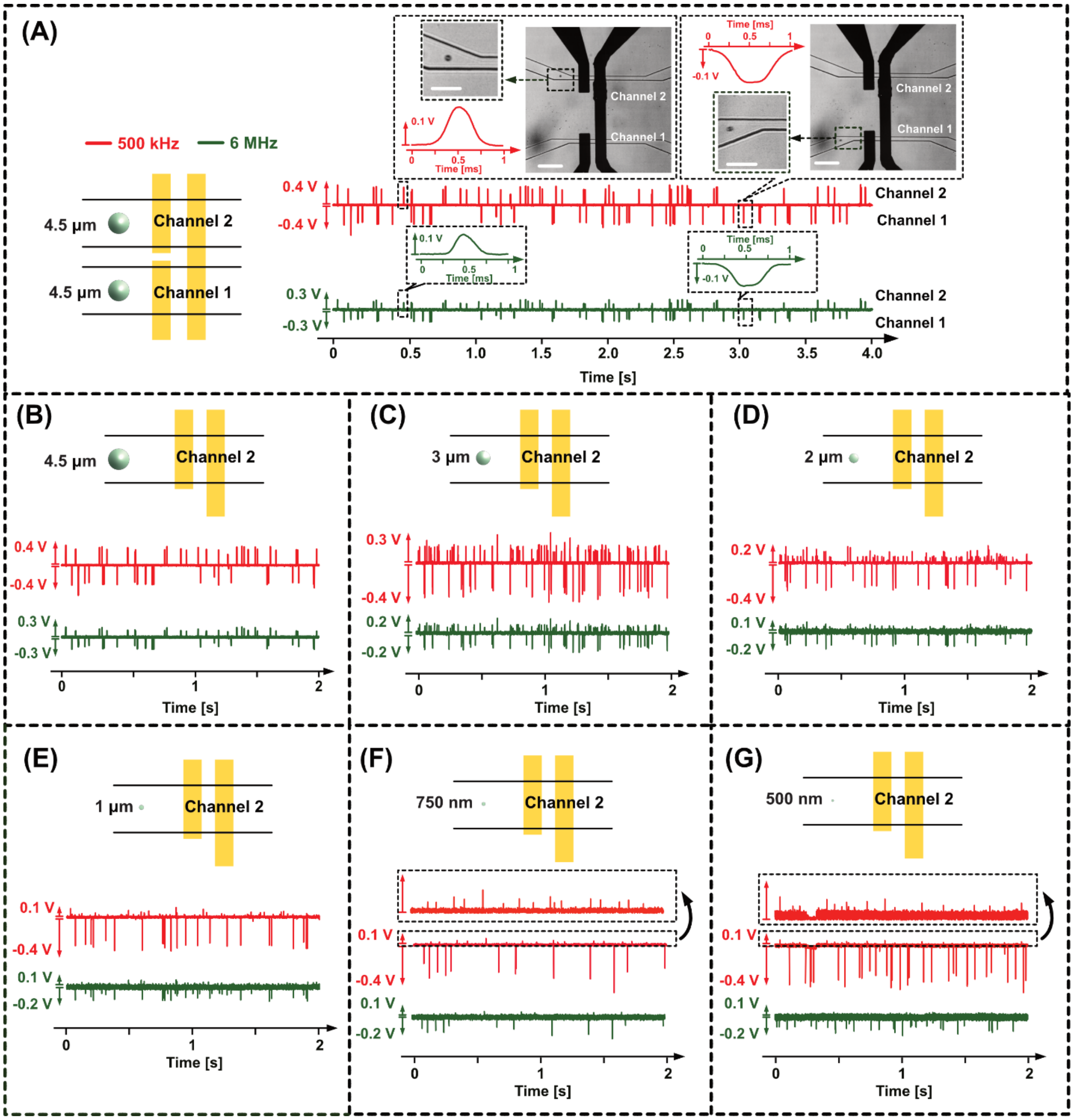

Fig. 3.21: Raw signal analysis of the parallel impedance cytometry. (A) In the first case, 4.5 µm beads flow in both channels, and the detection time for each bead is 1 ms. The scale bar denotes 30 µm. (B-G) For the other case, 4.5 µm beads flow through channel 1 that is used as a refence channel and beads of different diameters, (B) 4.5 µm, (C) 3 µm, (D) 2 µm, (E) 1 µm, (F) 750 nm and (G) 500 nm flow thorough channel 2 that is used as a measurement channel.

To show the impact of circuit on the impedance detection, the impedance signals in both channels at low (500 kHz, marked in red) and high detection frequencies (6 MHz, marked in green) were compared. Theoretically, polystyrene beads, which exhibit frequency-independent dielectric properties, can induce impedance pulses of similar magnitudes regardless of detection frequency when the detection frequency is less than 355 MHz [71]. In practical, the high-frequency impedance signal has a much smaller amplitude compared to the low-frequency impedance signal, as a result of circuit losses. Circuit loss varies with the detection system. As the particle trajectory and the detection circuit work together for impedance detection, the impedance pulses of the same particle may have different magnitudes. Thus, the variation in impedance magnitudes make it difficult to determine the particle volume based on raw impedance signals, although it is well known that the impedance magnitudes positively depend on particle volume [140], [141]. In this work, I can eliminate the impact of particle trajectory on the impedance detection, as the 10 μm × 10 μm microchannel can limit the trajectory fluctuation of single objects. It is evidenced by the stability of the impedance magnitudes for single beads. Despite there is a difference in the magnitude of raw impedance signal at different detection frequencies, one still could estimate the size of target particles in channel 2. This is because the magnitudes of upside and downside impedance pulses are the same, although at different detection frequencies.

To determine the sensitivity of the detection system, I compared the signals of particles with different sizes in channel 2, while keeping 4.5 μm beads flowing in channel 1 as a reference (see Fig. 3.21B-Fig. 3.21G). At both detection frequencies, the magnitudes of the upside impedance pulses generated in channel 2 decrease when the beads size reduces from 4.5 μm (Fig. 3.21B) to 500 nm (Fig. 3.21G). For example, in Fig. 3.21D, the upside impedance pulses (2 μm beads in channel 2) are about half the amplitude of the downside impedance pulses (4.5 μm in channel 1). Without any post-processing for calibration, one can easily determine the particles size of larger than 1 μm (see Fig. 3.21E) based on raw impedance signals. Real-time sizing of nanoscale particles with different diameters of 750 nm (Fig. 3.21F) and 500 nm (Fig. 3.21G) is also achieved.

All raw impedance signals can be post-processed for more accurate analysis. In order to calibrate the impedance pulse and obtain the electrical diameter ($|Z|^{1/3}$), all impedance signals in channel 2 are scaled according to the impedance pulse generated by 4.5 µm polystyrene beads in channel 1 (reference channel). The electrical diameter is defined as $D = G|Z|^{1/3}$, where $|Z|$ denotes the raw impedance magnitudes, and G is a gain factor accounting for the electronic circuitry. The gain factor [73], [95], [125] is determined by scaling the mean impedance of reference particles in channel 1, for example, meeting $G \cdot |Z|_{4.5\ \mu m}^{1/3} = 4.5$.

Fig. 3.22 shows the electrical diameter ($|Z|^{1/3}$) and phases ($|\emptyset(Z)|$) of polystyrene beads flowing in parallel channels at 500 kHz. The electrical diameter increases with increasing the diameter of polystyrene beads in channel 1. Moreover, the detection system can successfully identify the electrical diameter of beads with diameters less than 1 µm (e.g., 500 and 750 nm), demonstrating the nanoscale sensitivity. However, the location fluctuations of nanobeads in microchannels lead to larger distribution of their electrical diameters and phases, than microbeads with larger diameters (> 1 µm). The compact distribution of the electrical diameters of microbeads shows that the system with a 10×10 µm channel can stably monitor particles with a diameter greater than 1 µm. Additionally, both parallel channels share the same structure and electrode layout, resulting in only a slight difference in signals when 4.5 µm beads flow in both channels.

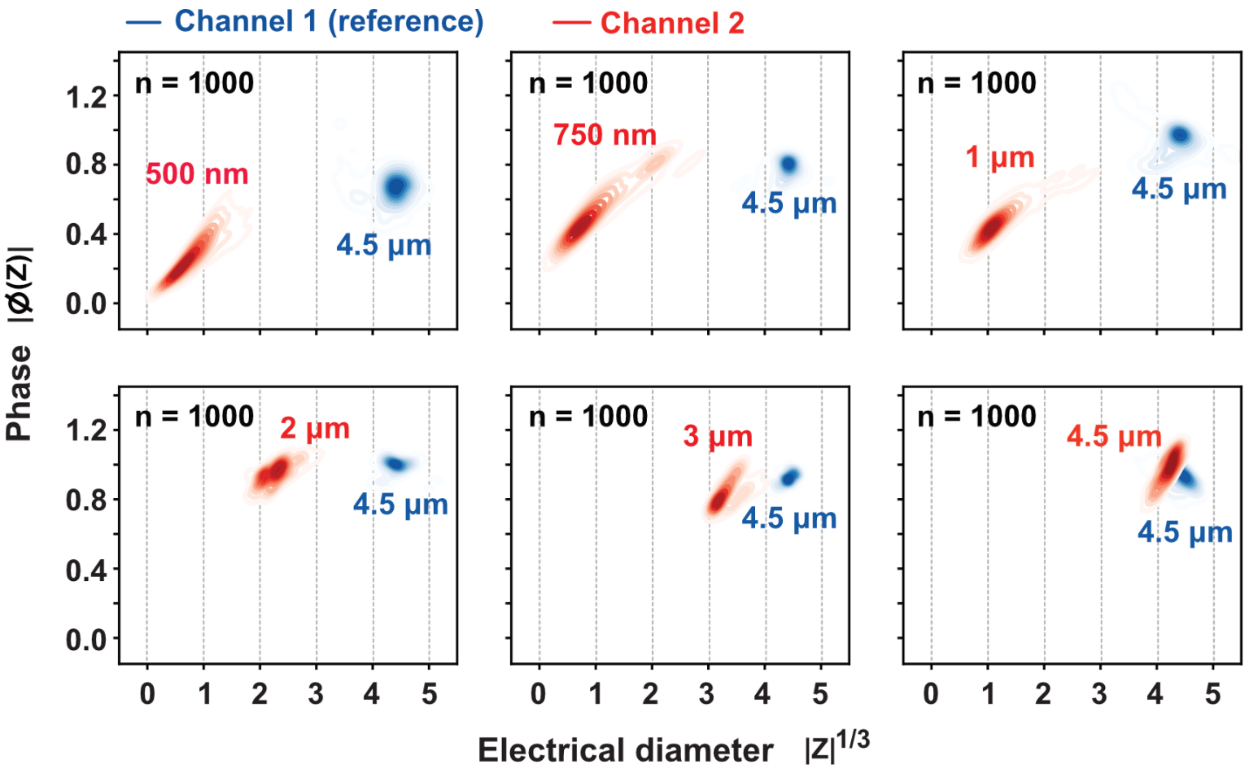

Fig. 3.22: Distribution analysis of electrical diameter ($|Z|^{1/3}$) vs phase ($|\emptyset(Z)|$) for parallel impedance cytometry at 500 kHz, when reference beads (4.5 µm) are in channel 1, and target beads (500 nm – 4.5 µm) are in channel 2.

3.3.1.4. Bacterial experimental results and discussion (Bacteria detection)

E. coli cell is a gram-negative, rod-shaped bacterium, which is frequently used as a model for antibiotic susceptibility testing. Susceptible *E. coli* cells suffered from the inhibition of cell division and morphological alterations under the treatment with 1 µg/ml of Mecillinam (see Fig. 3.23A). *E. coli* cells are susceptible to this antibiotic because beta-lactam antibiotics can inhibit penicillin-binding proteins (PBPs) anchored in the cytoplasmic membrane [142], [143]. For example, blocking of PBP-1 leads to rapid bacteria lysis [144], and blocking of PBP-2 or PBP-3 results in the spheroid shape of *E. coli* [145], as well as the inability to septate after doubling of cell volume during cell multiplication [146]. By contrast, *E. coli* cells that are resistant to an antibiotic can remain rod-shaped and divide in the presence of the drug [147].

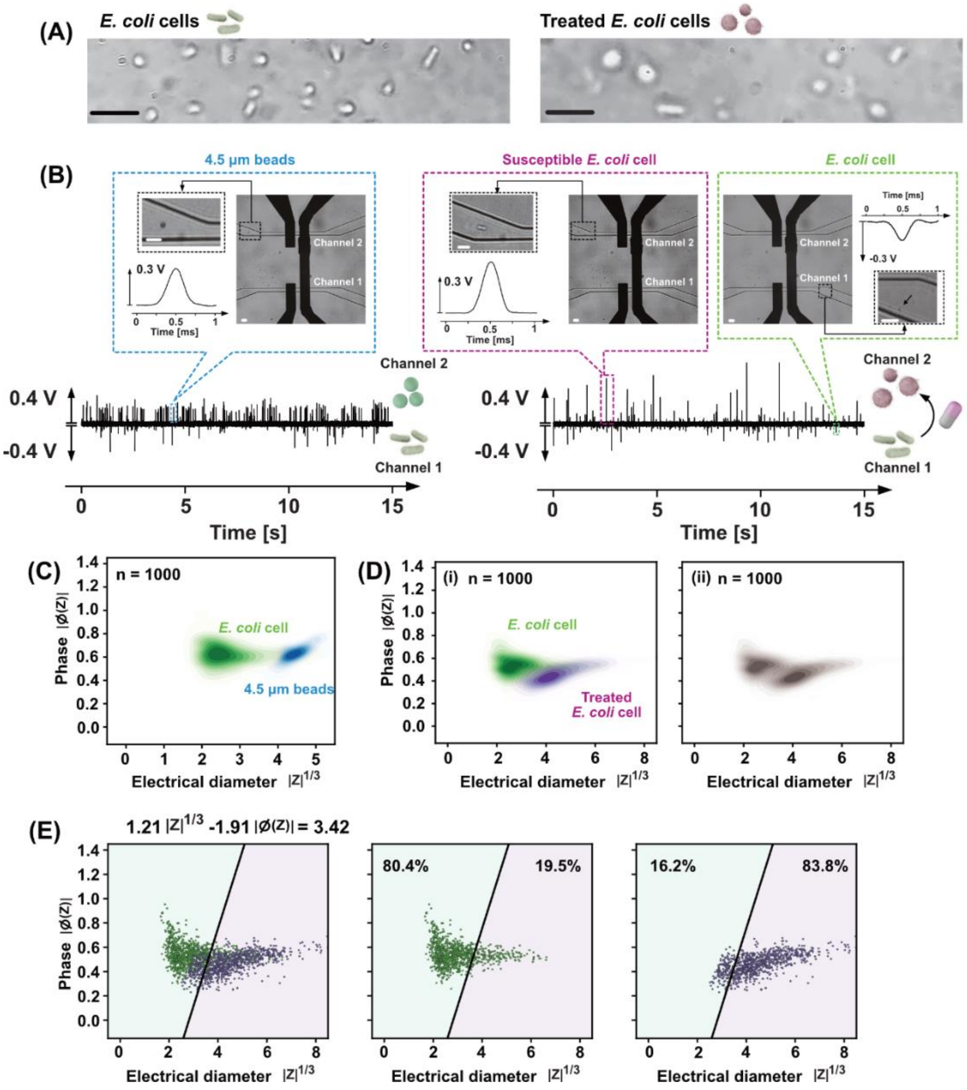

Fig. 3.23: Antibiotic susceptibility testing on *E. coli* cells by parallel impedance cytometry. (A) Morphological change in *E. coli* cells under the treatment of with 1 µg/ml of Mecillinam. The scale bar indicates 5 µm. (B) Raw signal analysis for 4.5µm beads, *E. coli* cells, and treated *E. coli* cells with Mecillinam. The scale bar denotes 10 µm. (C-D) Comparison of the electrical diameter versus phase of *E. coli* cells with (C) 4.5 µm beads and (D) treated E. coli cells: (i) colored and (ii) decolored distribution analysis. (E) Sorting results of *E. coli* cells based on the linear support vector machine.

Fig. 3.23B illustrates the raw impedance signals in two cases. In the first case, *E. coli* cells were in channel 1, and 4.5 µm polystyrene beads were in channel 2. The impedance pulses induced by single *E. coli* cells in channel 1 appear on the downside of the time series. In contrast, the impedance pulses of 4.5 μm beads in channel 2 are shown on upside of the same time series. It is easy to assess the size of single *E. coli* cells via raw impedance signals; some cells are half the size of the beads, while some are comparable to the beads. In the second case, *E. coli* cells were still in channel 1, but samples in channel 2 were changed to treated *E. coli* cells with Mecillinam. *E. coli* cells in channel 1 were employed as reference objects. On the upside of the raw impedance signal (channel 2), there were some pulses above 0.4 V, while on the downside (channel 1), most pulses were below 0.2 V. The high impedance pulse in channel 2 indicates that the volume of some *E. coli* cells increases. Through comparing the magnitude of the raw impedance signals on upside and downside of the time series, it is easy to estimate that the volume of some treated *E. coli* cells increased by at least 4 times. Besides, there was a large variation in the magnitude of the impedance pulses triggered by treated *E. coli* cells in channel 2. This means that not all *E. coli* cells are susceptible to this antibiotic, and some *E. coli* cells with low impedance (<0.2 V) might be resistant and did not response to the antibiotic. This is because most original *E. coli* cells have a magnitude of less than 0.2 V (see the downside of raw impedance signal, in Fig. 3.23A).

Fig. 3.23C shows the distribution analysis of one thousand *E. coli* cells and 4.5 μm beads in terms of the electrical diameter versus phase. The size distribution of *E. coli* varied compared to the stable size of 4.5 μm beads. The electrical diameters of *E. coli* cells are widely distributed, from approximately 2 to 4. Compared to the analysis based on raw signals, this analysis provides more accurate information regarding the morphology distribution of *E. coli* cells, which cannot be performed in real time.

As shown in Fig. 3.23D (i), *E. coli* cells treated with Mecillinam showed a rightward shift in electrical diameter. From the distribution analysis, I can conclude that some *E. coli* cells were susceptible to Mecillinam, which resulted in the increase of the volume of susceptible cells. In raw signal (see Fig. 3.23B), the susceptible cells are found to be of high impedance pulses. Additionally, there was an overlap in the distribution between *E. coli* and treated cells, indicating that some cells were not morphologically changed. In Fig. 6D (i), untreated and treated cells were distinguished by their color, untreated cells in channel 1 were labeled in green, and treated cells in channel 2 were labeled in purple. If both objects are measured in the same channel, this overlaps area would present a difficulty in analyzing how many cells change morphology. All cells were labeled with the same color (see Fig. 3.23D (ii)), and it was difficult to see how many cells responded to the antibiotic because it was impossible to distinguish the overlapping data between untreated and treated cells.

To analyze how many cells respond to the antibiotic, the phases and electrical diameters of objects in both channels were employed to fit a linear classifier based on the linear support vector machine [148]:

$$1.21 \times |Z|^{1/3} - 1.91 \times |\phi(Z)| = 3.42 \qquad \text{(Eq. 3.17)}$$

as shown in Fig. 3.23E, fitted equation 1 can divide the data from both channels into two areas. The left area of Equation 1 covers most untreated *E. coli* cells in channel 1, and the right area corresponds to most treated cells in channel 2. I can estimate how many cells are susceptible to antibiotics based on the number of treated cells (channel 2) on the right area. For example, only 19.5% untreated *E. coli* cells (channel 1) fall into the right area, but the number increases to 83.8% when treated with Mecillinam (channel 2). Therefore, I can conclude that more than 60% *E. coli* cells in channel 2 have morphology change in this case after antibiotic treatment.

3.3.1.5. Summary

Overall, I proposed the parallel impedance cytometry with a novel electrode layout, for real-time calibration of impedance detection, enabling the determination of target particle size determination by raw impedance signals. By simultaneously flowing the target and the reference suspensions into different channels, the impedance signals of two types of objects are shown in the time series, but on opposite sides. The size of target particles can be determined in real time by comparing the magnitude of the impedance pulses on the upside and downside. The sensitivity of the detection system can reach nanoscale, which was verified in simulation and experiments with nanoscale polystyrene beads. The system was also employed for antibiotic susceptibility testing of E. coli cells, and the results showed the capability of the system to monitor the response of single cells to antibiotics in real time. Additionally, the proportion of susceptible cells can also be quantified through statistical analysis of impedance pulses generated in both channels.

Together, I envision that this new impedance system could avoid the need for post processing and post calibration, and that the raw signal can provide as much information as possible in real-time detection. Additionally, this work paves a new path for antibiotic susceptibility testing, which can show the susceptibility of bacterial single cells in raw impedance signals with reference to control ones.

3.3.2. Machine learning-based impedance system

3.3.2.1. Experiment purposes and preparation

Impedance cytometry has enabled label-free and fast antibiotic susceptibility testing of bacterial single cells. Here, a machine learning-based impedance system is provided to score the phenotypic response of bacterial single cells to antibiotic treatment, with a high throughput of more than one thousand cells per min. In contrast to other impedance systems, an online training method on reference particles is provided, as the parallel impedance cytometry can distinguish reference particles from target particles, and label reference and target particles as the training and test set, respectively, in real time. Experiments with polystyrene beads of two different sizes (3 and 4.5 μm) confirm the functionality and stability of the system. Additionally, antibiotic-treated E. coli cells are measured every two hours during the six-hour drug treatment. All results successfully show the capability of real-time characterizing the change in dielectric properties of individual cells, recognizing single susceptible cells, as well as analysing the proportion of susceptible cells within heterogeneous populations in real time. As the intelligent impedance system can perform all impedance-based characterization and recognition of particles in real time, it can free operators from the post-processing and data interpretation.

The proposed intelligent impedance system consists of a parallel impedance cytometry and a machine learning-based impedance detection system. The performance of the intelligent impedance system (see Fig. 3.24) was evaluated by monitoring the changes in dielectric properties of thousands of single *E. coli* cells. The machine learning system is designed to distinguish susceptible individual cells from resistant ones in real time. Compared with other impedance cytometry devices, parallel impedance cytometry measures the impedance of target and reference particles in separate channels, and show their signals in the same time series with different orientation. The novel measurement method enables the automatic labelling of training set (reference particles) and test set (target particles). This feature provides a means of online training based on the reference particles whenever necessary.

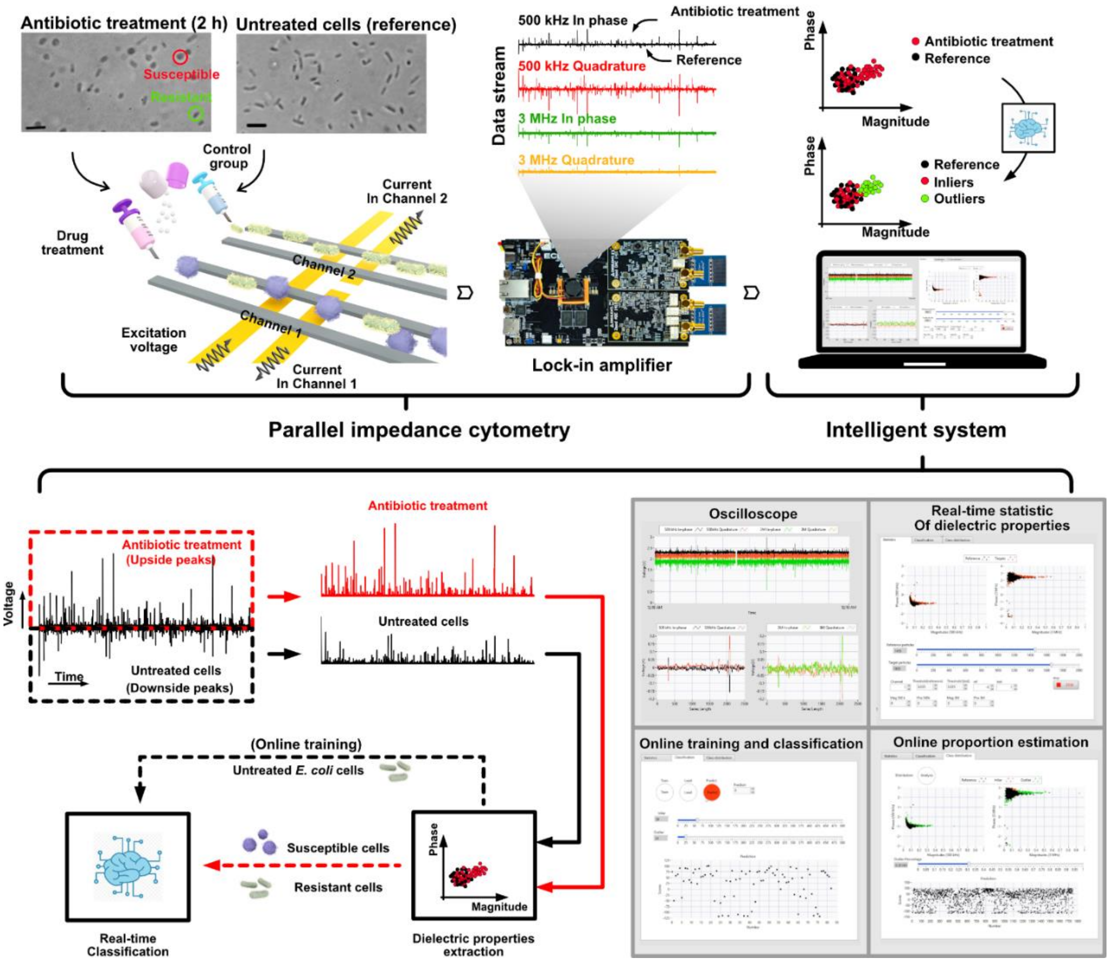

Fig. 3.24: Schematic of the intelligent impedance system, consisting of a parallel impedance cytometry and a machine learning-based detection system. The scale bar denotes 5 µm.

In this work, polystyrene beads (Polysciences, USA) of two different sizes: 3 µm and 4.5 µm, were employed first. To verify the possibility of separately measuring reference and target particles, 3 µm polystyrene beads are used as the reference in one channel, and the other channel is utilized to measure 3 µm beads or the mixture of 3 µm and 4.5 µm beads.

E. coli cells (XL2-Blue) were maintained at 37 ℃ and passaged every 12 to 16 hours. *E. coli* cells were treated with Mecillinam [137], [138] at a concentration of 2 µg/mL for 6 hours to induce the morphology change from rod-shaped to sphere-shaped [139]. *E. coli* cells (10 mL) is fixed with 70% alcohol at 23 ℃ every 2 hours. I manually stirred the cell-alcohol mixtures and placed them in a triple shaker at 100 rpm for about 2 hours to prevent the formation of aggregates. After the fixation, cells were centrifuged at 2500 rpm for 30 minutes and washed in 1× PBS. All fixed cells were suspended in the 1× PBS solution and stored at 4 ℃ in a refrigerator.

In experiments, samples were transferred to a 1× PBS solution with 0.1% Tween 20 solution, to avoid sample aggregation. A syringe pump was used to load sample suspension into the parallel microchannels at a flow rate of 0.8 µL/min. The images of beads and bacteria cells in the microchannels were taken using a high-speed camera (Photron. FASTCAM-APX RS 250K, Tech Imaging Ser-vices Inc., USA) at a frame rate of 20000 fps.

3.3.2.2. Detection mechanism

Fig. 3.24 illustrates the overall detection and signal-processing workflow of the intelligent impedance system, which consists of two main parts: (1) parallel impedance cytometry, and (2) machine learning-based detection system.

As for the parallel impedance cytometry, when particles suspended in an electrolyte flow pass through the detection electrodes one by one, the resultant perturbation on the propagation of AC current in two channels is converted by a lock-in amplifier [44], [85], [124], [125] into impedance pulses. The system allows rapid measurement of micron-sized particles in two parallel channels (with a cross section of 10 µm × 10 µm). The detection electrodes are 30 µm wide with spacing of 15 µm.

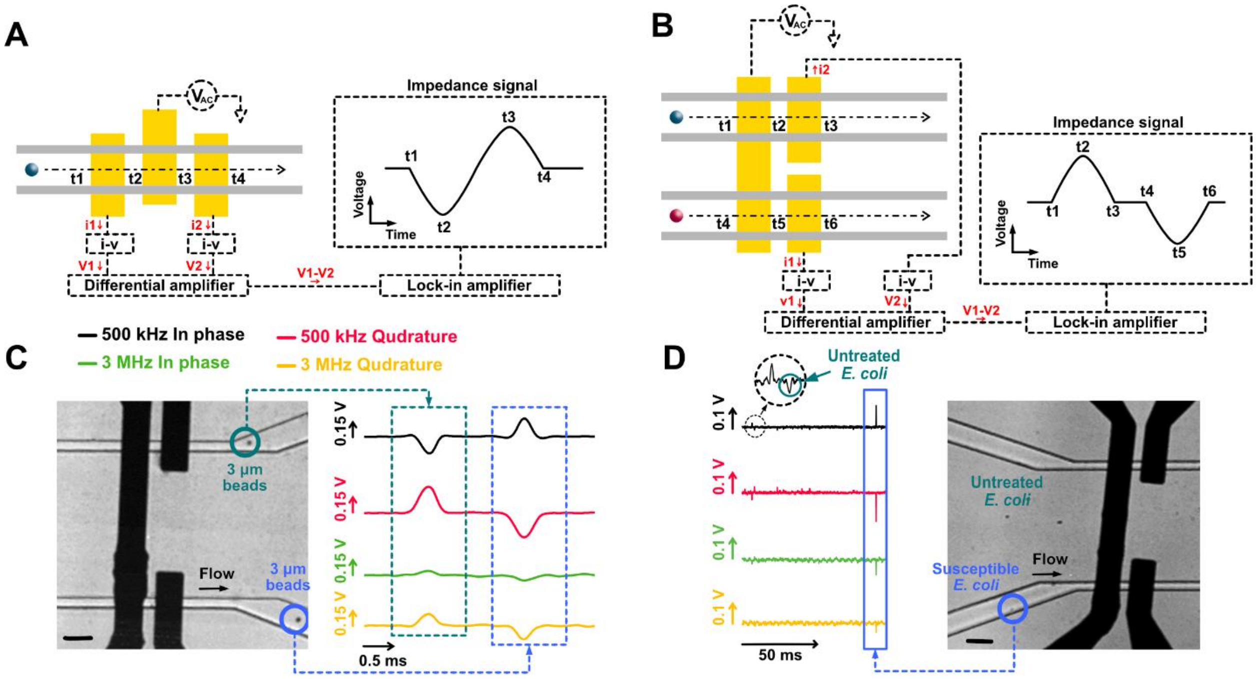

Fig. 3.25: Detection of polystyrene beads and E. coli cells using parallel impedance cytometry. (A) Top view of conventional impedance cytometry, (B) Schematic of parallel impedance cytometry, and (C-D) its detection results for (C) 3 µm beads and (D) E. coli cells of being antibiotic-treated and untreated for 2 hours. The scale bar is 30 µm.

In a conventional impedance cytometry device (see Fig. 3.25A), an AC voltage is applied to the center electrodes, while the two side electrodes serve as virtual grounds through transimpedance amplifiers (i-v converters), and current (i1 and i2) on the two side electrodes is converted into voltage (V1 and V2). The difference (V1-V2) between voltages V1 and V2 is converted to impedance signals through a lock-in amplifier. In Fig. 3.25A, the impedance signal of the particle at four specific times is shown, which reaches the downside and upside peaks, respectively, when the particle passing through the first span and the second span. The orientation of the impedance pulses is determined by the differential detection circuit. In contrast, parallel impedance cytometry employs the same differential detection circuit, but two detection electrodes are placed in two separate channels (Fig. 3.25B). The detection of particles in two microchannels was driven by an AC voltage via the left-side electrode. As a result, when a particle passes through the detection area of different microchannels, the induced impedance pulse has different orientations. In detail, the impedance pulses of reference and target particles are shown on the upside and down of the same time series, respectively.

The performance of parallel impedance cytometry for detecting polystyrene beads and *E. coli* cells with two different frequencies (500 kHz and 3 MHz) is briefly shown in Fig. 3.25C-Fig. 3.25D. When two polystyrene beads (3 μm) flowed through two microchannels separately (see Fig. 3.25C), there were two pulses appeared in the same impedance signal. Although these two impedance pulses have opposite orientation, there was no significant difference in their magnitude two detection frequencies. By comparing the upside impedance pulse with downside one, it is possible to benchmark the impedance of target single particles against the impedance of the reference particles in the other channel. In Fig. 3.25D, the impedance detection for *E. coli* cells treated by antibiotics for 2 hours (test group) and untreated *E. coli* cells (reference group) is shown. Untreated *E. coli* cells were measured as the reference in one channel, and antibiotic treated *E. coli* cells were detected in the other channel. After 2 h antibiotic treatment, some *E. coli* cells were susceptible to the antibiotic with morphology change (see Fig. 3.24), while some remained rod-shaped. The morphology change of *E. coli* cells by antibiotic treatment can be observed under a high-speed camera in parallel impedance cytometry, while untreated cells were too small to be clearly observed. The results showed that *E. coli* cells without treatment resulted in small impedance pulses, while susceptible *E. coli* cells induced an impedance pulse with a much larger magnitude in the opposite orientation (see Fig. 3.25D). The morphology change after antibiotic treatment can be assessed through the difference in magnitudes of impedance signals.

On the same side of the impedance signal of antibiotic-treated *E. coli*, there were also some tiny peaks, indicating that some *E. coli* cells did not respond to the antibiotic after two-hour treatment.

3.3.2.3. Real-time impedance statistic

When the data stream is generated from the parallel impedance cytometry, the intelligent impedance system can perform real-time signal processing to characterize the dielectric properties of single particles, including the phase and magnitude of the impedance pulses. The software is hybrid programmed using MATLAB (MathWorks, USA) and LabView (NI, USA)). The signal processing method is explained in the Experimental section (Subsection: Impedance signal analysis), and all dielectric properties are extracted by the software and shown on the user interface. The dielectric properties of individual particles at 500 kHz are labelled based on their detection channel, as shown in Fig. 3.26. The dielectric properties of individual particles at 3 MHz are presented in Fig. 3.27. In this case, the particles in the reference channel are marked as black, and those in the target channel are marked as red. The intelligent impedance system could separate target particles from reference particles automatically during signal processing, through manually setting the orientation of impedance pulses of both reference and target particles on the user interface (see Fig. 3.28).

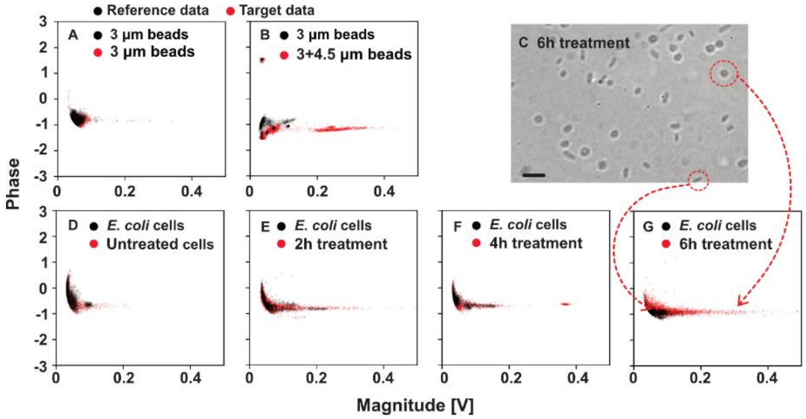

Fig. 3.26: Real-time characterization of the dielectric properties of polystyrene beads and E. coli cells using the intelligent impedance system, when the detection frequency is 500 kHz. (A-B) Impedance detection results for polystyrene beads (3 µm and 4.5 µm), in which 3 µm beads were employed as the reference in one channel, and (A) 3 µm beads or (B) the mixture of 3 µm and 4.5 µm beads were measured in another channel, respectively. (C) Image of E. coli cells after 6 h antibiotic treatment. The scale bar is 5 µm. (D-G) Impedance detection results for E. coli cells. One channel measured untreated E. coli cells as a reference, and another channel measured treated E. coli cells with different treatment durations, including (D) 0 h, (E) 2 h, (F) 4 h, and (G) 6 h.

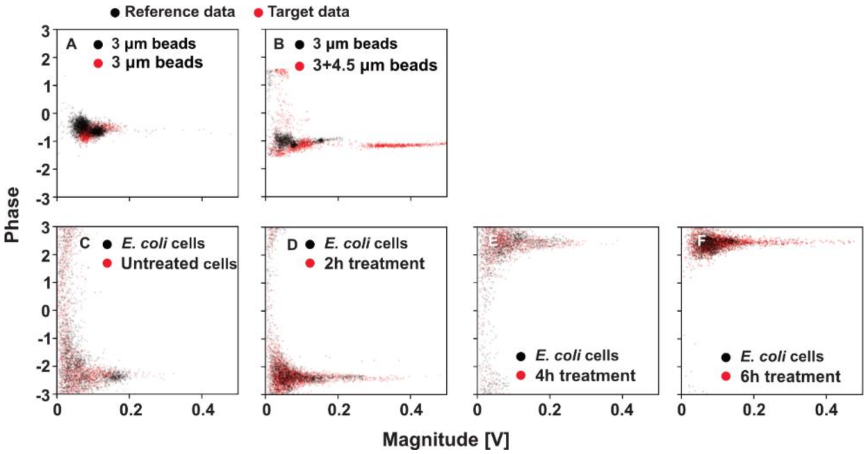

Fig. 3.27: Real-time dielectric property characterization using the intelligent impedance system at 3 MHz detection frequency. (A-B) Impedance detection for polystyrene beads (3 µm and 4.5 µm), in which 3 µm beads were employed as the reference in one channel, and (A) 3 µm beads or (B) the mixture of 3 µm and 4.5 µm beads were measured in another channel, respectively. (C-F) Antibiotic susceptibility testing of *E. coli* cells. One channel measured untreated *E. coli* cells as a reference, and another channel measured treated *E. coli* cells with different treatment durations, including (C) 0 h, (D) 2 h, (E) 4 h, and (F) 6 h.

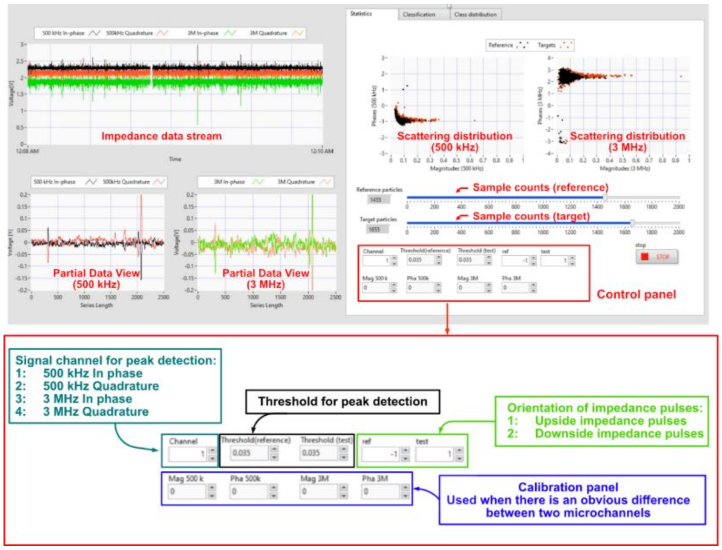

Channel: 1
Threshold(reference): 0.035
Threshold (test): 0.035
ref: -1
test: 1
Mag 500 k: 0
Pha 500k: 0
Mag 3M: 0
Pha 3M: 0

Fig. 3.28: User interface for real-time statistical analysis with the scattering distribution of dielectric properties. Users can determine which impedance pulses belong to target samples via the control panel. For example, the 500kHz in-phase impedance signal is employed to distinguish the reference and target particles (Channel: 1). The downside impedance pulses are induced by reference particles (ref: -1), and the upside impedance pulses corresponds to the target targets (test: 1). The threshold for the impedance detection is 0.035V (Threshold (reference): 0.035, and Threshold (test): 0.035). When the impedance pulses are above the threshold, the magnitude and phase of impedance pulses are extracted and shown in scattering plot.

As shown in Fig. 3.26A-Fig. 3.26B, polystyrene beads were employed to show the capability of the intelligence impedance system for the real-time detection and analysis (also see Fig. 3.28). When 3 μm beads were measured in both channels, the target data cluster (red) was covered by reference data cluster (black) (see Fig. 3.26A). Thus, the dielectric properties of the same particles are not impacted by the separate measurement in two channels. When injecting the mixture of 3 μm and 4.5 μm beads into the target channel, another data cluster appeared outside the reference data cluster. This is because the impedance magnitude increases with the diameter of the polystyrene beads [149]. In the scatter plot (see Fig. 3.26B), the data cluster for 3 μm beads in target channel is still mixed up with the reference data cluster. The dielectric properties of 4.5 μm beads are different from those of 3 μm beads, resulting in a bunch of outliers uncovered by the reference data cluster. When there are target particles with different dielectric properties from reference particles, the data of target particles are shown as outliers lying outside the reference cluster in the scatter plot of the intelligent impedance system.

E. coli cell is a gram-negative and rod-shaped bacterium, which is used as a model for antibiotic susceptibility testing in this work. Under 6 h treatment with 2 µg/ml of Mecillinam, susceptible *E. coli* cells suffered from cell division inhibition and morphological changes. For *E. coli* cells, the beta-lactam antibiotics (e.g., Mecillinam) can inhibit penicillin-binding proteins (PBPs) anchored in the cytoplasmic membrane [142], [143]. Specifically, the blocking of PBP-1 leads to rapid bacteria lysis [144], and the blocking of PBP-2 or PBP-3 results in the changes in morphological shape of *E. coli* [145], as well as the inability to septate after doubling of cell volume during cell multiplication [146]. As a result, resistant *E. coli* cells remain rod-shaped, while susceptible *E. coli* cells are spherical and increase in size (see Fig. 3.26C).

During 6 hours of treatment, the dielectric properties of drug-treated *E. coli* cells were measured as target particles every 2 hours, while untreated *E. coli* cells were measured in another channel as the reference (Fig. 3.26D-Fig. 3.26G). When there was no antibiotic treatment, the target data cluster was almost covered by the reference data cluster (see Fig. 3.26D). After 2 h treatment, some *E. coli* cells increased in size, as their impedance magnitudes increased (Fig. 3.26E). After 4 h treatment, there was an increase in the proportion of the target cluster that cannot be covered by the reference data cluster. At last, 6-hour treatment resulted in a clear change in the distribution of target data, and a large number of target cells were located outside the reference cluster (see Fig. 3.26G). It is obvious that the proportion of susceptible cells increased with the increase in antibiotic treatment duration, and some *E. coli* cells continued to grow in size. Additionally, *E. coli* cells were not all susceptible to antibiotics. I am able to distinguish susceptible cells from resistant ones, if their dielectric properties lie outside of the reference cluster.

3.3.2.4. Machine-learning-based workflow

In order to enable real-time recognition of the status of *E. coli* cells, a machine learning model is integrated into the intelligent impedance system. Here, the one-class support vector machine (SVM) was used as the classifier, which was trained on the dataset measured from the reference channel. During training processing, one-class SVM maps the reference dataset into a high dimensional feature space via the gaussian kernel function, and then determines the margin of the feature space. After training, one-class SVM [150]–[152] has the capability of recognizing outliers that lie outside the margin of the feature space. In other words, the trained one-class SVM is able to recognize unknown particles that are different from reference particles.

Fraction: 0

Inlier: 59

Outlier: 24

Fig. 3.29: User interface for the online training and prediction of the machine learning algorithm. The one-class SVM model was employed in this work. Users can train the model with reference targets by clicking the "Train" button at any time. The trained model can be loaded into the program by clicking the "Load" button. Clicking the "Predict" button means starting the real-time recognition of individual particles. The trained SVM model

can score individual samples. If the score is less than zero, the particle belongs to outliers which has much different from the reference particles. Otherwise, particles belong to inliers which has similar dielectric properties with reference particles.

The one-class SVM is established via MATLAB script, and the user interface is shown in Fig. 3.29. Once clicking the training bottom, LabView software transfers the reference dataset to the MABLAB node, and trains the one-class SVM algorithm. After that, the trained one-class SVM can be loaded to find out outliers from target particles. The workflow of the intelligent recognition is shown in Fig. 3.30A, and the system scores individual particles based on their dielectric properties at two frequencies. As the one-class SVM is trained on the dielectric properties of untreated *E. coli* cells, it has the ability to recognize susceptible cells and score them less than zero. The processing time for individual particle recognition based on their dielectric properties is 0.791 ± 0.078 ms, and the online training time takes up 25.3 ± 5.6 ms (using a PC with an Intel Core i5-9300H, @ 2.40 GHz CPU and 32 GB RAM)

Fig. 3.30B-Fig. 3.30C illustrate real-time recognition of polystyrene beads. In this case, 3 μm polystyrene beads were measured in one channel as the reference, and the obtained reference dataset was used for online training of the one-class SVM. When the same 3 μm polystyrene beads were measured in another channel (see Fig. 3.30B), most scores were greater than zeros, indicating that most particles have similar dielectric properties to reference particles. In contrast, when measuring the mixture of 3 and4.5 μm polystyrene beads, the scores of numerous particles were less than zeros, which means that outliers were detected in the target channel.

Fig. 3.30D-Fig. 3.30E show the real-time recognition of resistant and susceptible *E. coli* cells after 0 h and 6 h antibiotic treatment. Untreated *E. coli* cells were employed as the reference for the cells with antibiotic treatment. The one-class SVM was trained with the dielectric properties of untreated *E. coli* cells that were rod-shaped. When *E. coli* cells with 0 h treatment were detected in the microchannel, most cells were similar in morphology to the reference and resulted in a positive score (see Fig. 3.30D). In comparison, some *E. coli* cells exhibited morphology changes after 6 h treatment, which were marked out by the system with a negative score (see Fig. 3.30E).

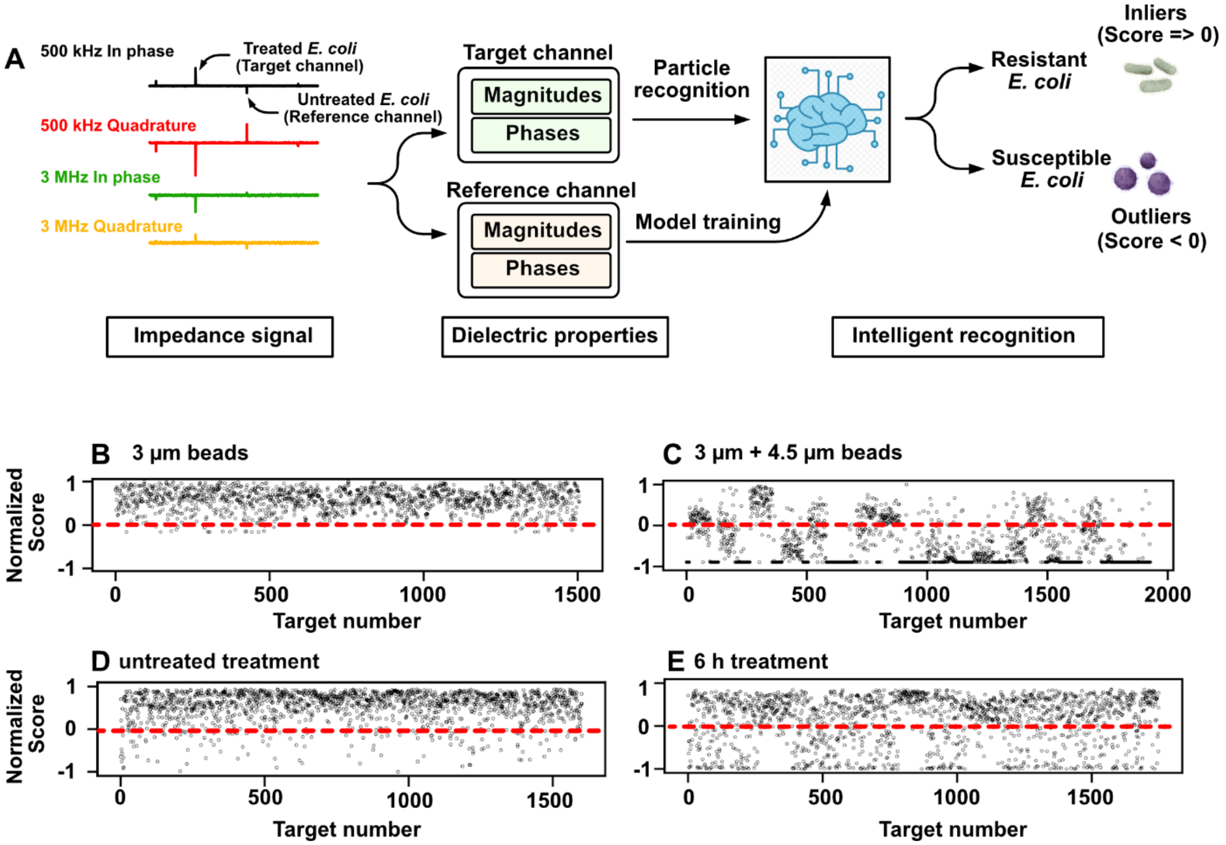

Fig. 3.30: Real-time single particle recognition using the intelligent impedance system. (A) Workflow of the real-time intelligent recognition of single particles. (B-C) Real-time intelligent recognition of polystyrene beads. When 3 μm polystyrene beads were measured as the reference in one channel, another channel was used to measure (B) 3 μm polystyrene beads and (C) the mixture of 3 μm and 4.5 μm, respectively. (C-D) Real-time intelligent recognition *E. coli* cells. When untreated *E. coli* cells were measured as the reference in one channel, another channel was employed for measuring *E. coli* cells with 0 h and 6 h antibiotic treatment. All scores were normalized to facilitate inter-comparisons between beads and *E. coli* cells.

3.3.2.5. Susceptible proportion estimation

The proportion of susceptible cells can be estimated through counting the number of *E. coli* cells that induce negative scores after the antibiotic treatment. In the intelligent impedance system, I integrated this function to statistically analyze the proportion of susceptible *E. coli* cells in all the cells measured. The user interface for estimating this proportion is shown in Fig. 3.31.

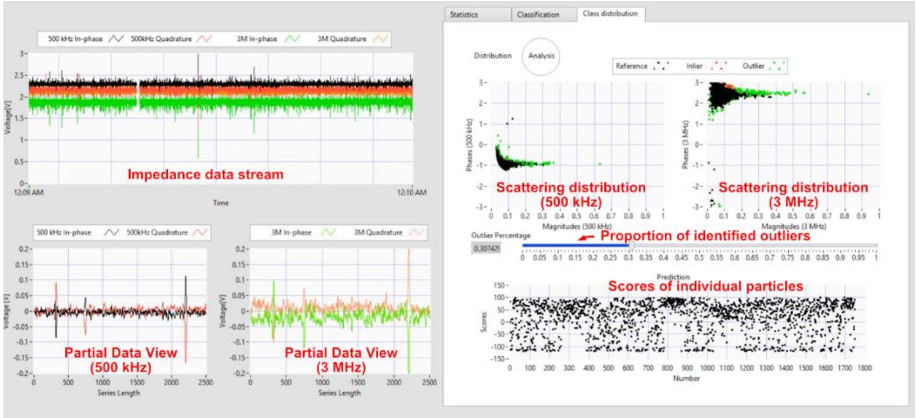

Fig. 3.31: User interface for analyzing the proportion of outliers. Users can analyze the distribution of recognized outliers and also their proportion in the total target particles, by clicking the "Analysis" button.

Fig. 3.32A-Fig. 3.32B illustrate the estimation of the proportion of outliers in total target particles. The outliers that are recognized by the system are marked as green. When detecting polystyrene beads, 3 μm polystyrene beads were employed as the reference, and their dielectric properties were used to train the one-class SVM in experiments. If there were only 3 μm polystyrene beads in the other channel, only 2 % of all the detected beads were mistakenly recognized as outliers (see Fig. 3.32A). By contrast, the proportion of outliers increased to 74%

after mixing 3 µm and 4.5 µm beads. Most data lying outside the reference data cluster can be recognized as outliers (see Fig. 3.32B).

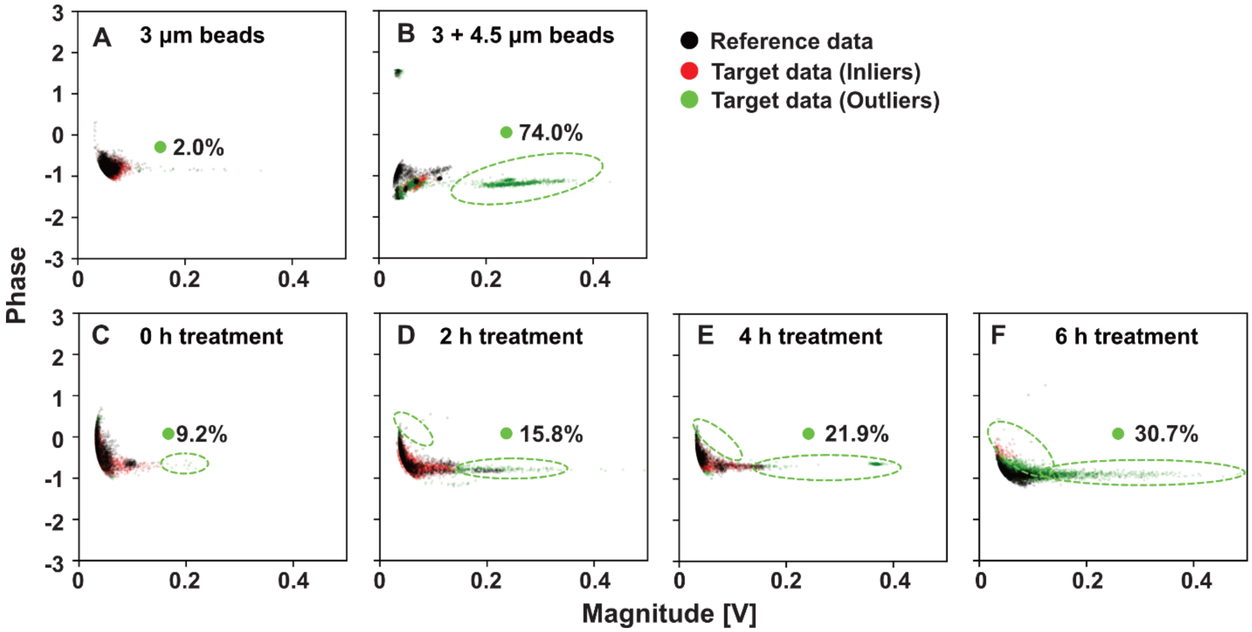

Fig. 3.32: Online estimation of the proportion of outliers in all measured target particles. The dielectric properties of single particles measured when the frequency is 500 kHz are shown. Reference particles are marked as black; inliers and outliers identified by the system are marked as red and green, respectively. (A-B) Online estimation results for polystyrene beads. 3 µm beads are measured in one channel as the reference, another channel is used to measure (A) 3 µm beads or (B) the mixture of 3 µm and 4.5 µm beads. (C-D) Online estimation results for *E. coli* cells. Untreated *E. coli* cells are measured in one channel as the reference, while the other channel is employed to measure *E. coli* cells treated by antibiotic for different durations: (C) 0 h, (D) 2 h, (E) 4 h and (F) 6 h.

Fig. 3.32C shows that 9.2% of 0-hour treated *E. coli* cells were mistakenly recognized as outliers, when benchmarking against untreated *E. coli* cells measured in the other channel as the reference. This proportion (9.2%) was greater than that of polystyrene beads (2%). This is because the morphology of *E. coli* cells is more heterogeneous than that of polystyrene beads. In treated cells, *E. coli* cells with morphology that differ greatly from the most cells may be recognized as outliers. After two-hour treatment, the proportion of outliers increased from 9.2% to 15.8%, and there was a clear cluster of outliers appeared in the scatter plot (see Fig. 3.32D). After four-hour treatment, 21.9% of target cells were found to have morphology change and recognized as outliers (see Fig. 3.32E). A longer treatment leads to an increase in the proportion of susceptible cells. After six-hour treatment, 30.7% of treated *E. coli* cells were found to have different dielectric properties from untreated cells (see Fig. 3.32F).

3.3.2.6. Discussion

In this section, I proposed an intelligent impedance system based on the parallel impedance cytometry, which enables the separate measurement of reference and target particles in different channels at the same time. This design allows the acquisition of impedance signals of reference and target particles as upside and downside pulses in the same time series, respectively. Through measuring polystyrene beads and *E. coli* cells, my system has demonstrated its capability of distinguishing the impedance pulses of reference and target particles by their orientation in real time, as well as characterizing the dielectric properties of single particle. All extracted data about the dielectric properties of reference and target particles are statistically shown on the user interface of system in real time. This feature enables operators to directly estimate the difference between the reference and target particles without post-processing.

Additionally, I integrated one-class SVM into the system for real-time recognition of single particles. The one-class SVM is trained by the dielectric properties of reference particles. If there are any particles with different dielectric properties from the reference particles, they would be recognized as outliers with negative scores. This function has been successfully verified to distinguish 4.5 μm beads from 3 μm beads, and to distinguish susceptible *E. coli* cells from resistant ones. In the future, the real-time recognition function can be integrated with sorting systems for more diverse applications [153], [154], for example, isolation of susceptible *E. coli* cells from heterogeneous populations for downstream analysis. Besides, I focused on the development of the intelligent impedance system in this work, and the one-class SVM was used due to its high-efficient training (25.3 ±5.6 ms) and prediction (0.791 ± 0.078 ms) process. The performance of the system could be further improved by employing more suitable machine learning algorithms.

To statistically analyze how many *E. coli* cells are sensitive to the antibiotics, I provided a user interface to show the proportion and distribution of susceptible cells in all measured *E. coli* cells. The experimental results successfully tracked the changes in the dielectric properties of susceptible *E. coli* cells. Compared to untreated *E. coli* cells, susceptible *E. coli* cells turns to be sphere-shaped with increased volume under the antibiotic treatment. As a result, most detected outliers have greater impedance magnitudes, indicating that they have larger volumes than reference cells. In addition to impedance magnitudes and phases, it has been [95] reported that the impedance opacity is sensitive to the changes in drug-treated bacterial cells. Therefore, I think that the recognition accuracy of the system could be improved by using more sensitive dielectric properties, such as tilt index [44], [124], pulse duration [45], [155], and impedance opacity [100], [156].

Overall, the intelligent impedance system demonstrated rapid antibiotic susceptibility testing of bacterial single cells. This system can perform digital signal processing and dielectric characterization automatically, which circumvents the need for post-processing and provide immediate data interpretation for operators. The integrated intelligent system enables the high-throughput recognition of the status of single cells in real time. The simplicity and automaticity of the system suggests that it is user-friendly for operators without any impedance background. I foresee that this method can pave the way toward next generation of intelligent impedance systems of rapid assays in biological clinical and environmental applications.

4. FPGA-based cell sorting control system

4.1. Femtosecond laser-based sorting techniques

4.1.1. Laser-induced cavitation

When a femtosecond laser pulse with enough energy is focused into liquid, a laser-induced plasma will generate and expand to form a cavitation bubble, as shown in Fig. 4.1. If the cavitation bubble propagates near an interface boundary, an asymmetrical collapse will occur, which generally leads to a directional single microjet.

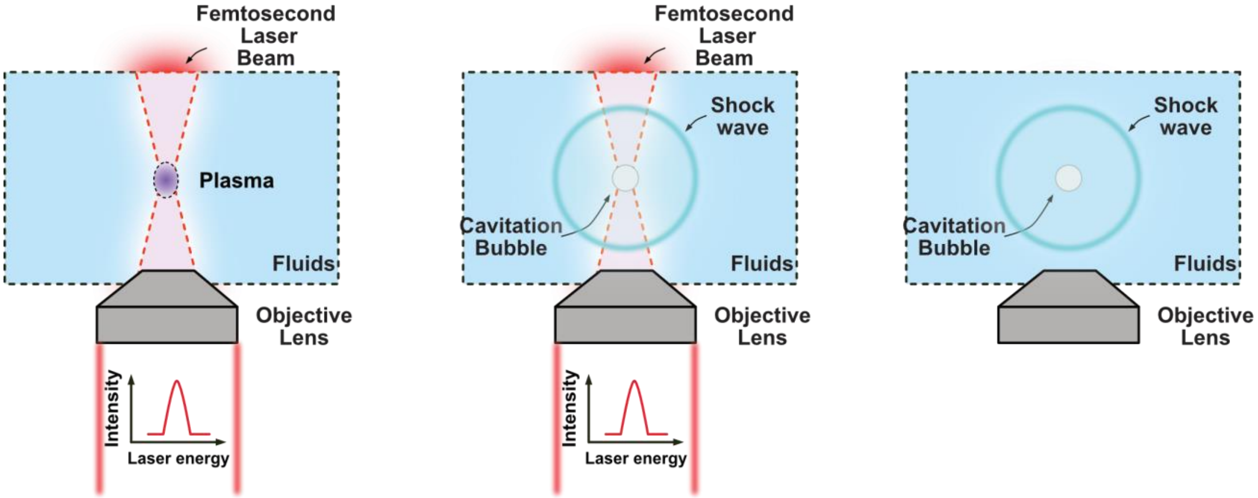

Fig. 4.1: Femtosecond laser-induced cavitation bubble and shock waves

Laser-induced cavitation is an optodynamic process where the optical energy of a high-intensity laser pulse is converted into the mechanical energy of dynamic phenomena, i.e., the expansion of a plasma, the propagation of a shock wave and the growth of a cavitation bubble. For such a process a laser pulse in the nanosecond range, focused into distilled water, is usually used to achieve highly localized ionization of liquid media, leading to plasma formation [157]–[159]. Rapid energy deposition during the optical breakdown causes rapid temperature and pressure increases within the plasma, thereby initiating its explosive expansion [160]. As a result of the optical breakdown is followed by the expansion of the shock wave and the growth of the cavitation bubble. When a cavitation bubble expands to its maximum volume, it is nearly empty. As a consequence, it starts to collapse due to the pressure of the surrounding liquid. However, after this collapse due to the pressure of the surrounding liquid. However, after this collapse, the bubble rebounds and the process repeat itself in the form of bubble oscillation. It is known that such a collapse in an infinite liquid is spherical and can be roughly described by the Rayleigh-Plesset model [161], [162].

4.1.2. Laser-induced microjet

A cavitation bubble developed near a boundary result in an asymmetric collapse [163]. Under suitable conditions, the deformation and collapse of the cavitation bubble near an interface result in the generation of liquid jet; the direction of this liquid jet during the collapse phase is determined by the physical properties of the boundary [164]. If the interface is rigid boundary, the jet is directed toward the wall, an oscillating bubble migrates toward the surface and the oscillation time are prolonged [165]–[167]. By contrast, in the case of a bubble collapse near a free surface, the jet is directed away from the free surface, the bubble migrates aways from the boundary during the collapse phases, the oscillation times are shortened [165], [167], [168].

In practical cell sorting processes, it is necessary to direct the microjet to target samples for the trajectory manipulation. It has to be mentioned that in the situation of immersed liquid the asymmetric collapse of cavitation bubbles near the solid sample boundary will lead to a microjet perpendicular to the sample. As shown in Fig. 4.2, my past work has shown the enhancing effect of the pocket structures on the fs laser-induced impulsive force [71]. Through the pocket structure, the impulsive force generated by single fs pulse enhanced and directed to the nearby particles.

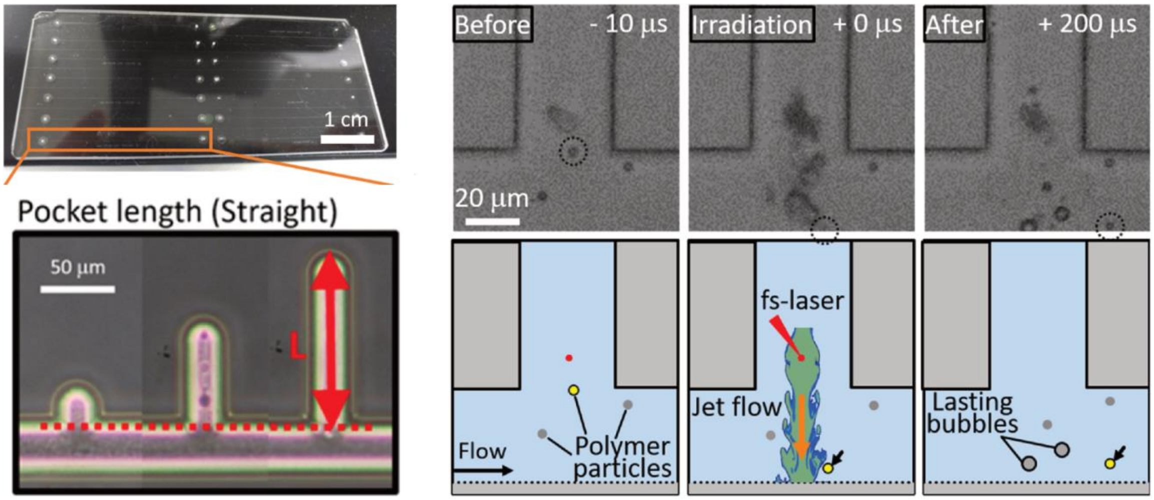

Fig. 4.2: Schematic of directed microjet to single particle by the micro-pocket [71]

4.2. Advantages of femto-second laser-based cell sorting

Sorting particles and cells from heterogeneous suspensions is an essential step in the processing and purification of complex mixtures for subsequent analysis and diagnosis [25]–[27]. Especially in many therapeutic and diagnostic practices, sorting process is widely used as the first step for drug screening[28], stem cell investigations[29], tissue and organ regeneration[30], and cancer diagnostics and therapy[31]–[33]. In order to isolate key cells one by one, precise sorting methods employ an external force (acoustic, electric, optical, or jet force) to manipulate the streamline of cells with certain biomarkers.

To date, there are numerous precise sorting methods and applications [27], many of which are based on acoustophoresis [66], [169], dielectrophoresis [170], [171], micro-electro-mechanical system (MEMS) [34], [172] and optical methods [173], [174]. For example, the traveling surface acoustic waves (TSAW) [55] has shown to realize volume-based cell sorting. However, standard acoustic microfluidic devices suffered from high voltage requirement (e.g., > 200 Vpp) and excess heat [52], [56]. Due to poor energy conversion, a large portion of the electrical energy used in acoustofluidic sorters is lost as heat, which weakens the biocompatibility of acoustofluidic sorters. Alternative is to use dielectrophoresis (DEP) methods and to realize cell sorting based on their intrinsic dielectric properties. A non-uniform electric field is employed to displace flowing objects into different balance positions [175]. The side effects [176] of DEP on biophysical properties and viability of cells limit its direct application to cell sorting, and the DEP-based sorting are typically performed with the droplet techniques [177], [178]. Additionally, magnetophoresis (MAP) has shown to realize a high-throughput cell sorting (83 kHz [68]), but labeling cells with magnetic beads or removing labels are laborious and difficult.

The femtosecond (fs) laser-assisted method [51] offers several advantages over other cell manipulation techniques, like the highest throughput, up to 100 kilohertz (kHz), which is far exceeding others, such as dielectrophoresis (DEP) (90 Hz [65]), traveling surface acoustic waves (TSAW) (4 kHz [66]), piezoelectric transducer (PZT) (23 kHz [67]). Besides, fs-laser-assisted binary sorting has reached a 100% success rate at a high throughput (100 kHz) for polystyrene beads, and a 63% success rate at an 83.3 kHz throughput for cells in previous work [51]. In this work, a jet flow is generated by the fs pulse irradiation and acts as an impulsive force on objects, i.e., the fs pulse irradiation generates shock and stress pressure waves, resulting in the jet flow. Recent research has demonstrated that the sorting process does not affect cell viability since no heat is generated during sorting process [69]. No physical heating makes it more biocompatible than other methods that use acoustofluidic [52], [56] or thermal-based [70] microdevice sorting techniques. Additionally, the strength of the impulsive force is determined by the pulse number, pulse energy, and pulse intervals of the fs-laser system [69], allowing for customized streamlining manipulation in a high-throughput system.

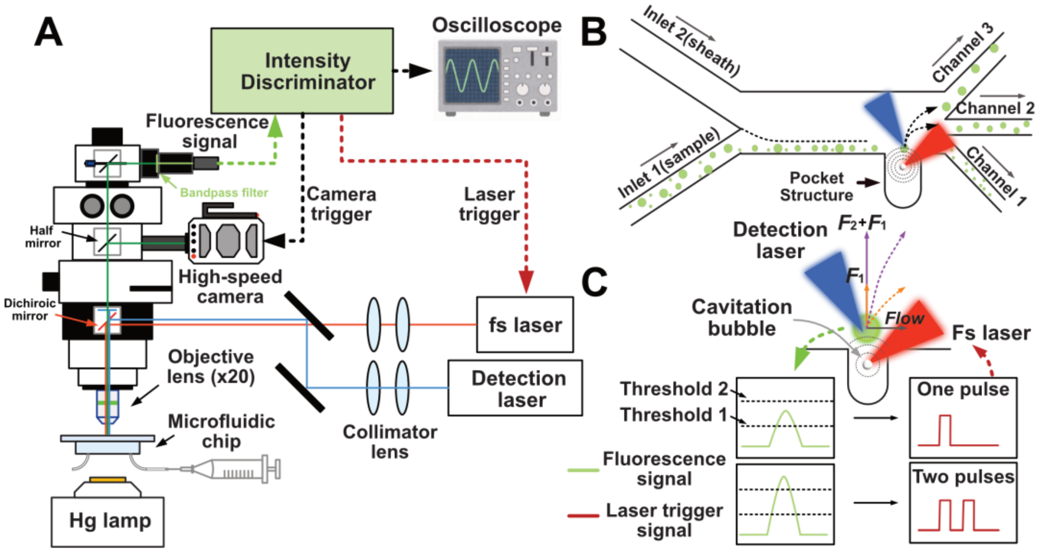

Fig. 4.3: Schematic of the fs-laser-assisted multi-selective system. Micro-objects are subjected to the impulsive force generated by the fs laser and separated into distinct outlet ports. The impulsive force is determined by the number of fs pulses. (A) Fluorescence detection and cell sorting experimental setup. (B) Operating concept of the fs-laser-assisted multi-selective system. (C) Schematic of the number control of the fs pulses based on different fluorescent intensities.

A fs-laser-assisted triple-selective system is presented in this work with the capacity to efficiently manipulate the streamline of individual cells/beads with varying fluorescence intensities into three different exit ports (see Fig. 4.3). A pocket structure was put on the channel wall next the fluorescence detection region, in order to ensure that all impulsive forces travel unidirectionally and focus at the sorting region [71]. In addition, the strength and duration of the impulsive force were evaluated as a function of the number of fs pulses by analyzing the streamline profile of the polystyrene beads. The experiments were performed on beads and cells of different sizes and fluorescence intensities, respectively. The results confirm the feasibility of using a fs laser for high-throughput triple-selective sorting, a first step toward constructing a high-throughput multi-selective system

4.3. FPGA-based control system and cell sorting

A fs-laser-assisted multi-selective system is presented in this section with the capacity to efficiently manipulate the streamline of individual cells/beads with varying fluorescence intensities into three different exit ports. A pocket structure (see Fig. 4.3) was put on the channel wall next the fluorescence detection region, in order to ensure that all impulsive forces travel unidirectionally and focus at the sorting region [71].

To realize such a multi-selective cell sorting system, The intensity discriminator is constructed on a FPGA board (Zynq UltraScale+ MPSoc XCZU9EG, Xilinx, USA) and is controlled by lab-developed scripts. Through switching between six states, the intensity discriminator (see Fig. 4.4A) determines the number of fs pulses based on the fluorescence intensity. Each state has a distinct action that can only be executed while the system is in that state. Depending on the trigger conditions, each state can continuously perform its own action or transition to the next state. The initial state is “S1: Detection”, which indicates that the detection system has been initialized and waits for a fluorescent object to be detected by the detection laser. When the fluorescent intensity exceeds the threshold 1 (2.5 V), the state S2 is initialized, generating a laser trigger with a width of 2 μs. If the maximum fluorescence intensity in state S3 exceeds threshold 2 (4 V), the second pulse is also generated in state S3. All induced laser triggers are arranged in the state S4. At the end of the rising edge of the fluorescence signal (see Fig. 4.4B), and the discrimination system sends the trigger signal to fs-laser system in state S5. Notably, the time delay of the first trigger was set to 10 μs in the single fs pulse case, and to 2 μs in the dual-pulse case, while the pulse interval was set to 6 μs. Following laser irradiation, the system switches to "S6: Stop Activity" to clear all activities and await the arrival of next fluorescence object.

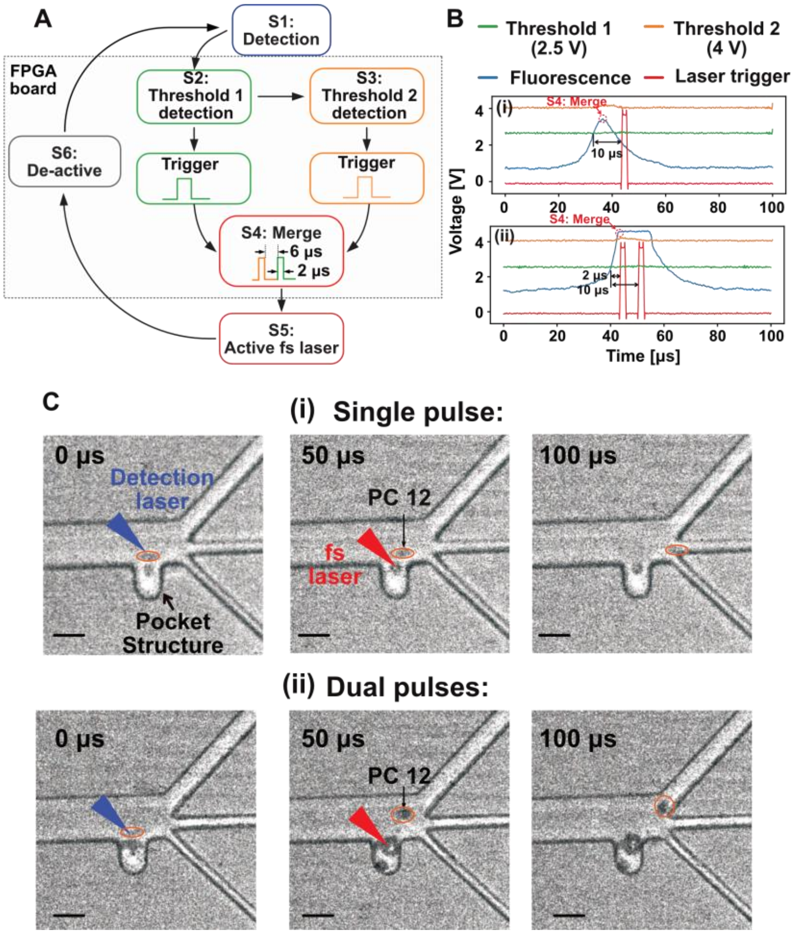

Fig. 4.4: Demonstrations of the cell sorting by the pulse control (A) Schematic of the intensity discrimination; (B) Oscilloscope illustration of the fluorescence signal and laser trigger signal in the case of (i) single pulse and (ii) dual pulses; (C) Experimental results on PC12 cells in the case of (i) single pulse and (ii) dual pulses, the scale bar represents 40 μm

Two thresholds of 2.5 V and 4 V were determined in this section (see Fig. 4.4), and the sorting steps of the multi-selective system were demonstrated using PC 12 cells an example. To begin, the fluorescence detector transferred the fluorescence intensity of PC 12 cells into voltage signals, through a PMT. When the fluorescence voltage of the target cell was greater than 2.5 V (see Fig. 4.4B), a single fs pulse was activated, and the PC 12 was pushed into the channel 2 (see Fig. 4.4C). By contrast, when the fluorescence voltage exceeded 4 V (see Fig. 4.4B), the PC 2 cell was deflected to the channel 3 by double fs pulses (see Fig. 4.4C). Additionally, the microfluidic chip also owns a waste channel (channel 1) for the collection of cells/beads with little or no fluorescence.

4.4. Summary

At current stages, the FPGA-based cell sorting system is employed in the fluorescence-triggered cell system. It has the capacity of determining the fs laser pulses through the fluorescence strength of target samples. Consequently, samples with varying fluorescence strength would be leaded to different outputs under the fs laser-induced acoustic force.

Notably, the FPGA-based cell sorting system (Chapter 4) is still under the development. This chapter only introduced the design and development of the control system for the fs laser. The future work is to integrate the impedance cytometry (Chapter 3) with the cell sorting system (Chapter 4), so that the cell sorting process can be triggered by the impedance signals, stead of the fluorescence signals. Therefore, the final purpose is to construct a FPGA-based single cell detection and sorting system, which can recognize and isolate the target cell based on their dielectric properties.

- The position and role of this Chapter 4 is unclear to me. After reading thesis, I understand that fs-laser system is something like a competitor to impedance-based system. But after presentation, my understanding changes to that impedance-based and fs-laser systems co-work. Please clearly explain the relationship of impedance and fs-laser systems.

Repones:

Thanks for your comments. The revised thesis provides more information about the relationship between the chapter 3 and chapter 4 at the end of the **subsection 4.4: Summary.**

The aim of the chapter 3 is to detect single cells, so that to distinguish these specific ones from others with our developed detection system. After that, chapter 4 shows a method to isolate these special cells from others via our developed sorting system. However, to date, the work did not come to an end, and the future work is to integrate the cell detection system (chapter 3) with the sorting system (chapter 4), so that to employ the impedance signals to control the cell sorting.

- Relating to above comment, if impedance and fs-laser is in competition, what is a conclusion of chapter 3 and 4? Do you want to conclude that impedance-based one is better than fs-laser based one? If so, please comment it clearly, and table for comparison will be informative.

Response:

Thanks for your comments. The Chapter 3 and chapter 4 are not in competition. Currently, I did not merge both systems together successfully, and therefore, I introduced they separately in different chapters.

5. General conclusion

This dissertation focused on the development of single cell detection and sorting system. I successfully developed a Field Programmable Gate Arrays (FPGA)-based impedance detection system. the FPGA-based impedance cytometry helps us to analyze the shape of single cells in a high throughput manner (>1000 cells/s). Besides, I extended the application of impedance detection into the intracellular analysis, so that to monitor the intracellular components distribution, and also to track the changes in single cell weight.

Unlike real-time visual measurements, impedance detection does not indicate the electrical diameter or opacity of single objects immediately, but needs post-calibration. My work presents a redesigned differential impedance cytometry system enabling real-time calibration of the impedance signal, called parallel impedance cytometry. Parallel dual microchannels allow simultaneous detection of both reference objects and suspension targets in independent channels. A unique electrode layout allows display of impedance pulses independent of channel in a single time series, which is confirmed in simulations and experiments. The impedance waveform can be directly used to assess the electrical properties of single objects without the need for long-term statistical analysis afterwards. Experiments on polystyrene beads confirm the nano-sensitivity of the system. In addition, antimicrobial susceptibility testing on E. coli indicates that my system can track the volume change and proportion of sensitive bacteria. The findings indicate that the novel impedance cytometry provides a new pathway for accurate morphology tracking and real-time volume analysis for submicron to micron-scale objects.

For further simplification of the post-process of the data, my dissertation provided an intelligent impedance system based on the parallel impedance cytometry. The parallel impedance cytometry enables the separate measurement of reference and target particles in different channels at the same time. Impedance signals of reference and target particles are indicated in the same time series as upside and downside pulses. The intelligent impedance system is able to do on-line training with the dielectric properties of reference particles at any time during experiments. Besides, the trained intelligent system enables the real-time recognition of outliers in the target particles which benchmark against the reference particles. Due to the system's simplicity and automaticity, it is easy to use for operators who have no background in impedance. I foresee that this method can pave the way toward next generation of intelligent impedance systems of rapid assays in biological clinical and environmental applications.

Additionally, for the femtosecond laser-based research, I developed a control system based on a FPGA board (ALINX, AXU9EG), aimed at the control of the femtosecond laser pulses. Through the developed system, I can determine the number of femtosecond laser pulses based on the amplitude of trigger system. This system can be integrated with several types of detection system for the single cell manipulation in the microchannel, like the forementioned impedance detection system or the fluorescence detection system. With the capability of controlling the femtosecond laser pulses, the force acting on the single cells is also controllable for us, which enabled us to direct different cells to different outputs based on their certain properties.

In my initial plan, I proposed to use femtosecond laser to induce acoustic forces for single cell characterization. For this plan, I have realized the label-free impedance detection system and also developed a system for controlling the femtosecond laser pulses. In future, I hope to integrate both together, and then I can trigger the femtosecond laser pulses to induce the acoustic waves when individual cells pass through the detection area. Therefore, by far, I think that I have completed most of the initial plan.

Reference

[1] J. A. Rodrigo, J. M. Soto, and T. Alieva, “Fast label-free microscopy technique for 3D dynamic quantitative imaging of living cells,” *Biomedical Optics Express*, 2017, doi: 10.1364/boe.8.005507.

[2] R. H. Adamson, “Microvascular endothelial cell shape and size in situ,” *Microvascular Research*, vol. 46, no. 1, 1993, doi: 10.1006/mvre.1993.1036.

[3] M. Navarro, J. Ruberte, and A. Carretero, “Myology,” *Morphological Mouse Phenotyping: Anatomy, Histology and Imaging*, pp. 63–88, Jan. 2017, doi: 10.1016/B978-0-12-812972-2.50004-0.

[4] A. Prasad and E. Alizadeh, “Cell Form and Function: Interpreting and Controlling the Shape of Adherent Cells,” *Trends in Biotechnology*, vol. 37, no. 4. 2019. doi: 10.1016/j.tibtech.2018.09.007.

[5] M. Eisenberg-Bord, N. Shai, M. Schuldiner, and M. Bohnert, “A Tether Is a Tether Is a Tether: Tethering at Membrane Contact Sites,” *Developmental Cell*, vol. 39, no. 4. 2016. doi: 10.1016/j.devcel.2016.10.022.

[6] Y. Guo *et al.*, “Visualizing Intracellular Organelle and Cytoskeletal Interactions at Nanoscale Resolution on Millisecond Timescales,” *Cell*, vol. 175, no. 5, 2018, doi: 10.1016/j.cell.2018.09.057.

[7] I. M. Tolić-Nørrelykke, “Push-me-pull-you: How microtubules organize the cell interior,” in *European Biophysics Journal*, 2008, vol. 37, no. 7. doi: 10.1007/s00249-008-0321-0.

[8] D. T. Butcher, T. Alliston, and V. M. Weaver, “A tense situation: Forcing tumour progression,” *Nature Reviews Cancer*, vol. 9, no. 2. 2009. doi: 10.1038/nrc2544.

[9] G. C. Yuan *et al.*, “Challenges and emerging directions in single-cell analysis,” *Genome Biology*, vol. 18, no. 1. 2017. doi: 10.1186/s13059-017-1218-y.

[10] S. Palit, C. Heuser, G. P. de Almeida, F. J. Theis, and C. E. Zielinski, “Meeting the challenges of high-dimensional single-cell data analysis in immunology,” *Frontiers in Immunology*, vol. 10, no. JUL, 2019, doi: 10.3389/fimmu.2019.01515.

[11] R. A. Hoffman, “Pulse width for particle sizing,” *Current Protocols in Cytometry*, no. SUPPL.50. 2009. doi: 10.1002/0471142956.cy0123s50.

[12] M. Brown and C. Wittwer, “Flow Cytometry: Principles and Clinical Applications in Hematology,” *Clinical Chemistry*, vol. 46, no. 8, pp. 1221–1229, Aug. 2000, doi: 10.1093/CLINCHEM/46.8.1221.

[13] A. Binek *et al.*, “Flow Cytometry Has a Significant Impact on the Cellular Metabolome,” *Journal of Proteome Research*, vol. 18, no. 1, pp. 169–181, Jan. 2019, doi: 10.1021/ACS.JPROTEOME.8B00472/ASSET/IMAGES/LARGE/PR-2018-00472T_0005.JPEG.

[14] N. S. Barteneva, E. Fasler-Kan, and I. A. Vorobjev, “Imaging Flow Cytometry: Coping with Heterogeneity in Biological Systems,” *Journal of Histochemistry and Cytochemistry*, vol. 60, no. 10, pp. 723–733, Oct. 2012, doi: 10.1369/0022155412453052.

[15] Y. Han, Y. Gu, A. C. Zhang, and Y. H. Lo, “Review: Imaging technologies for flow cytometry,” *Lab on a Chip*, vol. 16, no. 24. 2016. doi: 10.1039/c6lc01063f.

[16] M. Henriksen, “Quantitative imaging cytometry: instrumentation of choice for automated cellular and tissue analysis,” *Nature Methods 2010 7:4*, vol. 7, no. 4, pp. i–ii, Apr. 2010, doi: 10.1038/nmeth.f.302.

[17] P. Pozarowski, E. Holden, and Z. Darzynkiewicz, “Laser scanning cytometry: Principles and applications-an update,” *Methods in Molecular Biology*, vol. 931, 2012, doi: 10.1007/978-1-62703-56-4_11.

[18] M. C. Cheung, B. McKenna, S. S. Wang, D. Wolf, and D. J. Ehrlich, “Image-based cell-resolved screening assays in flow,” *Cytometry Part A*, vol. 87, no. 6, 2015, doi: 10.1002/cyto.a.22609.

[19] B. T. Bosworth and M. A. Foster, “High-speed ultrawideband photonically enabled compressed sensing of sparse radio frequency signals,” *Optics Letters, Vol. 38, Issue 22, pp. 4892-4895*, vol. 38, no. 22, pp. 4892–4895, Nov. 2013, doi: 10.1364/OL.38.004892.

[20] B. T. Bosworth, D. N. Tran, J. R. Stroud, M. A. Foster, S. Chin, and T. D. Tran, “Continuous high-rate photonically-enabled compressed sensing (CHiRP-CS) for high speed flow microscopy,” *Imaging and Applied Optics 2015 (2015), paper CTh3E.3*, p. CTh3E.3, Jun. 2015, doi: 10.1364/COSI.2015.CTH3E.3.

[21] S. Stavrakis, G. Holzner, J. Choo, and A. deMello, “High-throughput microfluidic imaging flow cytometry,” *Current Opinion in Biotechnology*, vol. 55, pp. 36–43, Feb. 2019, doi: 10.1016/J.COPBIO.2018.08.002.

[22] H. Mikami *et al.*, “Virtual-freezing fluorescence imaging flow cytometry,” *Nature Communications*, vol. 11, no. 1, p. 1162, Dec. 2020, doi: 10.1038/s41467-020-14929-2.

[23] S. Gawad, K. Cheung, U. Seger, A. Bertsch, and P. Renaud, “Dielectric spectroscopy in a micromachined flow cytometer: theoretical and practical considerations,” *Lab on a Chip*, vol. 4, no. 3, p. 241, 2004, doi: 10.1039/b313761a.

[24] T. Sun and H. Morgan, “Single-cell microfluidic impedance cytometry: a review,” *Microfluidics and Nanofluidics*, vol. 8, no. 4, pp. 423–443, Apr. 2010, doi: 10.1007/s10404-010-0580-9.

[25] A. A. Nawaz *et al.*, “Intelligent image-based deformation-assisted cell sorting with molecular specificity,” *Nature Methods 2020 17:6*, vol. 17, no. 6, pp. 595–599, May 2020, doi: 10.1038/s41592-020-0831-y.

[26] N. Nitta *et al.*, “Raman image-activated cell sorting,” *Nature Communications*, vol. 11, no. 1, p. 3452, Dec. 2020, doi: 10.1038/s41467-020-17285-3.

[27] Y. Shen, Y. Yalikun, and Y. Tanaka, “Recent advances in microfluidic cell sorting systems,” *Sensors and Actuators, B: Chemical*, vol. 282, no. August 2018, pp. 268–281, 2019, doi: 10.1016/j.snb.2018.11.025.

[28] P. M. Haverty *et al.*, “Reproducible pharmacogenomic profiling of cancer cell line panels,” *Nature 2016 533:7603*, vol. 533, no. 7603, pp. 333–337, May 2016, doi: 10.1038/nature17987.

[29] Y. Zhu *et al.*, “Proteomic Analysis of Single Mammalian Cells Enabled by Microfluidic Nanodroplet Sample Preparation and Ultrasensitive NanoLC-MS,” *Angewandte Chemie*, vol. 130, no. 38, pp. 12550–12554, Sep. 2018, doi: 10.1002/ANGE.201802843.

[30] A. Scialdone *et al.*, “Resolving early mesoderm diversification through single-cell expression profiling,” *Nature 2016 535:7611*, vol. 535, no. 7611, pp. 289–293, Jul. 2016, doi: 10.1038/nature18633.

[31] D. T. Miyamoto *et al.*, “RNA-Seq of single prostate CTCs implicates noncanonical Wnt signaling in antiandrogen resistance,” *Science (1979)*, vol. 349, no. 6254, pp. 1351–1356, Sep. 2015, doi: 10.1126/SCIENCE.AAB0917.

[32] J. I. Varillas *et al.*, “Microfluidic Isolation of Circulating Tumor Cells and Cancer Stem-Like Cells from Patients with Pancreatic Ductal Adenocarcinoma,” *Theranostics*, vol. 9, no. 5, p. 1417, 2019, doi: 10.7150/THNO.28745.

[33] D. Lin *et al.*, “Screening Therapeutic Agents Specific to Breast Cancer Stem Cells Using a Microfluidic Single-Cell Clone-Forming Inhibition Assay,” *Small*, vol. 16, no. 9, p. 1901001, Mar. 2020, doi: 10.1002/SMLL.201901001.

[34] Y. Kasai *et al.*, “Breakthrough in purification of fossil pollen for dating of sediments by a new large-particle on-chip sorter,” *Science Advances*, vol. 7, no. 16, p. eabe7327, Apr. 2021, doi: 10.1126/sciadv.abe7327.

[35] S. Pechhold *et al.*, “Transcriptional analysis of intracytoplasmically stained, FACS-purified cells by high-throughput, quantitative nuclease protection,” *Nature Biotechnology*, vol. 27, no. 11, pp. 1038–1042, Nov. 2009, doi: 10.1038/nbt.1579.

[36] D. A. Lawson *et al.*, “Single-cell analysis reveals a stem-cell program in human metastatic breast cancer cells,” *Nature*, vol. 526, no. 7571, pp. 131–135, Oct. 2015, doi: 10.1038/nature15260.

[37] S. Boddington, T. D. Henning, E. J. Sutton, and H. E. Daldrup-Link, “Labeling Stem Cells with Fluorescent Dyes for non-invasive Detection with Optical Imaging,” *Journal of Visualized Experiments*, no. 14, Apr. 2008, doi: 10.3791/686.

[38] L. Xing *et al.*, “Mesenchymal stem cells, not conditioned medium, contribute to kidney repair after ischemia-reperfusion injury,” *Stem Cell Research & Therapy*, vol. 5, no. 4, p. 101, 2014, doi: 10.1186/scrt489.

[39] S. SARTORE *et al.*, “Amniotic mesenchymal cells autotransplanted in a porcine model of cardiac ischemia do not differentiate to cardiogenic phenotypes,” *European Journal of Cardio-Thoracic Surgery*, vol. 28, no. 5, pp. 677–684, Nov. 2005, doi: 10.1016/j.ejcts.2005.07.019.

[40] S. Hamann, J. F. Kiilgaard, T. Litman, F. J. Alvarez-Leefmans, B. R. Winther, and T. Zeuthen, “Measurement of Cell Volume Changes by Fluorescence Self-Quenching,” *Journal of Fluorescence*, vol. 12, no. 2, pp. 139–145, 2002.

[41] A. Andrzejewska *et al.*, “Labeling of human mesenchymal stem cells with different classes of vital stains: robustness and toxicity,” *Stem Cell Research & Therapy*, vol. 10, no. 1, p. 187, Dec. 2019, doi: 10.1186/s13287-019-1296-8.

[42] V. Roukos, G. Pegoraro, T. C. Voss, and T. Misteli, “Cell cycle staging of individual cells by fluorescence microscopy,” *Nature Protocols*, vol. 10, no. 2, pp. 334–348, Feb. 2015, doi: 10.1038/nprot.2015.016.

[43] A. Ferro, T. Mestre, P. Carneiro, I. Sahumbaiev, R. Seruca, and J. M. Sanches, “Blue intensity matters for cell cycle profiling in fluorescence DAPI-stained images,” *Laboratory Investigation*, vol. 97, no. 5, pp. 615–625, May 2017, doi: 10.1038/labinvest.2017.13.

[44] T. Tang *et al.*, “Microscopic impedance cytometry for quantifying single cell shape,” *Biosensors and Bioelectronics*, p. 113521, Aug. 2021, doi: 10.1016/j.bios.2021.113521.

[45] C. Honrado, P. Bisegna, N. S. Swami, and F. Caselli, "Single-cell microfluidic impedance cytometry: From raw signals to cell phenotypes using data analytics," *Lab on a Chip*. 2021. doi: 10.1039/d0lc00840k.

[46] R. Huisjes, A. Bogdanova, W. W. van Solinge, R. M. Schiffelers, L. Kaestner, and R. van Wijk, "Squeezing for Life – Properties of Red Blood Cell Deformability," *Frontiers in Physiology*, vol. 0, no. JUN, p. 656, Jun. 2018, doi: 10.3389/FPHYS.2018.00656.

[47] J. Kim, H. Lee, and S. Shin, "Advances in the measurement of red blood cell deformability: A brief review," *Journal of Cellular Biotechnology*, vol. 1, no. 1, pp. 63–79, Jan. 2015, doi: 10.3233/JCB-15007.

[48] Y. Hao, S. Cheng, Y. Tanaka, Y. Hosokawa, Y. Yalikun, and M. Li, "Mechanical properties of single cells: Measurement methods and applications," *Biotechnology Advances*, vol. 45, Dec. 2020, doi: 10.1016/J.BIOTECHADV.2020.107648.

[49] M. Xu *et al.*, "Morphological Indicator for Directed Evolution of Euglena gracilis with a High Heavy Metal Removal Efficiency," *Environmental Science & Technology*, vol. 55, no. 12, pp. 7880–7889, Jun. 2021, doi: 10.1021/acs.est.0c05278.

[50] P. Liu, H. Liu, D. Yuan, D. Jang, S. Yan, and M. Li, "Separation and Enrichment of Yeast Saccharomyces cerevisiae by Shape Using Viscoelastic Microfluidics," *Analytical Chemistry*, vol. 93, no. 3, pp. 1586–1595, Jan. 2020, doi: 10.1021/ACS.ANALCHEM.0C03990.

[51] T. Iino *et al.*, "High-speed microparticle isolation unlimited by Poisson statistics," *Lab on a Chip*, 2019, doi: 10.1039/c9lc00324j.

[52] R. Zhong *et al.*, "Acoustofluidic Droplet Sorter Based on Single Phase Focused Transducers," *Small*, p. 2103848, Oct. 2021, doi: 10.1002/SMLL.202103848.

[53] Q. Guo, S. P. Duffy, K. Matthews, E. Islamzada, and H. Ma, "Deformability based Cell Sorting using Microfluidic Ratchets Enabling Phenotypic Separation of Leukocytes Directly from Whole Blood," *Scientific Reports*, vol. 7, no. 1, p. 6627, Dec. 2017, doi: 10.1038/s41598-017-06865-x.

[54] E. Henry *et al.*, "Sorting cells by their dynamical properties," *Scientific Reports*, vol. 6, no. 1, p. 34375, Dec. 2016, doi: 10.1038/srep34375.

[55] M. Afzal, J. Park, J. S. Jeon, M. Akmal, T.-S. Yoon, and H. J. Sung, "Acoustofluidic Separation of Proteins Using Aptamer-Functionalized Microparticles," *Analytical Chemistry*, vol. 93, no. 23, pp. 8309–8317, Jun. 2021, doi: 10.1021/acs.analchem.1c01198.

[56] K. Yamanouchi and H. Furuyashiki, "New low-loss SAW filter using internal floating electrode reflection types of single-phase unidirectional transducer," *Electronics Letters*, vol. 20, no. 24, pp. 989–990, Nov. 1984, doi: 10.1049/EL:19840672.

[57] Y. Wu, R. Chattaraj, Y. Ren, H. Jiang, and D. Lee, "Label-Free Multitarget Separation of Particles and Cells under Flow Using Acoustic, Electrophoretic, and Hydrodynamic Forces," *Analytical Chemistry*, vol. 93, no. 21, pp. 7635–7646, Jun. 2021, doi: 10.1021/acs.analchem.1c00312.

[58] C. Wyatt Shields Iv, C. D. Reyes, and G. P. López, "Microfluidic cell sorting: A review of the advances in the separation of cells from debulking to rare cell isolation," *Lab on a Chip*. 2015. doi: 10.1039/c4lc01246a.

[59] S. Yan, J. Zhang, D. Yuan, and W. Li, "Hybrid microfluidics combined with active and passive approaches for continuous cell separation," *ELECTROPHORESIS*, vol. 38, no. 2, pp. 238–249, Jan. 2017, doi: 10.1002/ELPS.201600386.

[60] F. Fachin *et al.*, “Monolithic Chip for High-throughput Blood Cell Depletion to Sort Rare Circulating Tumor Cells,” *Scientific Reports 2017 7:1*, vol. 7, no. 1, pp. 1–11, Sep. 2017, doi: 10.1038/s41598-017-11119-x.

[61] T. K. Chiu *et al.*, “A low-sample-loss microfluidic system for the quantification of size-independent cellular electrical property—Its demonstration for the identification and characterization of circulating tumour cells (CTCs),” *Sensors and Actuators B: Chemical*, vol. 246, pp. 29–37, Jul. 2017, doi: 10.1016/J.SNB.2017.02.048.

[62] Y. Zhao *et al.*, “A microfluidic system for cell type classification based on cellular size-independent electrical properties,” *Lab on a Chip*, vol. 13, no. 12, pp. 2272–2277, May 2013, doi: 10.1039/C3LC41361F.

[63] Y. Zhao *et al.*, “A microfluidic system enabling continuous characterization of specific membrane capacitance and cytoplasm conductivity of single cells in suspension,” *Biosensors and Bioelectronics*, vol. 43, no. 1, pp. 304–307, May 2013, doi: 10.1016/J.BIOS.2012.12.035.

[64] M. Mizuno, M. Yamada, R. Mitamura, K. Ike, K. Toyama, and M. Seki, “Magnetophoresis-Integrated Hydrodynamic Filtration System for Size- and Surface Marker-Based Two-Dimensional Cell Sorting,” *Analytical Chemistry*, vol. 85, no. 16, pp. 7666–7673, Aug. 2013, doi: 10.1021/AC303336F.

[65] H. Song *et al.*, “Continuous-flow sorting of stem cells and differentiation products based on dielectrophoresis,” *Lab on a Chip*, vol. 15, no. 5, pp. 1320–1328, 2015, doi: 10.1039/C4LC01253D.

[66] Z. Ma, Y. Zhou, D. J. Collins, and Y. Ai, “Fluorescence activated cell sorting via a focused traveling surface acoustic beam,” *Lab on a Chip*, vol. 17, no. 18, pp. 3176–3185, 2017, doi: 10.1039/C7LC00678K.

[67] S. Sakuma, Y. Kasai, T. Hayakawa, and F. Arai, “On-chip cell sorting by high-speed local-flow control using dual membrane pumps,” *Lab on a Chip*, vol. 17, no. 16, pp. 2760–2767, 2017, doi: 10.1039/C7LC00536A.

[68] J.-J. Lee *et al.*, “Synthetic Ligand-Coated Magnetic Nanoparticles for Microfluidic Bacterial Separation from Blood,” *Nano Letters*, vol. 14, no. 1, pp. 1–5, Jan. 2014, doi: 10.1021/nl3047305.

[69] Y. Hosokawa, “Applications of the femtosecond laser-induced impulse to cell research,” *Japanese Journal of Applied Physics*, 2019, doi: 10.7567/1347-4065/ab4749.

[70] Y. Shen, Y. Yalikun, Y. Aishan, N. Tanaka, A. Sato, and Y. Tanaka, “Area cooling enables thermal positioning and manipulation of single cells,” *Lab on a Chip*, vol. 20, no. 20, pp. 3733–3743, 2020, doi: 10.1039/D0LC00523A.

[71] T. Tang *et al.*, “Dual-frequency impedance assays for intracellular components in microalgal cells,” *Lab on a Chip*, 2022, doi: 10.1039/D1LC00721A.

[72] Y. Yalikun *et al.*, “Effects of Flow-Induced Microfluidic Chip Wall Deformation on Imaging Flow Cytometry,” *Cytometry Part A*, vol. 97, no. 9, pp. 909–920, Sep. 2020, doi: 10.1002/cyto.a.23944.

[73] T. Zhang *et al.*, “Hydrodynamic particle focusing enhanced by femtosecond laser deep grooving at low Reynolds numbers,” *Scientific Reports*, vol. 11, no. 1, pp. 1–10, 2021, doi: 10.1038/s41598-021-81190-y.

[74] Y. Feng, L. Huang, P. Zhao, F. Liang, and W. Wang, “A Microfluidic Device Integrating Impedance Flow Cytometry and Electric Impedance Spectroscopy for High-Efficiency Single-Cell

Electrical Property Measurement," *Analytical Chemistry*, vol. 91, no. 23, pp. 15204–15212, 2019, doi: 10.1021/acs.analchem.9b04083.

[75] Z. Zhu, X. Xu, L. Fang, D. Pan, and Q. A. Huang, "Investigation of geometry-dependent sensing characteristics of microfluidic electrical impedance spectroscopy through modeling and simulation," *Sensors and Actuators, B: Chemical*, vol. 235, 2016, doi: 10.1016/j.snb.2016.05.092.

[76] T. Tang *et al.*, "Assessment of the electrical penetration of cell membranes using four-frequency impedance cytometry," *Microsystems & Nanoengineering 2022 8:1*, vol. 8, no. 1, pp. 1–12, Jun. 2022, doi: 10.1038/s41378-022-00405-y.

[77] Z.-Y. Hong, K. Okano, D. di Carlo, Y. Tanaka, Y. Yalikun, and Y. Hosokawa, "High-speed micro-particle manipulation in a microfluidic chip by directional femtosecond laser impulse," *Sensors and Actuators A: Physical*, vol. 297, Oct. 2019, doi: 10.1016/j.sna.2019.111566.

[78] D. Holmes *et al.*, "Leukocyte analysis and differentiation using high speed microfluidic single cell impedance cytometry," *Lab on a Chip*, 2009, doi: 10.1039/b910053a.

[79] D. Spencer and H. Morgan, "High-Speed Single-Cell Dielectric Spectroscopy," *ACS Sensors*, vol. 5, no. 2, pp. 423–430, Feb. 2020, doi: 10.1021/acssensors.9b02119.

[80] T. Sun, S. Gawad, N. G. Green, and H. Morgan, "Dielectric spectroscopy of single cells: time domain analysis using Maxwell's mixture equation," *Journal of Physics D: Applied Physics*, vol. 40, no. 1, p. 1, Dec. 2006, doi: 10.1088/0022-3727/40/1/S01.

[81] T. Sun, N. G. Green, and H. Morgan, "Analytical and numerical modeling methods for impedance analysis of single cells on-chip," *Nano*, vol. 3, no. 1, 2008, doi: 10.1142/S1793292008000800.

[82] H. Daguerre, M. Solsona, J. Cottet, M. Gauthier, P. Renaud, and A. Bolopion, "Positional Dependence of Particles and Cells in Microfluidic Electrical Impedance Flow Cytometry: Origin, Challenges and Opportunities," *Lab on a Chip*, 2020, doi: 10.1039/D0LC00616E.

[83] H. Chun, T. D. Chung, and H. C. Kim, "Cytometry and velocimetry on a microfluidic chip using polyelectrolytic salt bridges," *Analytical Chemistry*, vol. 77, no. 8, 2005, doi: 10.1021/ac048535o.

[84] J. Chen *et al.*, "Classification of cell types using a microfluidic device for mechanical and electrical measurement on single cells," *Lab on a Chip*, 2011, doi: 10.1039/c1lc20473d.

[85] Y. Zhang *et al.*, "Crossing constriction channel-based microfluidic cytometry capable of electrically phenotyping large populations of single cells," *Analyst*, vol. 144, no. 3, 2019, doi: 10.1039/c8an02100g.

[86] K. R. Foster and H. P. Schwan, "Dielectric properties of tissues and biological materials: a critical review.," *Critical Reviews in Biomedical Engineering*, vol. 17, no. 1. 1989.

[87] S. M. A. Iqbal and N. Z. Butt, "Design and analysis of microfluidic cell counter using spice simulation," *SN Applied Sciences*, vol. 1, no. 10, 2019, doi: 10.1007/s42452-019-1327-1.

[88] T. Sun, H. Morgan, and N. G. Green, "Analytical solutions of ac electrokinetics in interdigitated electrode arrays: Electric field, dielectrophoretic and traveling-wave dielectrophoretic forces," *Physical Review E - Statistical, Nonlinear, and Soft Matter Physics*, vol. 76, no. 4, 2007, doi: 10.1103/PhysRevE.76.046610.

[89] K. Huang *et al.*, "A wide-band digital lock-in amplifier and its application in microfluidic impedance measurement," *Sensors (Switzerland)*, vol. 19, no. 16, 2019, doi: 10.3390/s19163519.

[90] D. Divakar, K. Mahesh, M. M. Varma, and P. Sen, “FPGA-Based Lock-In Amplifier for Measuring the Electrical Properties of Individual Cells,” in *2018 IEEE 13th Annual International Conference on Nano/Micro Engineered and Molecular Systems (NEMS)*, Apr. 2018, pp. 1–5. doi: 10.1109/NEMS.2018.8556987.

[91] T. Tang *et al.*, “FPGA-Assisted Nonparallel Impedance Cytometry as Location Sensor of Single Particle,” in *2021 21st International Conference on Solid-State Sensors, Actuators and Microsystems (Transducers)*, Jun. 2021, pp. 727–730. doi: 10.1109/Transducers50396.2021.9495657.

[92] A. Furniturewalla, M. Chan, J. Sui, K. Ahuja, and M. Javanmard, “Fully integrated wearable impedance cytometry platform on flexible circuit board with online smartphone readout,” *Microsystems and Nanoengineering*, vol. 4, no. 1, 2018, doi: 10.1038/s41378-018-0019-0.

[93] V. S. Hollis, J. A. Holloway, S. Harris, D. Spencer, C. van Berkel, and H. Morgan, “Comparison of Venous and Capillary Differential Leukocyte Counts Using a Standard Hematology Analyzer and a Novel Microfluidic Impedance Cytometer,” *PLOS ONE*, vol. 7, no. 9, p. e43702, Sep. 2012, doi: 10.1371/JOURNAL.PONE.0043702.

[94] D. Dieujuste, Y. Qiang, and E. Du, “A portable impedance microflow cytometer for measuring cellular response to hypoxia,” *Biotechnology and Bioengineering*, vol. 118, no. 10, pp. 4041–4051, Oct. 2021, doi: 10.1002/BIT.27879.

[95] J. Zhong, M. Liang, and Y. Ai, “Submicron-precision particle characterization in microfluidic impedance cytometry with double differential electrodes,” *Lab on a Chip*, 2021, doi: 10.1039/D1LC00481F.

[96] A. de Ninno *et al.*, “High-throughput label-free characterization of viable, necrotic and apoptotic human lymphoma cells in a coplanar-electrode microfluidic impedance chip,” *Biosensors and Bioelectronics*, vol. 150, p. 111887, Feb. 2020, doi: 10.1016/J.BIOS.2019.111887.

[97] H. Wang, N. Sobahi, and A. Han, “Impedance spectroscopy-based cell/particle position detection in microfluidic systems,” *Lab on a Chip*, vol. 17, no. 7, pp. 1264–1269, 2017, doi: 10.1039/C6LC01223J.

[98] C. Petchakup, H. Li, and H. W. Hou, “Advances in single cell impedance cytometry for biomedical applications,” *Micromachines (Basel)*, vol. 8, no. 3, 2017, doi: 10.3390/mi8030087.

[99] Y. Xu, X. Xie, Y. Duan, L. Wang, Z. Cheng, and J. Cheng, “A review of impedance measurements of whole cells,” *Biosensors and Bioelectronics*, vol. 77, pp. 824–836, 2016, doi: 10.1016/j.bios.2015.10.027.

[100] T. SUN, N. G. GREEN, and H. MORGAN, “ANALYTICAL AND NUMERICAL MODELING METHODS FOR IMPEDANCE ANALYSIS OF SINGLE CELLS ON-CHIP,” *Nano*, vol. 03, no. 01, pp. 55–63, Feb. 2008, doi: 10.1142/S1793292008000800.

[101] D. C. Spencer, T. F. Paton, K. T. Mulroney, T. J. J. Inglis, J. M. Sutton, and H. Morgan, “A fast impedance-based antimicrobial susceptibility test,” *Nature Communications*, vol. 11, no. 1, p. 5328, Dec. 2020, doi: 10.1038/s41467-020-18902-x.

[102] H. Morgan, T. Sun, D. Holmes, S. Gawad, and N. G. Green, “Single cell dielectric spectroscopy,” *Journal of Physics D: Applied Physics*, vol. 40, no. 1, pp. 61–70, Jan. 2007, doi: 10.1088/0022-3727/40/1/S10.

[103] T. Sun, S. Gawad, C. Bernabini, N. G. Green, and H. Morgan, “Broadband single cell impedance spectroscopy using maximum length sequences: theoretical analysis and practical considerations,”

Measurement Science and Technology, vol. 18, no. 9, pp. 2859–2868, Sep. 2007, doi: 10.1088/0957-0233/18/9/015.

[104] L. Gong *et al.*, “Direct and Label-Free Cell Status Monitoring of Spheroids and Microcarriers Using Microfluidic Impedance Cytometry,” *Small*, vol. 17, no. 21, p. 2007500, May 2021, doi: 10.1002/smll.202007500.

[105] K. Mahesh, M. Varma, and P. Sen, “Double-peak signal features in microfluidic impedance flow cytometry enable sensitive measurement of cell membrane capacitance,” *Lab on a Chip*, vol. 20, no. 22, pp. 4296–4309, 2020, doi: 10.1039/D0LC00744G.

[106] N. Haandbæk, S. C. Bürgel, F. Heer, and A. Hierlemann, “Characterization of subcellular morphology of single yeast cells using high frequency microfluidic impedance cytometer,” *Lab Chip*, vol. 14, no. 2, pp. 369–377, 2014, doi: 10.1039/C3LC50866H.

[107] Y.-H. M. Chan and W. F. Marshall, “How Cells Know the Size of Their Organelles,” *Science (1979)*, vol. 337, no. 6099, pp. 1186–1189, Sep. 2012, doi: 10.1126/science.1223539.

[108] H. Inui, K. Miyatake, Y. Nakano, and S. Kitaoka, “Wax ester fermentation in Euglena gracilis,” *FEBS Letters*, vol. 150, no. 1, pp. 89–93, Dec. 1982, doi: 10.1016/0014-5793(82)81310-0.

[109] L. A. Staehelin, “Chloroplast structure: From chlorophyll granules to supra-molecular architecture of thylakoid membranes,” *Photosynthesis Research*, vol. 76, no. 1–3, pp. 185–196, 2003, doi: 10.1023/A:1024994525586.

[110] A. K. Monfils, R. E. Triemer, and E. F. Bellairs, “Characterization of paramylon morphological diversity in photosynthetic euglenoids (Euglenales, Euglenophyta),” *Phycologia*, vol. 50, no. 2, pp. 156–169, Mar. 2011, doi: 10.2216/09-112.1.

[111] D. Baumer, A. Preisfeld, and H. G. Ruppel, “ISOLATION AND CHARACTERIZATION OF PARAMYLON SYNTHASE FROM EUGLENA GRACILIS (EUGLENOPHYCEAE)1,” *Journal of Phycology*, vol. 37, no. 1, pp. 38–46, Feb. 2001, doi: 10.1046/j.1529-8817.2001.037001038.x.

[112] L. Barsanti, V. Passarelli, V. Evangelista, A. M. Frassanito, and P. Gualtieri, “Chemistry, physico-chemistry and applications linked to biological activities of β-glucans,” *Natural Product Reports*, vol. 28, no. 3, p. 457, 2011, doi: 10.1039/c0np00018c.

[113] A. Gissibl, A. Sun, A. Care, H. Nevalainen, and A. Sunna, “Bioproducts From Euglena gracilis: Synthesis and Applications,” *Frontiers in Bioengineering and Biotechnology*, vol. 7, May 2019, doi: 10.3389/fbioe.2019.00108.

[114] C. A. E. Little, N. D. Orloff, I. E. Hanemann, C. J. Long, V. M. Bright, and J. C. Booth, “Modeling electrical double-layer effects for microfluidic impedance spectroscopy from 100 kHz to 110 GHz,” *Lab on a Chip*, vol. 17, no. 15, pp. 2674–2681, Jul. 2017, doi: 10.1039/C7LC00347A.

[115] T. A. Zangle, D. Burnes, C. Mathis, O. N. Witte, and M. A. Teitell, “Quantifying Biomass Changes of Single CD8+ T Cells during Antigen Specific Cytotoxicity,” *PLOS ONE*, vol. 8, no. 7, p. e68916, Jul. 2013, doi: 10.1371/JOURNAL.PONE.0068916.

[116] N. Rhind, “Cell-size control,” *Current Biology*, vol. 31, no. 21, pp. R1414–R1420, Nov. 2021, doi: 10.1016/J.CUB.2021.09.017.

[117] L. Petrus and M. A. Noordermeer, “Biomass to biofuels, a chemical perspective,” *Green Chemistry*, vol. 8, no. 10, pp. 861–867, Oct. 2006, doi: 10.1039/B605036K.

[118] R. Sindhu, P. Binod, A. Pandey, S. Ankaram, Y. Duan, and M. K. Awasthi, "Biofuel Production From Biomass: Toward Sustainable Development," *Current Developments in Biotechnology and Bioengineering: Waste Treatment Processes for Energy Generation*, pp. 79–92, Jan. 2019, doi: 10.1016/B978-0-444-64083-3.00005-1.

[119] J. Gala de Pablo, M. Lindley, K. Hiramatsu, and K. Goda, "High-Throughput Raman Flow Cytometry and Beyond," *Accounts of Chemical Research*, vol. 54, no. 9, pp. 2132–2143, May 2021, doi: 10.1021/acs.accounts.1c00001.

[120] N. Ota *et al.*, "Isolating Single Euglena gracilis Cells by Glass Microfluidics for Raman Analysis of Paramylon Biogenesis," *Analytical Chemistry*, vol. 91, no. 15, pp. 9631–9639, 2019, doi: 10.1021/acs.analchem.9b01007.

[121] J. Fernandez-de-Cossio-Diaz and R. Mulet, "Maximum entropy and population heterogeneity in continuous cell cultures," *PLOS Computational Biology*, vol. 15, no. 2, p. e1006823, Feb. 2019, doi: 10.1371/JOURNAL.PCBI.1006823.

[122] B. W. Thuronyi *et al.*, "Continuous evolution of base editors with expanded target compatibility and improved activity," *Nature Biotechnology 2019 37:9*, vol. 37, no. 9, pp. 1070–1079, Jul. 2019, doi: 10.1038/s41587-019-0193-0.

[123] L. E. KOREN, "High-yield media for photosynthesizing Euglena gracilis Z," *J. Portozool*, vol. 14, p. 17, 1967, [Online]. Available: https://ci.nii.ac.jp/naid/10005190559/en/

[124] M. Cramer and J. Myers, "Growth and photosynthetic characteristics of euglena gracilis," *Archiv für Mikrobiologie 1952 17:1*, vol. 17, no. 1, pp. 384–402, Jan. 1952, doi: 10.1007/BF00410835.

[125] Y. Wang, T. Seppänen-Laakso, H. Rischer, and M. G. Wiebe, "Euglena gracilis growth and cell composition under different temperature, light and trophic conditions," *PLoS ONE*, vol. 13, no. 4, Apr. 2018, doi: 10.1371/JOURNAL.PONE.0195329.

[126] S. Muramatsu *et al.*, "Isolation and characterization of a motility-defective mutant of Euglena gracilis," *PeerJ*, vol. 8, p. e10002, Sep. 2020, doi: 10.7717/PEERJ.10002/SUPP-3.

[127] T. Matsumoto, H. Inui, K. Miyatake, Y. Nakano, and K. Murakami, "Comparison of Nutrients in Euglena with those in Other Representative Food Sources," *Eco-Engineering*, vol. 21, no. 2, pp. 81–86, 2009, doi: 10.11450/seitaikogaku.21.81.

[128] R. J. Cousins, "A role of zinc in the regulation of gene expression," *Proceedings of the Nutrition Society*, vol. 57, no. 2, pp. 307–311, May 1998, doi: 10.1079/PNS19980045.

[129] M. Kamalanathan, P. Chaisutyakorn, R. Gleadow, and J. Beardall, "A comparison of photoautotrophic, heterotrophic, and mixotrophic growth for biomass production by the green alga Scenedesmus sp. (Chlorophyceae)," *https://doi.org/10.2216/17-82.1*, vol. 57, no. 3, pp. 309–317, Mar. 2019, doi: 10.2216/17-82.1.

[130] T. Tang *et al.*, "Impedance-based tracking of the loss of intracellular components in microalgae cells," *Sensors and Actuators B: Chemical*, vol. 358, p. 131514, May 2022, doi: 10.1016/j.snb.2022.131514.

[131] X. Han, C. van Berkel, J. Gwyer, L. Capretto, and H. Morgan, "Microfluidic lysis of human blood for leukocyte analysis using single cell impedance cytometry," *Analytical Chemistry*, vol. 84, no. 2, 2012, doi: 10.1021/ac202700x.

[132] OCHI and H., “Requirement and accumulation of inorganic ions in Euglena gracilis Z.,” *J. Jpn. Soc. Nutr. And Food Sci.*, vol. 43, pp. 54–57, 1990, Accessed: Dec. 10, 2021. [Online]. Available: http://ci.nii.ac.jp/naid/10024768389/en/

[133] V. Nigon and P. Heizmann, “Morphology, Biochemistry, and Genetics of Plastid Development in Euglena gracilis,” 1978, pp. 211–290. doi: 10.1016/S0074-7696(08)62243-3.

[134] J. R. Cook, “Unbalanced Growth and Replication of Chloroplast Populations in Euglena gracilis,” *Journal of General Microbiology*, vol. 75, no. 1, pp. 51–60, Mar. 1973, doi: 10.1099/00221287-75-1-51.

[135] E. DAVIS and H. EPSTEIN, “Some factors controlling step-wise variation of organelle number in,” *Experimental Cell Research*, vol. 65, no. 2, pp. 273–280, Apr. 1971, doi: 10.1016/0014-4827(71)90002-4.

[136] B. Khatiwada *et al.*, “Probing the Role of the Chloroplasts in Heavy Metal Tolerance and Accumulation in Euglena gracilis,” *Microorganisms 2020, Vol. 8, Page 115*, vol. 8, no. 1, p. 115, Jan. 2020, doi: 10.3390/MICROORGANISMS8010115.

[137] R. Yan, D. Zhu, Z. Zhang, Q. Zeng, and J. Chu, “Carbon metabolism and energy conversion of Synechococcus sp. PCC 7942 under mixotrophic conditions: comparison with photoautotrophic condition,” *Journal of Applied Phycology*, vol. 4, no. 24, pp. 657–668, Aug. 2012, doi: 10.1007/S10811-011-9683-2.

[138] J. Beardall and J. A. Raven, “Limits to Phototrophic Growth in Dense Culture: CO2 Supply and Light,” *Algae for Biofuels and Energy*, pp. 91–97, Jan. 2013, doi: 10.1007/978-94-007-5479-9_5.

[139] M. Einicker-Lamas *et al.*, “Euglena gracilis as a model for the study of Cu2+ and Zn2+ toxicity and accumulation in eukaryotic cells,” *Environmental Pollution*, vol. 120, no. 3, pp. 779–786, Dec. 2002, doi: 10.1016/S0269-7491(02)00170-7.

[140] A. C. Guedes and F. X. Malcata, “Nutritional value and uses of microalgae in aquaculture,” *Aquaculture*, vol. 10, no. 1516, pp. 59–78, 2012.

[141] A. Salahi, C. Honrado, A. Rane, F. Caselli, and N. S. Swami, “Modified Red Blood Cells as Multimodal Standards for Benchmarking Single-Cell Cytometry and Separation Based on Electrical Physiology,” *Analytical Chemistry*, vol. 94, no. 6, 2022, doi: 10.1021/acs.analchem.1c04739.

[142] S. Tamaki, H. Matsuzawa, and M. Matsuhashi, “Cluster of mrdA and mrdB genes responsible for the rod shape and mecillinam sensitivity of Escherichia coli,” *J Bacteriol*, vol. 141, no. 1, pp. 52–57, 1980, doi: 10.1128/JB.141.1.52-57.1980.

[143] B. Spratt, “Escherichia coli resistance to beta-lactam antibiotics through a decrease in the affinity of a target for lethality,” *Nature*, vol. 274, no. 5672, pp. 713–715, 1978, doi: 10.1038/274713A0.

[144] I. N, N. K, and W. M, “Novel S-benzylisothiourea compound that induces spherical cells in Escherichia coli probably by acting on a rod-shape-determining protein(s) other than penicillin-binding protein 2,” *Biosci Biotechnol Biochem*, vol. 66, no. 12, pp. 2658–2662, Jan. 2002, doi: 10.1271/BBB.66.2658.

[145] T. Zhang *et al.*, “Shape-based separation of drug-treated Escherichia coli using viscoelastic microfluidics,” *Lab on a Chip*, vol. 22, no. 15, pp. 2801–2809, Jul. 2022, doi: 10.1039/D2LC00339B.

[146] F. Caselli, A. de Ninno, R. Reale, L. Businaro, and P. Bisegna, “A novel wiring scheme for standard chips enabling high-accuracy impedance cytometry,” *Sensors and Actuators, B: Chemical*, vol. 256, pp. 580–589, 2018, doi: 10.1016/j.snb.2017.10.113.

[147] A. de Ninno, V. Errico, F. R. Bertani, L. Businaro, P. Bisegna, and F. Caselli, “Coplanar electrode microfluidic chip enabling accurate sheathless impedance cytometry,” *Lab on a Chip*, vol. 17, no. 6, pp. 1158–1166, 2017, doi: 10.1039/C6LC01516F.

[148] A. F. W. Coulson, “Microbiology: Proteins that bind the β-lactam antibiotics,” *Nature 1984 309:5970*, vol. 309, no. 5970, pp. 668–668, 1984, doi: 10.1038/309668a0.

[149] J. Buijs, A. S. M. Dofferhoff, J. W. Mouton, J. H. T. Wagenvoort, and J. W. M. van der Meer, “Concentration-dependency of β-lactam-induced filament formation in Gram-negative bacteria,” *Clinical Microbiology and Infection*, vol. 14, no. 4, pp. 344–349, Apr. 2008, doi: 10.1111/J.1469-0691.2007.01940.X.

[150] A. S. M. Dofferhoff and J. Buys, “The influence of antibiotic-induced filament formation on the release of endotoxin from Gram-negative bacteria:,” *http://dx.doi.org/10.1177/096805199600300304*, vol. 3, no. 3, pp. 187–194, Sep. 2016, doi: 10.1177/096805199600300304.

[151] D. L. Popham and K. D. Young, “Role of penicillin-binding proteins in bacterial cell morphogenesis,” *Current Opinion in Microbiology*, vol. 6, no. 6, pp. 594–599, Dec. 2003, doi: 10.1016/J.MIB.2003.10.002.

[152] J. Buijs, A. S. M. Dofferhoff, J. W. Mouton, and J. W. M. van der Meer, “Pathophysiology of in-vitro induced filaments, spheroplasts and rod-shaped bacteria in neutropenic mice,” *Clinical Microbiology and Infection*, vol. 12, no. 11, pp. 1105–1111, Nov. 2006, doi: 10.1111/J.1469-0691.2006.01503.X.

[153] J. Choi *et al.*, “A rapid antimicrobial susceptibility test based on single-cell morphological analysis,” *Science Translational Medicine*, vol. 6, no. 267, Dec. 2014, doi: 10.1126/SCITRANSLMED.3009650/SUPPL_FILE/6-267RA174_SUPPLEMENTARY_FILE.ZIP.

[154] S. Suthaharan, “Support Vector Machine,” pp. 207–235, 2016, doi: 10.1007/978-1-4899-7641-3_9.

[155] C. Bernabini, D. Holmes, and H. Morgan, “Micro-impedance cytometry for detection and analysis of micron-sized particles and bacteria,” *Lab on a Chip*, vol. 11, no. 3, 2011, doi: 10.1039/c0lc00099j.

[156] B. Schölkopf, J. C. Platt, J. Shawe-Taylor, A. J. Smola, and R. C. Williamson, “Estimating the support of a high-dimensional distribution,” *Neural Computation*, vol. 13, no. 7, 2001, doi: 10.1162/089976601750264965.

[157] H. Yang, I. King, and M. R. Lyu, “Multi-task learning for one-class classification,” 2010. doi: 10.1109/IJCNN.2010.5596881.

[158] B. Schölkopf, R. Williamson, A. Smola, J. Shawe-Taylor, and J. Piatt, “Support vector method for novelty detection,” 2000.

[159] F. Gökçe, P. S. Ravaynia, M. M. Modena, and A. Hierlemann, “What is the future of electrical impedance spectroscopy in flow cytometry?,” *Biomicrofluidics*, vol. 15, no. 6, 2021, doi: 10.1063/5.0073457.

[160] Y. Ai and P. Li, “Label-free multivariate biophysical phenotyping-activated acoustic sorting at the single-cell level,” *Analytical Chemistry*, vol. 93, no. 8, 2021, doi: 10.1021/acs.analchem.0c05352.

[161] J. Chen, C. Xue, Y. Zhao, D. Chen, M. H. Wu, and J. Wang, "Microfluidic impedance flow cytometry enabling high-throughput single-cell electrical property characterization," *International Journal of Molecular Sciences*, vol. 16, no. 5, pp. 9804–9830, 2015, doi: 10.3390/ijms16059804.

[162] Z. Han, L. Chen, S. Zhang, J. Wang, and X. Duan, "Label-Free and Simultaneous Mechanical and Electrical Characterization of Single Plant Cells Using Microfluidic Impedance Flow Cytometry," *Analytical Chemistry*, vol. 92, no. 21, 2020, doi: 10.1021/acs.analchem.0c02854.

[163] R. Petkovsek, P. Gregorcic, and J. Mozina, "A beam-deflection probe as a method for optodynamic measurements of cavitation bubble oscillations," *Measurement Science and Technology*, vol. 18, no. 9, p. 2972, Aug. 2007, doi: 10.1088/0957-0233/18/9/030.

[164] R. Zhao, R. qing Xu, Z. hua Shen, J. Lu, and X. wu Ni, "Experimental investigation of the collapse of laser-generated cavitation bubbles near a solid boundary," *Optics & Laser Technology*, vol. 39, no. 5, pp. 968–972, Jul. 2007, doi: 10.1016/J.OPTLASTEC.2006.06.005.

[165] P. Gregorčič, R. Petkovšek, and J. Možina, "Investigation of a cavitation bubble between a rigid boundary and a free surface," *Journal of Applied Physics*, vol. 102, no. 9, p. 094904, Nov. 2007, doi: 10.1063/1.2805645.

[166] E. A. Brujan and A. Vogel, "Stress wave emission and cavitation bubble dynamics by nanosecond optical breakdown in a tissue phantom," *Journal of Fluid Mechanics*, vol. 558, pp. 281–308, Jul. 2006, doi: 10.1017/S0022112006000115.

[167] L. R. O. M. F.R.S., "VIII. On the pressure developed in a liquid during the collapse of a spherical cavity," *https://doi.org/10.1080/14786440808635681*, vol. 34, no. 200, pp. 94–98, Aug. 2009, doi: 10.1080/14786440808635681.

[168] M. S. Plesset, "The Dynamics of Cavitation Bubbles," *Journal of Applied Mechanics*, vol. 16, no. 3, pp. 277–282, Sep. 1949, doi: 10.1115/1.4009975.

[169] "A discussion on deformation of solids by the impact of liquids, and its relation to rain damage in aircraft and missiles, to blade erosion in steam turbines, and to cavitation erosion - The collapse of cavitation bubbles and the pressures thereby produced against solid boundaries," *Philosophical Transactions of the Royal Society of London. Series A, Mathematical and Physical Sciences*, vol. 260, no. 1110, 1966, doi: 10.1098/rsta.1966.0046.

[170] J. R. Blake and D. C. Gibson, "Growth and Collapse of A Vapour Cavity Near A Free Surface," *Journal of Fluid Mechanics*, vol. 111, 1981, doi: 10.1017/S0022112081002322.

[171] J. R. Krieger and G. L. Chahine, "Acoustic signals of underwater explosions near surfaces," *J Acoust Soc Am*, vol. 118, no. 5, 2005, doi: 10.1121/1.2047147.

[172] Y. Tomita and A. Shima, "Mechanisms of impulsive pressure generation and damage pit formation by bubble collapse," *Journal of Fluid Mechanics*, vol. 169, 1986, doi: 10.1017/S0022112086000745.

[173] Y. Tomita and T. Kodama, "Interaction of laser-induced cavitation bubbles with composite surfaces," *Journal of Applied Physics*, vol. 94, no. 5, 2003, doi: 10.1063/1.1594277.

[174] P. B. Robinson, J. R. Blake, T. Kodama, A. Shima, and Y. Tomita, "Interaction of cavitation bubbles with a free surface," *Journal of Applied Physics*, vol. 89, no. 12, 2001, doi: 10.1063/1.1368163.

[175] S. Li *et al.*, “An On-chip, multichannel droplet sorter using standing surface acoustic waves,” *Analytical Chemistry*, vol. 85, no. 11, pp. 5468–5474, Jun. 2013, doi: 10.1021/AC400548D/SUPPL_FILE/AC400548D_SI_006.AVI.

[176] A. Isozaki *et al.*, “Sequentially addressable dielectrophoretic array for high-throughput sorting of large-volume biological compartments,” *Science Advances*, vol. 6, no. 22, p. eaba6712, May 2020, doi: 10.1126/sciadv.aba6712.

[177] A. Isozaki, D. Huang, Y. Nakagawa, and K. Goda, “Dual sequentially addressable dielectrophoretic array for high-throughput, scalable, multiplexed droplet sorting,” *Microfluidics and Nanofluidics*, vol. 25, no. 4, pp. 1–10, Apr. 2021, doi: 10.1007/S10404-021-02432-Z/FIGURES/6.

[178] K. de Wijs *et al.*, “Micro vapor bubble jet flow for safe and high-rate fluorescence-activated cell sorting,” *Lab on a Chip*, vol. 17, no. 7, pp. 1287–1296, Mar. 2017, doi: 10.1039/C6LC01560C.

[179] X. Qi *et al.*, “Optical sorting and cultivation of denitrifying anaerobic methane oxidation archaea,” *Biomedical Optics Express, Vol. 8, Issue 2, pp. 934-942*, vol. 8, no. 2, pp. 934–942, Feb. 2017, doi: 10.1364/BOE.8.000934.

[180] Y. Chen, T. H. Wu, Y. C. Kung, M. A. Teitell, and P. Y. Chiou, “3D pulsed laser-triggered high-speed microfluidic fluorescence-activated cell sorter,” *Analyst*, vol. 138, no. 24, pp. 7308–7315, Nov. 2013, doi: 10.1039/C3AN01266B.

[181] R. H. Cole *et al.*, “Printed droplet microfluidics for on demand dispensing of picoliter droplets and cells,” *Proc Natl Acad Sci U S A*, vol. 114, no. 33, pp. 8728–8733, Aug. 2017, doi: 10.1073/PNAS.1704020114/-/DCSUPPLEMENTAL.

[182] L. Yang, P. P. Banada, A. K. Bhunia, and R. Bashir, “Effects of Dielectrophoresis on growth, viability and immuno-reactivity of Listeria monocytogenes,” *Journal of Biological Engineering*, vol. 2, no. 1, pp. 1–14, Apr. 2008, doi: 10.1186/1754-1611-2-6/TABLES/1.

[183] S. S. Schütz, T. Beneyton, J. C. Baret, and T. M. Schneider, “Rational design of a high-throughput droplet sorter,” *Lab on a Chip*, vol. 19, no. 13, pp. 2220–2232, Jun. 2019, doi: 10.1039/C9LC00149B.

[184] H. D. Xi *et al.*, “Active droplet sorting in microfluidics: a review,” *Lab on a Chip*, vol. 17, no. 5, pp. 751–771, Feb. 2017, doi: 10.1039/C6LC01435F.

Achievements

論文業績

1.学術論文

1.1 すでに採択されたもの：

[1] **Tao Tang,** Xun Liu, Yapeng Yuan, Tianlong Zhang, Royata Kiya, Kengo Suzuki, Yang Yang, Yo Tanaka, Ming Li, Yoichiroh Hosokawa and Yaxiaer Yalikun*“Assessment of electrical penetration of cell membrane using four-frequency impedance cytometry”, **Microsystems & Nanoenginerring** (2022). https://doi.org/10.1038/s41378-022-00405-y **(IF: 7.127)**

[2] **Tao Tang #,** Xun Liu #, Yapeng Yuan, Tianlong Zhang, Royata Kiya, Kengo Suzuki, Yo Tanaka, Ming Li, Yoichiroh Hosokawa and Yaxiaer Yalikun *“Impedance-based tracking of the loss of intracellular components in microalgae cells”, **Sensors and Actuators B: Chemical**. (2022). https://doi.org/10.1016/j.snb.2022.131514 **(IF: 7.46)**

[3] **Tao Tang**, Xun Liu, Yapeng Yuan, Royata Kiya, Yigang Shen, Tianlong Zhang, Kengo Suzuki, Ming Li, Yo Tanaka, Yoichiroh Hosokawa and Yaxiaer Yalikun *, “Dual-frequency impedance assays for intracellular components in microalgal cells”, **Lab on a Chip** (2021). https://doi.org/10.1039/D1LC00721A **(IF 6.799)**

[4] **Tao Tang**, Xun Liu, Yigang Shen, Yapeng Yuan, Tianlong Zhang, Yo Tanaka, Kengo Suzuki, Ming Li, Yoichiroh Hosokawa and Yaxiaer Yalikun *, “Microscopic impedance cytometry for single-cell shape characterization”, **Biosensors and Bioelectronics** 193 (2021): 113521. https://doi.org/10.1016/j.bios.2021.113521 **(IF 10.618)**

[5] **Tao Tang #,** Yapeng Yuan #, Yaxiaer Yalikun *, Yoichiroh Hosokawa, Ming Li, Yo Tanaka*, “Glass based micro total analysis systems: Materials, fabrication methods, and applications”, **Sensors and Actuators B: Chemical.** (2021) https://doi.org/10.1016/j.snb.2021.129859 **(IF: 7.4)**

[6] **Tao Tang**, Yoichiroh Hosokawa, Takeshi Hayakawa, Yo Tanaka, Weihua Li, Ming Li*, Yaxiaer Yalikun*, “Rotation of Biological Cells: Fundamentals and Applications”, **Engineering.** 2021. https://doi.org/10.1016/j.eng.2020.07.031 **(IF: 7.55)**

1.2 査読中にあるもの:

[7] **Tao Tang**, Xun Liu, Yapeng Yuan, Tianlong Zhang, Royata Kiya, Yang Yang, Yoichi Yamazaki, Hironari Kamikubo, Yo Tanaka, Ming Li, Yoichiroh Hosokawa and Yaxiaer Yalikun* “Real-time seeing single bacteria susceptibility with parallel impedance cytometry at nano and microscales” **ACS Sensors (IF: 7.711)**

[8] **Tao Tang**, Xun Liu, Yapeng Yuan, Royata Kiya, Yang Yang, Yoichi Yamazaki, Hironari Kamikubo, Yo Tanaka, Ming Li, Yoichiroh Hosokawa and Yaxiaer Yalikun* “Real-time `machine learning-based impedance system for susceptible bacteria recognition with parallel impedance cytometry”. **Sensors and Actuators B: Chemical (IF: 7.4).**

[9] **Tao Tang** #, Royata Kiya #, Yo Tanaka, Yochiroh Hosokawa and Yaxiaer Yalikun* “Multi-cell sorting method enabled by pulse irradiation of femtosecond laser”, **Scientific Reports. (IF: 4.379)**

2.学会論文

[1] **Tao Tang**, Kengo Suzuki, Yo Tanaka, Yoichiroh Hosokawa, Yaxiaer Yalikun, "Impedance-based tracking of biophysical properties of single microalgae cells" **The Robotics and Mechatronics Conference 2022 in Sapporo (Poster presentation)**

[2] **Tao Tang**, Xun Liu, Yoichiroh Hosokawa, and Yaxiaer Yalikun, "FPGA-assisted nonparallel impedance cytometry as location sensor of single cells", The 21st International conference on Solid-state sensors, actuators and microsystems (**Tranducer 2021 - Poster presentation**)

[3] **Tao Tang**, Xun Liu, Yigang Shen, Yapeng Yuan, Tianlong Zhang, Yo Tanaka, Kengo Suzuki, Ming Li, Yoichiroh Hosokawa and Yaxiaer Yalikun, "Impedance cytometry for characterizing single cell shape", The 25th International Conference on Miniaturized Systems for Chemistry and Life Sciences (**µTAS 2021- Poster presentation**)

[4] **Tao Tang**, Xun Liu, Yigang Shen,Yapeng Yuan,Tianlong Zhang, Kengo Suzuki, Yo Tanaka, Ming Li, Yoichiroh Hosokawa and Yaxiaer Yalikun, "Impedance-based single cell shape detection", The 2021 International Chemical Congress of Pacific Basin Societies (**Pacifichem 2021- Poster presentation**)

[5] **Tao Tang**, et al., "Femtosecond Laser-Induced Response Wave Measuring Method for Single Cell Characterization", **IEEE MEMS 2021 Virtual Conference, January, 462–465. (MEMS-Oral presentation)**

[6] **Tao Tang**, et al. "Single Cell Analysis Based on Femtosecond Laser-induced Acoustic Radiation",**The 42nd meeting of the Society of Chemistry and Micro / Nanosystems. (2020), 109. (Chemina-Poster presentation)**

[7] **Tao Tang,** et al., “On-chip integration of ultra-thin glass cantilever for physical property measurement activated by femtosecond laser impulse”, **Proceeding IEEE / RSJ Int. Conf. Intell.. Syst. Press. (2020) 2780–2785. (IROS-Poster presentation) Robot**

[8] **Tao Tang** et al. “M-Shaped Impedance Flow Cytometry for Cell Location Monitor”, **JSAP autumn meeting, 2020**

3. 受賞歴

[1] **Tang Tao** “The development of on-chip electrical measurement method for single cell physical properties using femtosecond laser-induced impact force” **the FY2021 Award of Encouragement from the Sasakawa Scientific Research Grant Selection Committee.**

4. プレス・リリース

[1] Tao Tang, Xun Liu, Yigang Shen, Yapeng Yuan, Tianlong Zhang, Yo Tanaka, Kengo Suzuki, Ming Li, Yoichiroh Hosokawa and Yaxiaer Yalikun *, "Microscopic impedance cytometry for quantifying single cell shape."

https://www.euglena.jp/news/20210810-2/

http://www.naist.jp/pressrelease/2021/08/008179.html

https://www.riken.jp/press/2021/20210810_1/index.html

[2] Tao Tang, Xun Liu, Yapeng Yuan, Tianlong Zhang, Royata Kiya, Kengo Suzuki, Yang Yang, Yo Tanaka, Ming Li, Yoichiroh Hosokawa and Yaxiaer Yalikun*, " Assessment of electrical penetration of cell membrane using four-frequency impedance cytometry."

https://www.naist.jp/pressrelease/2022/06/009059.html

Acknowledgements

This work was funded by the Grant-in-Aid funding from the NAIST, Amada Foundation, Sasakawa Scientific Research Grant, Japan, and the Nara Institute of Science and Technology Support Foundation, Japan. Currently, it is funded by the JST Support for Pioneering Research Initiated by the Next Generation program and Nara Institute of Science and Technology Touch stone program. I am grateful for all the financial support from above, which enabled me to purchase many of the necessary devices to carry out my experiments, and also supported me attend a lot of conferences.

Following that, I would like to express my sincere appreciation and gratitude to Professor Hosokawa and Professor Yaxiaer. Three years ago, as a new Ph.D. student, I had no experience in this research field, but they gave me numerous chances to try and fail, which allowed me to grow rapidly. Their support enabled me to decide what research topic interests me and start a totally new topic: impedance cytometry. Also, thanks to their valuable and informative comments and suggestions, I learned how to do oral/poster presentation, to write academic articles and response letter, and to determine the research topic, etc. Additionally, I am also grateful for the comments and suggestions provided by Takayuki Yanagida sensei and Kiyotaka Sasagawa sensei. As a result of their help and instruction, I was able to finish this dissertation much more effectively.

My sincere thanks also go to Prof. Li Ming, and she has greatly improved my writing abilities. Generally, my original drafts were not in good quality, and each time, she provided valuable comments to help me improve the paper. These comments taught me a lot about academic writing.

Also, I would like to thank Yo Tananka sensei for his valuable experimental comments and support over the past three years. For the sample providing, we are grateful to Kengo Suzuki sensei, Hironari Kamikubo sensei, Yoichi Yamazaki sensei.

Additionally, I would like to extend my acknowledgement to all members of Bio-Process Engineering Laboratory (生体プロセス工学研究室) in NAIST for the daily discussions and cooperation. Having been a member of this big family and doing research here was very enjoyable for me, and I will cherish the memories I made here forever. I wish you all have a bright future.

In closing, I would like to thank my parents for everything they have done for me. Thank you for your understanding and concern. Also, I would like to thank myself for all the hard work I've put in. Keep moving forward.